INTERNATIONAL JOURNAL OF

ENERGY HORIZON

VOLUME: 1 ISSUE: 1

2025

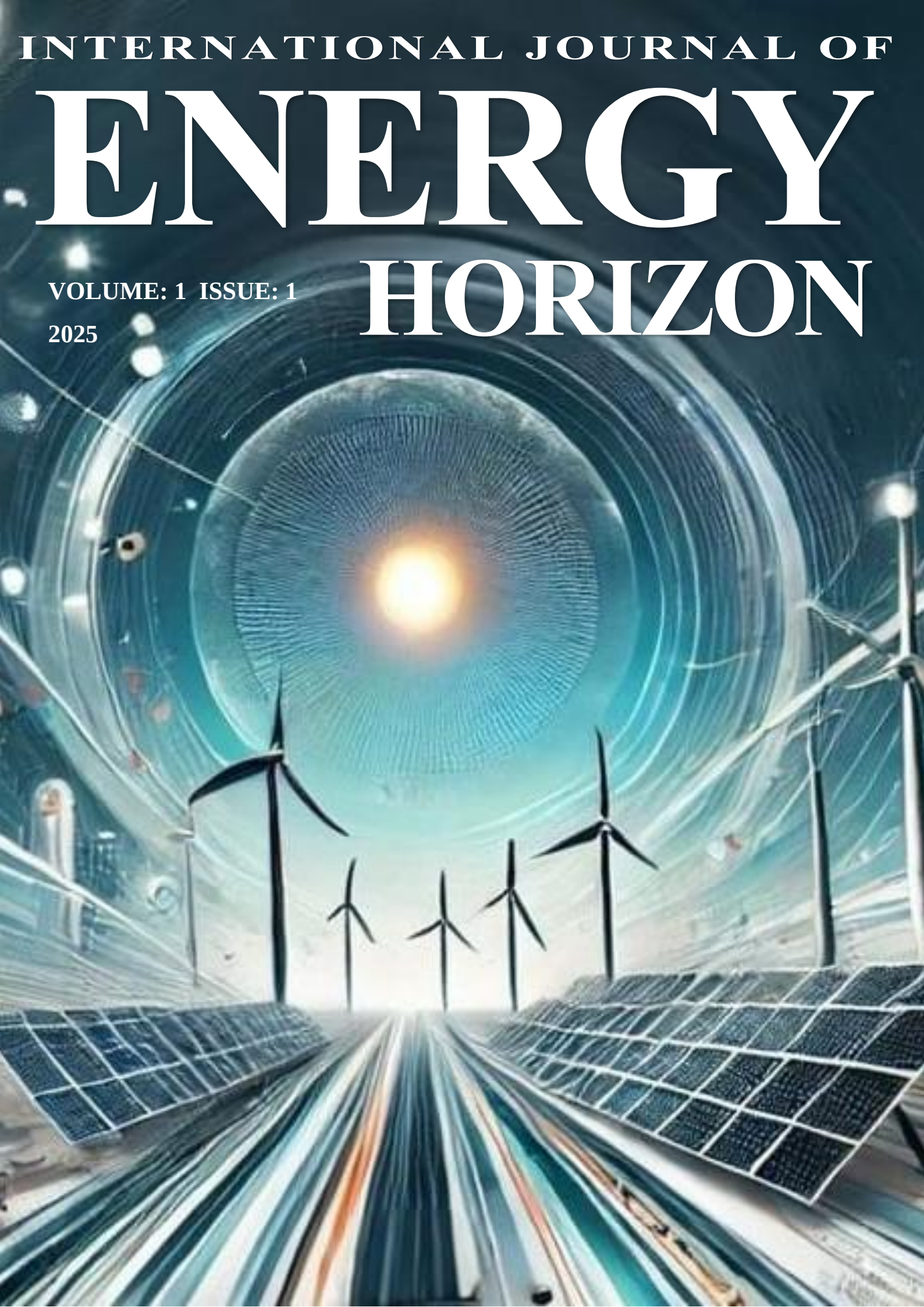

PREFACE

It is with great pleasure and anticipation that we present to you the inaugural issue of the International Journal of Energy Horizon (IJEH), a new open-access, peer-reviewed scientific journal dedicated to advancing research and innovation in the field of energy science and technology.

In an era marked by rapid technological change and urgent global challenges—especially the climate crisis and the need for sustainable energy solutions—we believe that knowledge must flow freely and collaboratively. IJEH was founded with the vision of becoming a vibrant international platform for researchers, engineers, and practitioners to share novel findings, discuss emerging trends, and promote interdisciplinary dialogue in energy systems, renewable technologies, hydrogen solutions, fuel cells, energy policy, and beyond.

This first issue reflects our mission: to bridge academic rigor with real-world relevance. We are proud to showcase original research articles and reviews contributed by scholars whose work embodies excellence, originality, and impact.

We extend our sincere gratitude to the editorial board, reviewers, and authors who contributed to the successful launch of IJEH. Their dedication and collaboration have laid the foundation for what we hope will become a respected and influential journal in the energy community.

As we embark on this journey, we warmly invite researchers and professionals from around the world to join us—whether as authors, readers, or reviewers—in shaping the future of sustainable energy through shared knowledge.

Welcome to the first issue of International Journal of Energy Horizon.

Editorial Team

International Journal of Energy Horizon (IJEH)

https://dergipark.org.tr/tr/pub/ijeh

International Journal of Energy Horizon (IJEH)

IJEH is published twice a year

2025, Volume 1, Issue 1

Contents

Editorial Team

International Journal of Energy Horizon 01 (2025) 1-7

International Journal of Energy Horizon

journal homepage: https://dergipark.org.tr/tr/pub/ijeh

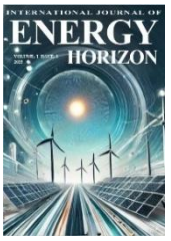

Research Paper

A Parametric and Performance-Based CFD Investigation of The Effect of Cavity Geometry and Location of Injector on Flame Stabilization in Supersonic Flow

Barış AKIN[1], Mohammed ALOBEID[2,*], Ahmed Emin KILIÇ[3]

[1,2,3]Ankara Yıldırım Beyazıt University, Faculty of Engineering and Natural Science, Mechanical Engineering Department, Ankara, 06010, Turkey
[1]ORCID No:0009-0002-0680-9890
[2]ORCID No:0009-0001-9442-4650
[3]ORCID No:0000-0002-8472-9426

ARTICLE INFO

Article History:

Received:11 June 2025
Revised:18 June 2025
Accepted:19 June 2025
Available online:30 June 2025

Keywords:

Scramjet combustion
Cavity geometry
Fuel injection location
Flame stabilization
CFD simulation

ABSTRACT

Scramjet (Supersonic Combustion Ramjet) engines are a key propulsion technology for hypersonic flight, where stable combustion and efficient fuel–air mixing under supersonic conditions remain fundamental challenges. This study presents a two-dimensional computational fluid dynamics (CFD) investigation to optimize cavity geometry and fuel injection configurations in a scramjet combustor to enhance mixing and flame stabilization. Rectangular and trapezoidal cavity geometries were assessed under varying hydrogen injection pressures (1, 2, and 3 atm) and locations (top, middle, and bottom) using ANSYS Fluent. A density-based solver incorporating the SST k-ω turbulence model and the Eddy Dissipation Model was employed to simulate reactive flow dynamics. Validation of the numerical model was performed through comparison with experimental data, ensuring mesh independence and agreement on normalized pressure profiles. Results showed that injection location and cavity geometry significantly influence flow recirculation, fuel retention, and temperature distribution. The middle injection at 2 atm in the rectangular cavity yielded the most uniform vortex formation and the highest combustion efficiency. In contrast, top injection configurations consistently resulted in poor flame holding due to bypassing of the cavity. For the trapezoidal cavity, middle and bottom injections at 2 atm exhibited comparable mixing behavior, albeit with lower peak temperatures. Overall, the rectangular cavity with centerline injection at 2 atm demonstrated optimal performance for sustained combustion in supersonic flow. These findings contribute to the design of efficient flameholders in scramjet systems, offering insights for improved performance in future hypersonic propulsion applications.

1. INTRODUCTION

Supersonic Combustion Ramjet (SCRAMJET) engines are among the most promising candidates for hypersonic propulsion, capable of operating efficiently at speeds above Mach 5. Unlike traditional rocket systems that rely on onboard oxidizers—leading to high propellant mass fractions and limited reusability—SCRAMJETs utilize atmospheric oxygen for combustion. This significantly improves payload capacity and reduces launch costs [1].

While ramjets and turbojets perform well at lower supersonic speeds, their effectiveness diminishes at hypersonic regimes due to increased flow separation, shock–boundary layer interaction, and combustion inefficiencies. SCRAMJETs overcome this by sustaining supersonic combustion, enabling continuous thrust at high Mach numbers. Nonetheless, key engineering hurdles—such as flame stabilization, efficient fuel–air mixing in ultra-short residence times, high thermal loads on structural materials, and thermal management—must be resolved [2–4].

Flame stabilization in scramjets is particularly challenging due to the supersonic flow and short interaction times. Among the studied strategies, cavity-based flameholders offer a passive means of anchoring flames via recirculation zones that slow and trap the flame within the combustor [5]. Experimental and numerical investigations have shown that rectangular, trapezoidal, and strut-assisted cavities can enhance flame stabilization under high-speed flows [5-7]. For instance, Liu et al. demonstrated ignition and flame stabilization in an ethylene-fueled cavity scramjet using high-speed imaging and pressure diagnostics [8]. Moreover, recent DNS and LES studies have characterized turbulence–flame interactions within cavity shear layers, clarifying how inflow turbulence impacts flame topology and stability[3-4] .

*Corresponding author
E-mail address: mohammed.alobed@gmail.com
journal homepage: https://dergipark.org.tr/tr/pub/ijeh

Efficient fuel mixing remains crucial under extreme supersonic conditions. Studies by Relangi et al. explored how axisymmetric cavities with angled and transverse injections affect mixing, revealing improvements in uniformity and performance [9]. Li et al. experimentally demonstrated that adding cavity-floor injection in ethylene–air flows can extend stable ignition limits by boosting residence time [10]. Other researchers have examined strut-based injectors and their interaction with shock-generated vortices, emphasizing the trade-offs between enhanced mixing and total pressure losses [11].

Combustion dynamics, including thermoacoustic instability and oscillation, directly impact durability and control. Jeong et al. applied POD techniques to high-speed CH* chemiluminescence data, identifying dominant oscillation modes in cavity combustors at Mach 2.5 [12]. Newer computational models using shock-induced stabilization via parallel cavities have been shown to attenuate instabilities and maintain stable flames at high Mach regimes [13]. Meanwhile, Huang et al. reviewed turbulence modeling and CFD simulation strategies, concluding that LES combined with detailed chemistry models offers the most accurate predictions of transient processes, including thermal and combustion responses [2].

Parametric CFD studies remain essential to optimize cavity geometry, fuel injection schemes, and operational conditions. Sun et al. assessed ignition enhancement techniques for Mach 2 combustors with cavity and floor injection under varying equivalence ratios [13]. Zhang and co-workers, analyzing strut/wall injection hybrid schemes, reported fuel penetration, flame anchoring, and temperature distribution improvements, though pressure losses required further mitigation [14]. New numerical work published in late 2024 highlighted that cavity length-to-depth ratios of around 4 maximize combustion efficiency while minimizing total pressure losses [15]. Collectively, these studies inform the design of stable, high-performance supersonic combustors.

2. NUMERICAL METHODOLOGY AND COMPUTATIONAL SETUP

2.1. Geometric Model

At The combustor geometry was designed to investigate the effects of cavity shape and injection configuration on flame stabilization. Two distinct cavity geometries rectangular and trapezoidal were considered. The performance of each was evaluated based on fuel–air mixing, recirculation behavior, and combustion efficiency.

A parametric sweep was performed for three offset ratios (Du/D = 1, 2, 3), defined as the ratio of the cavity's front wall length to the rear wall length. For each offset ratio, three rear wall ramp angles (θ = 90°, 60°, and 30°) were analyzed. This allowed a systematic investigation of cavity shape on internal vortex structure and flame anchoring potential.

In all cases, hydrogen was injected through three discrete positions along the front wall—top, middle, and bottom parallel to the main airflow. Injection pressures of 1 atm, 2 atm, and 3 atm were applied to assess their effect on combustion characteristics.

The main supersonic airflow enters the domain at Mach 3, with a stagnation temperature of 1400 K and static pressure of 1 atm. The hydrogen fuel enters at Mach 1 and 300 K, under the specified pressure levels. The simulation domain was constructed to mirror typical combustor test-section dimensions found in experimental studies.

The main flow was characterized by Mach 3 and 1 atm pressure, with an inlet temperature of 1400 K. The fuel inlet was exposed to a series of extreme conditions, including temperatures of 300K and velocities of Mach 1, as well as variable pressures.

2.2. Governing Equations And Numerical Modeling Approach

The reactive supersonic flow within the scramjet combustor was modeled as a two-dimensional, steady, compressible system governed by the conservation laws of mass, momentum, and total energy. These equations were solved using ANSYS Fluent 2024 R2 with a density-based solver and an implicit formulation.

The governing equations are as follows:

1) Continuity Equation (Mass Conservation):

$$\frac{\partial \rho}{\partial t} + \nabla \cdot (\rho \vec{v}) = 0 \tag{1}$$

2) Momentum Conservation Equation:

$$\frac{\partial (\rho \vec{v})}{\partial t} + \nabla \cdot (\rho \vec{v}\vec{v}) = -\nabla p + \nabla \cdot \tau + \rho \vec{g} \tag{2}$$

where τ is the viscous stress tensor.

$$\tau_{ij} = \mu \left(\frac{\partial v_i}{\partial x_j} + \frac{\partial v_j}{\partial x_i} \right) - \frac{2}{3} \mu (\nabla \cdot \vec{v}) \delta_{ij} \tag{3}$$

3) Energy Conservation Equation:

$$\frac{\partial (\rho E)}{\partial t} + \nabla \cdot [\vec{v}(\rho E + p)] = \nabla \cdot (k_{\text{eff}} \nabla T) + \Phi + S_h \tag{4}$$

S_h: heat production term

k_{eff}: effective thermal conductivity

Φ: viscous dispersion term

E: total energy (internal energy + kinetic energy)

2.2.1. Numerical Model

In this simulation, the k-ω SST turbulence model is employed to predict the effects of disturbances within the flow field with a high degree of accuracy. This model is known for its ability to handle complex flow situations, especially in areas with strong pressure differences and during transient flow. A primary advantage of the present approach is that it offers high accuracy near the wall while maintaining a relatively low computational cost compared to other turbulence modelling methods.

The k-ω formulation is applied to enhance accuracy in near-wall regions. The k-ε is used in the outer flow regions to blend and allow the SST model to leverage the strengths of both formulations. This hybrid approach ensures robust and physically consistent turbulence modelling. The k-ω SST model is particularly suitable for high-speed flows, such as those found in scramjet combustors [16].

$$\frac{\partial}{\partial x_i}(\rho k u_i) = \frac{\partial}{\partial x_i}\left(\Gamma_k \frac{\partial k}{\partial x_j} \right) + \widetilde{G_k} - Y_k + S_k \tag{5}$$

This equation represents turbulent kinetic energy. The right side of the equation shows diffusion, production, dispersion and an additional source.

$$\frac{\partial}{\partial x_i}(\rho \omega u_i) = \frac{\partial}{\partial x_j}\left(\Gamma_\omega \frac{\partial \omega}{\partial x_j} \right) + G_\omega - Y_\omega + D_\omega + S_\omega \tag{6}$$

This equation expresses the transport of specific turbulent dispersion velocity. The symbol D_ω denotes the cross-diffusion term.

$$D_\omega = 2(1 - F_1)\rho \sigma_{\omega 2} \cdot \frac{1}{\omega} \cdot \frac{\partial k}{\partial x_j} \cdot \frac{\partial \omega}{\partial x_j} \tag{7}$$

The cross-diffusion term is an important component of the SST model and contributes to the ω equation in the transition region.

$$\Gamma_k = \mu + \frac{\mu_t}{\sigma_k}, \quad \Gamma_\omega = \mu + \frac{\mu_t}{\sigma_\omega} \tag{8}$$

The term ' Γ ' combining the contributions of viscosity and turbulent viscosity in turbulent flows.

$$\mu_t = \frac{\rho k}{\omega} \tag{9}$$

The turbulent viscosity definition is used in the SST model. Some versions include an SST mixing function.

$$\frac{\partial}{\partial t}(\rho Y_i) + \nabla \cdot (\rho \vec{v} Y_i) = -\nabla \cdot \vec{J_i} + R_i + S_i \tag{10}$$

The transport equation for species 'i' includes diffusion flux, reaction production and external sources.

The combustion process in supersonic flows is significantly affected by turbulence. Considering the considerations, the eddy-dissipation reaction model was employed, incorporating the turbulence intensity in the calculations. The process under consideration is a one-stage chemical reaction between air and hydrogen, represented by the following formula: $2H_2+O_2 \rightarrow 2H_2O$.

$$R_i = \min\left(\frac{A\rho\epsilon}{k} \cdot \frac{Y_{\text{fuel}}}{\nu_{\text{fuel}}}, \frac{B\rho\epsilon}{k} \cdot \frac{Y_{\text{oxid}}}{\nu_{\text{oxid}}} \right) \tag{11}$$

The reaction rate in this equation is determined by the turbulent mixing ratio.

ν: Stoichiometric coefficient

Y_{fuel}: Mass fraction of H_2

Y_{oxid}: Mass fraction of O_2

The numerical analysis was conducted using commercial software, namely ANSYS-Fluent 2024 R2. In numerical analysis, the Coupled method was employed for the pressure-velocity pair, while the second-order UPWIND method was utilized for the discretization of the conservation equations. The convergence criteria were accepted as 10^{-5} for the mass and momentum conservation equations and 10^{-5} for the energy conservation equations. The numerical analyses were terminated when the convergence criteria were met.

2.3. Mesh & Boundary Conditions

To ensure numerical accuracy and solution stability, a high-quality structured mesh was generated, with localized refinement in the cavity region where complex recirculation and mixing phenomena are expected. The mesh quality was quantitatively evaluated based on element quality, aspect ratio, skewness, and orthogonal quality, as summarized in Table 1. The average element quality exceeded 0.95, indicating minimal distortion and excellent grid resolution in regions of interest. Skewness values remained below 0.17, and the orthogonal quality was consistently above 0.96, supporting accurate resolution of steep gradients in pressure and temperature. The computational domain, including the location of the cavity, injectors, and boundary conditions, is illustrated in Figure 1, which highlights the key regions of flow development and fuel–air interaction. Boundary conditions were applied to reflect realistic scramjet operating conditions: the main airflow was introduced at Mach 3 with a static pressure of 1 atm and a total temperature of 1400 K, while the hydrogen fuel was injected at Mach 1 and 300 K from three separate locations along the front cavity wall at pressures of 1 atm, 2 atm, and 3 atm. All walls were modeled as adiabatic and no-slip, and a pressure outlet was imposed downstream to allow unrestrained flow development. The inlet gas compositions used in all simulations are detailed in Table 2, with consistent species mass fractions applied for both air and hydrogen in each case. This meshing and boundary setup provided a robust framework for capturing the high-speed reactive flow characteristics critical to flame stabilization in scramjet cavities.

Table 1. Mesh metrics

	Min	Max	Average
Element Quality	0.91389	0.99997	0.95149
Aspect Ratio	1.0011	1.4983	1.3608
Skewness	1.6287e-006	0.16422	2.6285e-002
Orthogonal Quality	0.96694	1	0.99717

Table 2. Fluid inlet properties

Fluid	P (atm)	T (K)	Mach
Air	1	1200	3
H2	1,2,3	300	1

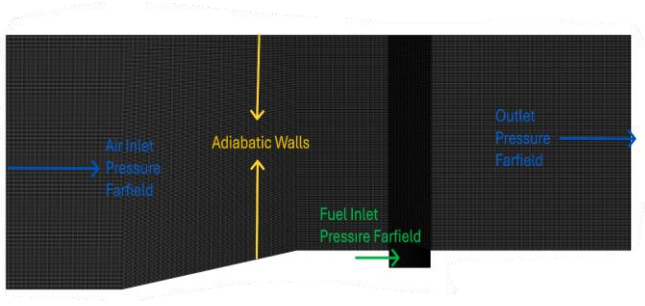

Fig.1 Computational domain

3. VALIDATION

The numerical model was validated through a two-stage process to ensure the reliability of the simulation results. First, a mesh independence study was conducted to determine the optimal number of grid elements required to achieve stable and accurate results. As shown in Figure 3(b) the normalized pressure value at the flameholder surface plateaued beyond 76,000 elements, with variations remaining below 0.1%, confirming numerical independence and justifying the selected mesh density for subsequent simulations. The second stage of validation involved direct comparison of numerical predictions with experimental data reported by Gruber et al. (2001). The experimental setup used in their study is schematically illustrated in Figure 2, including the combustor geometry and flameholder placement. Key validation metrics were extracted from the normalized pressure distribution along the flameholder surface, calculated as the ratio of local pressure to inlet pressure. A comparison of numerical and experimental results is presented in Figure 3 (a), demonstrating strong agreement in both trend and magnitude, particularly in the effective distance from the leading edge of the flameholder to the location of peak pressure. These results confirm the model's capability to accurately replicate critical flow features relevant to combustion stabilization in supersonic flow regimes. The validated mesh and numerical approach were then employed for further parametric investigations [17].

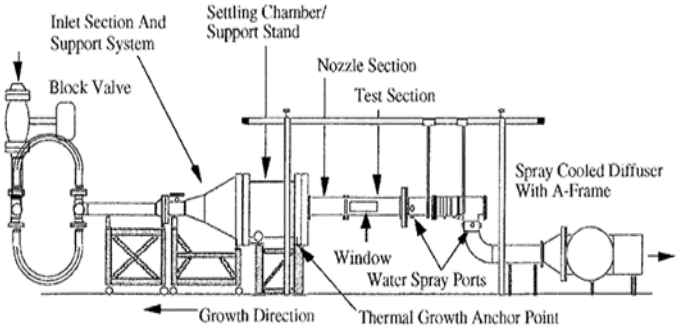

Fig.2. Experimental setup

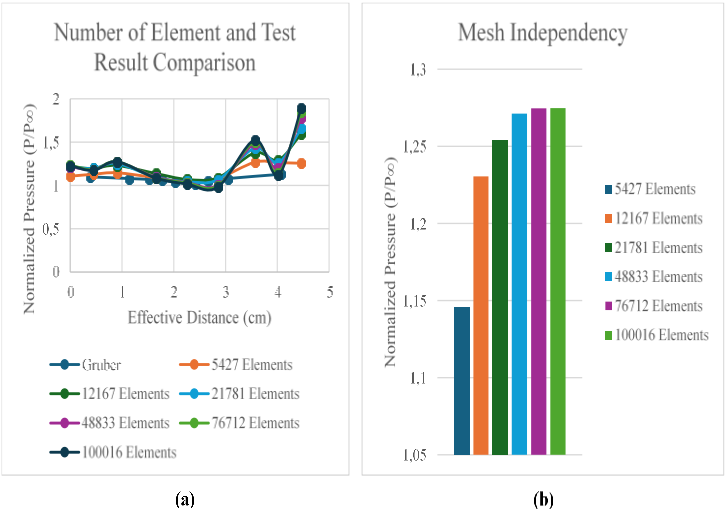

Fig.3. (a) Experimental and CFD results [18]. (b) Element number comparison

3.1. Cavity Geometry Validation

A detailed geometric analysis was performed to determine the optimal cavity configuration for effective flame stabilization in supersonic flow. Two critical geometric parameters were examined: the offset ratio (Du/D) and the rear wall ramp angle (θ). The offset ratio, defined as the ratio of the front to rear wall lengths, was evaluated at values of 1, 2, and 3. The comparison of normalized cavity pressure for these cases is shown in Figure 4, indicating that Du/D = 1 yields the highest pressure buildup within the cavity region. This pressure enhancement corresponds to stronger recirculation and increased fuel residence time—factors known to support stable combustion. Contour plots of pressure, velocity, and temperature for each offset ratio are presented in Figure 5 (a-c), where Du/D = 1 clearly demonstrates superior vortex formation and thermal buildup in the cavity, further supporting its selection.

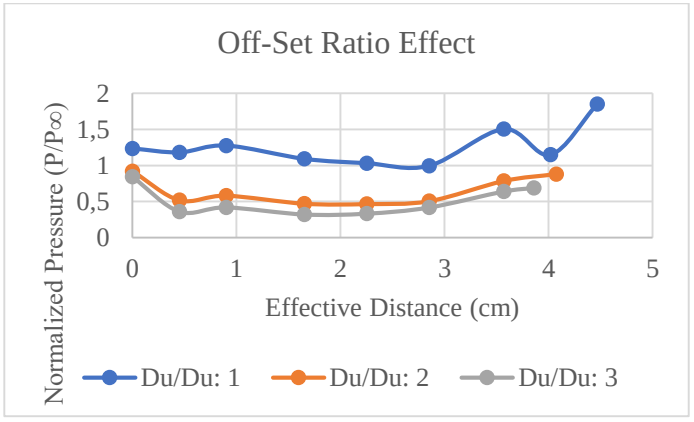

Fig.4 Comparison of O.R.

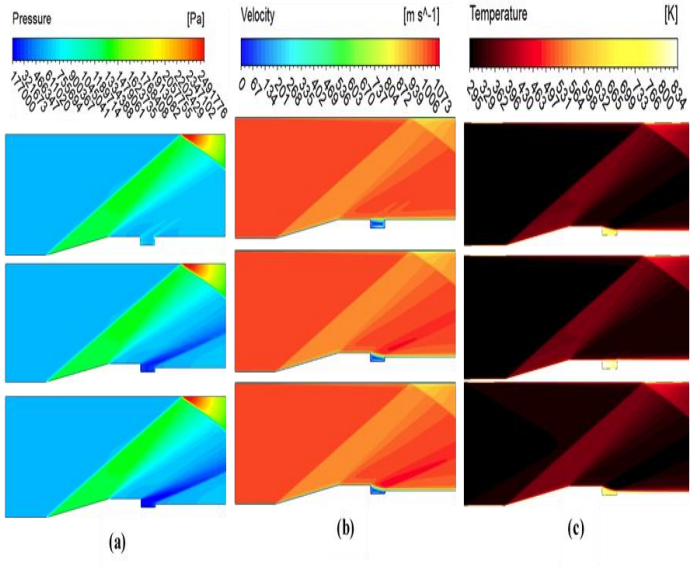

Fig.5. (a) Pressure contours of different O.R. (b) Velocity contours of different O.R. (c) Temp. contours of different O.R.

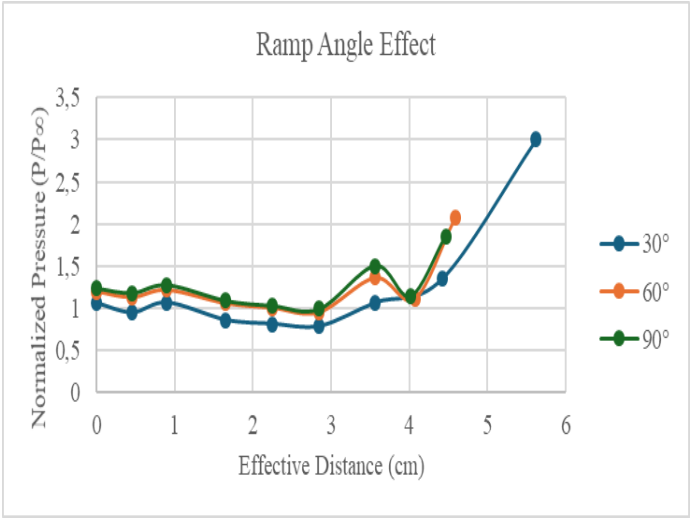

Fig.6. Comparison of ramp angles

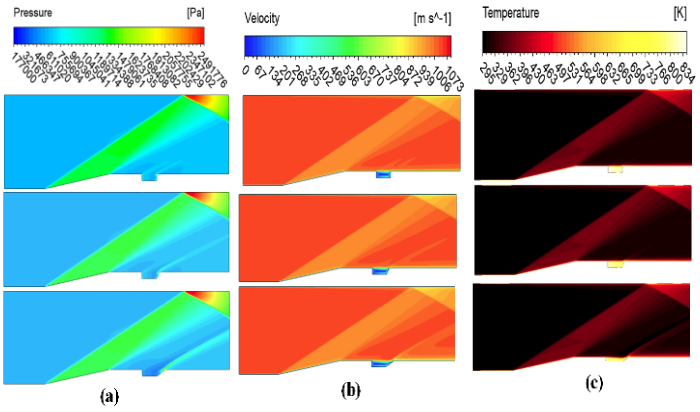

Fig.7. (a) Pressure contours of different ramp angles (b) Velocity contours of different ramp angles (c) Temp. contours of different ramp angles.

After identifying Du/D = 1 as optimal, the influence of the rear wall ramp angle was investigated by comparing 90°, 60°, and 30° configurations. As shown in Figure 6, which compares normalized pressure across these ramp angles, the differences were marginal. Although the 30° case displayed slight flow non-uniformities near the trailing edge, as seen in the contour plots of Figures 3.2.6 to 3.2.8, the overall pressure, velocity, and temperature distributions remained largely consistent across all angles. These findings confirm that while the offset ratio significantly impacts cavity performance, the ramp angle plays a secondary role. Therefore, the rectangular cavity with Du/D = 1 and rear wall angles of 90° and 60° was selected for subsequent combustion analysis and parametric studies.

4. VALIDATION PARAMETRIC STUDIES

To evaluate the influence of injector placement and pressure on combustion performance, a parametric investigation was carried out using the validated rectangular and trapezoidal cavity geometries. The configuration of both cavity types, along with the location of top, middle, and bottom injectors, is depicted in Figure 8. Each case was analyzed at three injection pressures (1 atm, 2 atm, and 3 atm), and the results are interpreted through pressure, velocity, temperature, and hydrogen concentration contours. These four variables collectively describe the flameholding potential and fuel–air mixing efficiency in supersonic conditions.

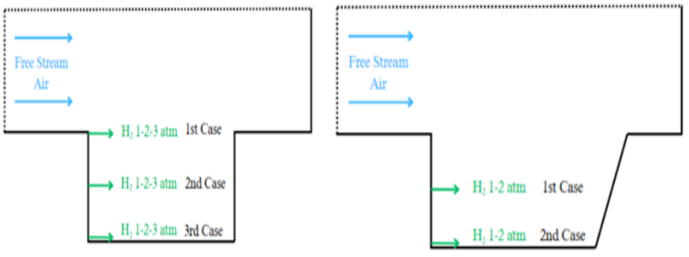

Fig.8. Rectangular and trapezoidal cavity configuration

At 1 atm injection pressure, bottom injection yielded the most effective flame anchoring conditions. The pressure distribution was more uniform and elevated within the cavity compared to middle and top injection, which suffered from underdeveloped recirculation zones and low cavity pressure. Velocity contours confirmed strong vortex formation only in the bottom configuration, which promoted enhanced fuel residence and mixing. Correspondingly, temperature fields showed high thermal intensity concentrated near the cavity step, indicating robust combustion. Hydrogen distribution maps also revealed that bottom injections enable dense and uniform fuel mixing across the cavity. These trends, which are visualized in the four sub-contours of Figure 9, support the conclusion that bottom injection at 1 atm provides the most favorable aerodynamic and thermochemical characteristics for flame stabilization.

Increasing the injection pressure to 2 atm enhanced overall performance, particularly for the middle injection configuration. Compared to 1 atm, both pressure and temperature contours showed improved flameholding conditions, with middle injection producing the highest internal cavity temperature. Velocity fields reflected fully developed recirculation with a more symmetric flow pattern in the middle injection case, while bottom injection retained strong mixing behavior with slightly reduced thermal uniformity. Hydrogen concentration fields, especially in the cavity core, were denser and more uniformly distributed in the

middle injection case [19]. These combined effects, captured in Figure 10, suggest that 2 atm injection from the middle position achieves optimal balance between mixing efficiency and combustion stability.

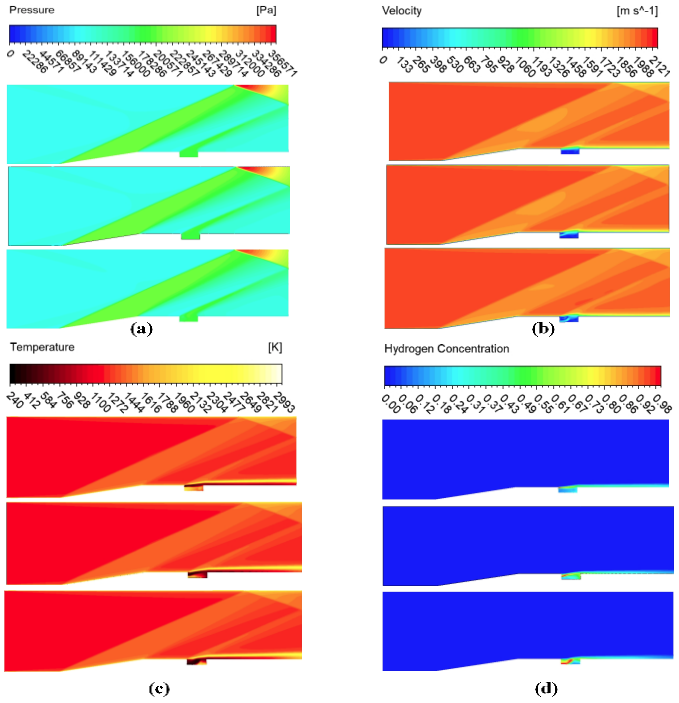

Fig.9. The three injection location at 1 atm (a) Pressure contours (b) Velocity contours (c) Temp. contours. (d) Hydrogen concentration.

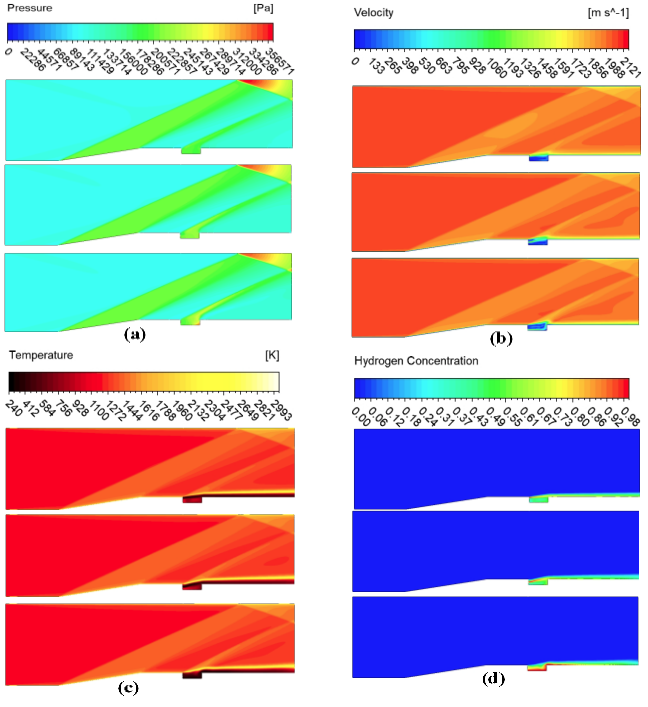

Fig.10. The three injection location at 2 atm (a) Pressure contours (b) Velocity contours (c) Temp. contours. (d) Hydrogen concentration.

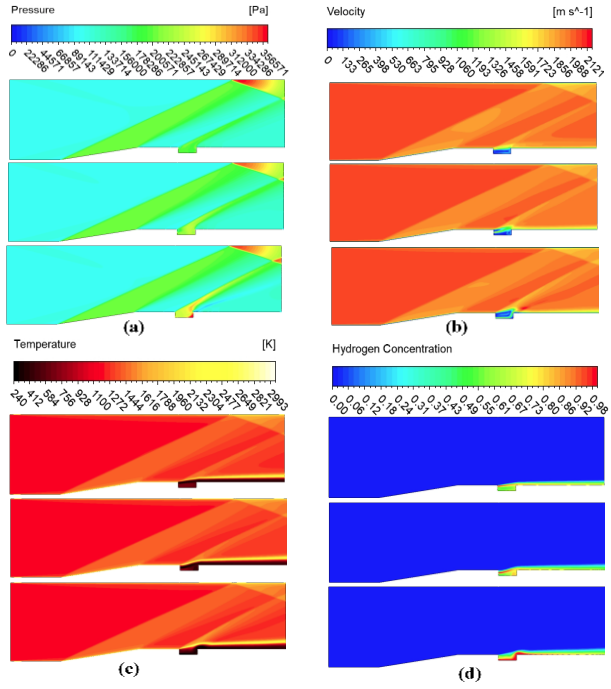

Fig.11. The three injection location at 3 atm (a) Pressure contours (b) Velocity contours (c) Temp. contours. (d) Hydrogen concentration.

At 3 atm injection pressure, performance began to deteriorate. Although pressure levels within the cavity increased further, the gradients became non-uniform and less stable, particularly in the bottom and middle injector configurations. The resulting pressure asymmetry introduced adverse flow structures, weakening the flameholding zone. Velocity contours demonstrated distorted recirculation, and temperature fields failed to show significant improvement over the 2 atm case. In fact, the temperature rise plateaued, and the hydrogen distribution became less compact and uneven. These findings, which are illustrated in Figure 11, indicate that excessive injection pressure can negatively affect flow stability and combustion uniformity, with diminishing returns above 2 atm.

Analysis of the 60° trapezoidal cavity geometry at 1 atm injection pressure demonstrated that both middle and bottom injector configurations produced viable flow recirculation. However, middle injection resulted in more homogeneous pressure distribution and temperature fields, while bottom injection concentrated combustion near the cavity base with higher thermal peaks. Velocity fields for both cases revealed functional vortex structures, although those from the bottom injection extended deeper into the cavity. Hydrogen concentration was denser in the lower cavity region for bottom injection, whereas middle injection promoted a more distributed mixture across the cavity center. These results, synthesized in Figure 12, suggest that middle injection may provide improved balance between stability and mixture uniformity in trapezoidal cavities operating at lower pressures.

At 2 atm, the trapezoidal geometry showed further improvements in combustion behavior. Both middle and bottom injection cases achieved strong and stable recirculation zones, as observed from velocity and hydrogen distribution contours. Pressure gradients remained smooth, and temperature fields revealed high thermal intensity distributed more evenly across the cavity length. Importantly, middle injection allowed the fuel to remain centered within the cavity, supporting enhanced residence time and mixing quality. These behaviors are documented in Figure 13, which highlights the enhanced flameholding and combustion efficiency attainable with moderate-pressure injection in optimized cavity geometries. Compared to the rectangular cavity, the trapezoidal form provided slightly lower peak temperatures but demonstrated more stable fuel retention and reduced thermal stress near solid boundaries.

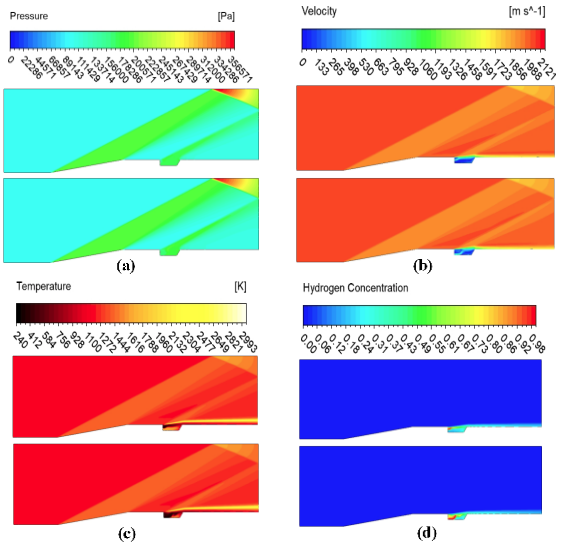

Fig.12. The Mid and Bottom Injection location of 60° backwall at 1 atm (a) Pressure contours (b) Velocity contours (c) Temp. contours. (d) Hydrogen concentration.

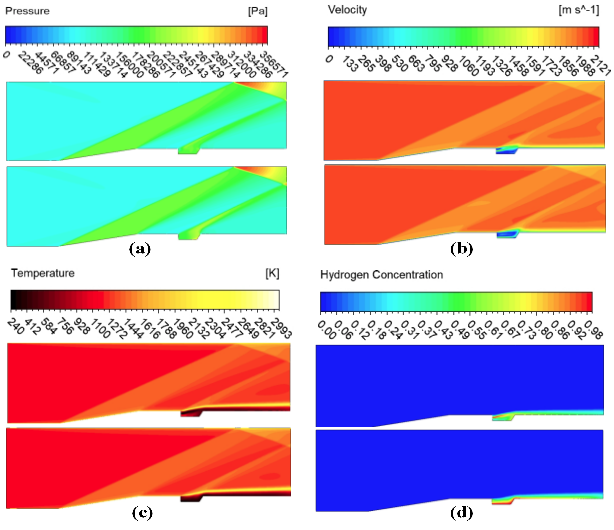

Fig.13. The Mid and Bottom Injection location of 60° backwall at 2 atm (a) Pressure contours (b) Velocity contours (c) Temp. contours. (d) Hydrogen concentration.

5. CONCLUSION

This study presented a comprehensive CFD-based investigation into the effects of cavity geometry and fuel injection configuration on flame stabilization in supersonic scramjet combustors. Two cavity types rectangular and trapezoidal were evaluated through parametric variations in offset ratio, ramp angle, injection location, and injection pressure. The simulation results validated against experimental data and subjected to mesh independence checks revealed significant dependencies between cavity design, injector setup, and combustion behavior.

Among the tested geometries, the rectangular cavity with an offset ratio of Du/D = 1 demonstrated the most effective vortex formation and pressure retention, supporting its selection for detailed analysis. While variations in ramp angle had a negligible impact on combustion-relevant flow fields, injection location and pressure were found to be critical. The middle injection at 2 atm provided the most balanced combination of pressure stability, thermal development, and fuel retention. This configuration consistently yielded strong recirculation, high combustion efficiency, and uniform hydrogen mixing. In contrast, top injection failed to promote adequate fuel-air interaction, and increasing the injection pressure to 3 atm did not produce significant performance benefits in some cases, it introduced flow instability.

Comparative analyses also indicated that the 60° trapezoidal cavity geometry, while slightly less efficient thermally, offered improved mixture distribution and lower thermal gradients along cavity walls. This may be advantageous in reducing thermal stress and material fatigue in practical applications.

Overall, the findings highlight the critical role of cavity design and injector strategy in determining scramjet combustor performance. The identified configuration rectangular cavity, centerline injection at 2 atm provides a promising design baseline for future experimental validation and hardware development. Future studies may extend these findings by incorporating angled or pulsed injection strategies, as well as exploring multi-element cavity interactions under transient flow conditions.

REFERENCES

[1] X. Li, Q. Lei, X. Zhao, W. Fan, S. Chen, L. Chen, Y. Tian and Q. Zhou, "Combustion Characteristics of a Supersonic Combustor with a Large Cavity Length to Depth Ratio," *Aerospace*, vol. 9, no. 4, p. 214, 2022.

[2] S. Huang, Q. Chen, Y. Cheng, J. Xian and Z. Tai, "Supersonic Combustion Modeling and Simulation on General Platforms," *Aerospace*, vol. 9, no. 7, p. 366, 2022.

[3] G. B. Goodwin, R. F. Johnson, D. A. Kessler, A. D. Kercher and H. K. Chelliah, "Effect of Inflow Turbulence on Premixed Combustion in a Cavity Flameholder," arXiv preprint, arXiv:2001.05893, 2020. [Online]. Available: https://arxiv.org/abs/2001.05893

[4] M. Lin, J. Fang, X. Deng, X. Gu and Z. X. Chen, "Direct numerical simulation of inflow boundary-layer turbulence effects on cavity flame stabilisation in a model scramjet combustor," Aerosp. Sci. Technol., vol. 165, p. 110463, 2025.

[5] E. B. Jeong, S. O'Byrne, I. S. Jeung and A. F. P. Houwing, "The Effect of Fuel Injection Location on Supersonic Hydrogen Combustion in a Cavity Based Model Scramjet Combustor," *Energies*, vol. 13, no. 1, p. 193, 2020.

[6] Y. Zhang, Y. Chen and Y. Sun, "Numerical and experimental examination of strut plus wall injection in a scramjet combustor," *Advances in Mechanical Engineering*, Springer, 2025.

[7] Y. Sun, F. Li, J. Zhu *et al.*, "Effects of Additional Cavity Floor Injection on Ignition and Combustion in a Mach 2 Supersonic Flow," *Energies*, vol. 13, no. 18, p. 4801, 2020.

[8] Z. Liu *et al.*, "Ignition and flame stabilization in an ethylene-fueled cavity stabilized scramjet engine," *Proc. EUCASS Conf.*, 2022.

[9] N. Relangi, A. Ingenito and S. Jeyakumar, "Implications of Injection Locations in an Axisymmetric Cavity-Based Scramjet Combustor," *Energies*, vol. 14, p. 2626, 2021.

[10] F. Li, M. Sun, Z. Cai, Y. Chen, Y. Sun, F. Li and J. Zhu, "Effects of additional cavity floor injection on the ignition and combustion processes in a Mach 2 supersonic flow," Energies, vol. 13, no. 18, p. 4801, 2020

[11] Y. Zhang, Y. Chen and Y. Sun, "Characteristics of Flame Stabilization Enhancement in a Strut Based Supersonic Combustor," *Advances in Mechanical Engineering*, Springer, 2025.

[12] X. Li *et al.*, "Supersonic Combustion Mode Analysis of a Cavity Based Scramjet," *Aerospace*, MDPI, 2022.

[13] Z. Meng, C. Shen, K. Jia and H. He, "Numerical study on flame stabilization by shock-induced in a supersonic combustor with parallel-cavity: Symmetric configuration," Acta Astronaut., vol. 232, pp. 721–733, 2025

[14] B. Lukovic, P. Orkwis, M. Turner and B. Sekar, "Effect of cavity L/D variations on neural network-based deterministic unsteadiness source terms," in Proc. 40th AIAA Aerospace Sciences Meeting & Exhibit, Reno, NV, USA, 2002, p. 857, AIAA Paper 2002-0857.

[15] G. Choubey, M. Solanki, T. Bhatt, G. Kshitij, D. Yuvarajan and W. Huang, "Numerical investigation on a typical scramjet combustor using cavity floor H2 fuel injection strategy," *Acta Astronautica*, vol. 202, pp. 373–385, Jan. 2023.

[16] M. R. Gruber, R. A. Baurle, T. Mathur and K. Y. Hsu, "Fundamental studies of cavity-based flameholder concepts for supersonic combustors," *Journal of Propulsion and Power*, vol. 17, no. 1, pp. 146–153, 2001.

[17] M. Yüzücü, "Numerical Investigation of the Effect of Flameholder Geometry on Air-Fuel Mixing in Scramjet Engines," M.S. thesis, 2024.

[18] Z. Cai, M. Sun, Z. Wang and X. S. Bai, "Effect of cavity geometry on fuel transport and mixing processes in a scramjet combustor," *Aerospace Science and Technology*, vol. 80, pp. 309–314, Sep. 2018.

[19] T. Roos, A. Pudsey, M. Bricalli and H. Ogawa, "Cavity enhanced jet interactions in a scramjet combustor," *Acta Astronautica*, vol. 157, pp. 162–179, Apr. 2019.

International Journal of Energy Horizon 01 (2025) 8-10

International Journal of Energy Horizon

journal homepage: https://dergipark.org.tr/tr/pub/ijeh

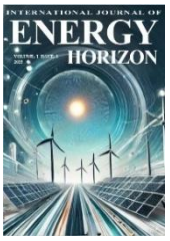

Research Paper

Compared Economic Assessment of Selected Thermochemical Cycles Utilizing Next-Gen Nuclear Reactors Using IAEA's HEEP

Onur BAYRAM[1,*], Alperen TOZLU[2]

[1]Ankara Yıldırım Beyazıt University, Faculty of Engineering and Natural Science, Mechanical Engineering Department, Ankara, 06010, Turkey
[2]Bayburt University, Faculty of Engineering, Mechanical Engineering Department, Bayburt, 69000, Turkey
[1]ORCID No:0009-0009-2582-4325
[2]ORCID No:0000-0002-2610-5279

ARTICLE INFO

Article History:

Received:29 May 2025
Revised:2 June 2025
Accepted:20 June 2025
Available online:30 June 2025

Keywords:

Hydrogen production
Thermochemical cycles
HEEP software

ABSTRACT

This study presents an economic comparison of four hybrid thermochemical hydrogen production cycles powered by nuclear energy, using the IAEA's HEEP software. The analysis includes estimations of capital expenditures (CAPEX) for each cycle, calculated as $200 million for HyS, $264 million for CuCl, $462 million for MgCl, and $210 million for CaBr. Based on these estimates, the corresponding hydrogen production costs are determined to be below $2.80/kg for HyS, $2.99/kg for CuCl, and $3.61/kg for MgCl. The cost for the CaBr cycle falls within the range of $2.86–$3.03/kg. Although the HyS cycle is no longer pursued due to challenges associated with its electrolysis step, the CuCl cycle emerges as the most economically favorable and thoroughly investigated alternative among the evaluated options.

1. INTRODUCTION

Thermochemical cycles are recognized for their potential to lower hydrogen production costs and improve efficiency. However, their reliance on high operating temperatures introduces significant safety risks and technical challenges, including issues related to material stability and operational longevity [1,6,8,12]. To address these limitations, hybrid cycles have been developed, which combine thermal energy with electricity input to facilitate specific reaction steps [5]. These hybrid thermochemical processes are particularly attractive due to their ability to operate at comparatively lower temperatures by integrating at least one electrochemical step, often involving electrolysis.

The first notable example of such a system is the ISPRA Mark 11, also known as the Westinghouse HyS cycle. It operates at a peak temperature of 1120 K and features a low-voltage electrolysis step (~0.16 V), aiming to balance efficiency and operational simplicity. While its high-temperature requirement might suggest feasibility concerns, its cyclic operation avoids complex chemical handling and has demonstrated performance levels comparable to those of more intricate high-temperature thermochemical cycles [7]. The Cu-Cl cycle, initially introduced in hybrid form by Dokiya and the U.S. Institute of Gas Technology [2], presents a maximum reaction temperature of about 800 K—substantially lower than that required for pure thermolysis. Although early progress was limited, interest in the Cu-Cl cycle was renewed decades later, and it has since become one of the most extensively researched hydrogen production methods [14]. Ongoing research is supported by institutions such as Argonne National Laboratory (ANL), Atomic Energy of Canada Limited (AECL), and Ontario Tech University.

Other noteworthy hybrid cycles include the modified CaBr cycle, adapted from the UT-3 process, which operates at around 1020 K and involves an electrolysis step requiring 0.8 V, and the Mg-Cl cycle, which is a refinement of the chlorine-based hybrid cycle, functioning at 730 K with an electrolysis voltage of 0.99 V. A

*Corresponding author
E-mail address: onurbayram24@aybu.edu.tr
journal homepage: https://dergipark.org.tr/tr/pub/ijeh

schematic overview of these hybrid thermochemical cycles is provided in Figure 1.

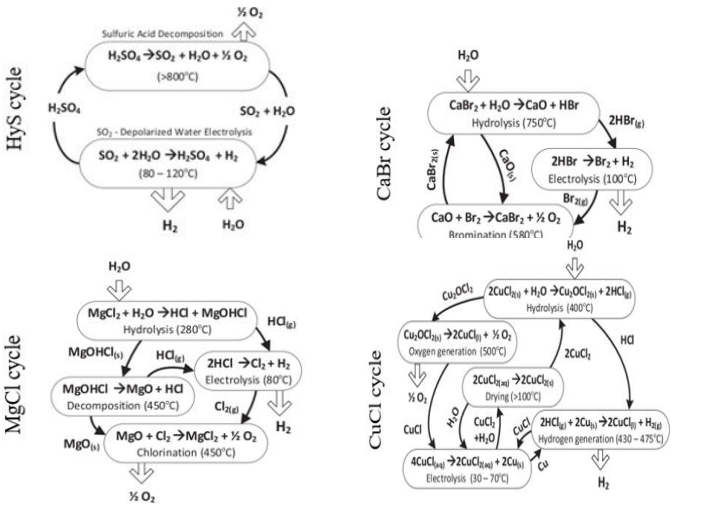

Fig. 1. Schematics of selected hybrid thermochemical cycles (adapted from [3])

2. MATERIALS AND METHODS

The HEEP software is employed to carry out economic evaluations of selected hybrid thermochemical cycles through a series of case studies [3]. As the current HEEP database lacks specific data on medium-temperature nuclear reactors, customized scenarios are created by incorporating key parameters such as thermal power output, efficiency, and the distribution of thermal energy between power generation and hydrogen production systems. Ideally, cost analyses for the MgCl and Cu-Cl cycles should be based on reactors like the SCWR or other comparable nuclear systems operating at similar thermal capacities. However, due to their absence in the HEEP database, the High Temperature Gas Reactor (HTGR) is adopted as the reference source for both heat and electricity supply in the simulations [9]. Figure 2 presents the thermal output characteristics and associated economic parameters of the HTGR as listed in the HEEP database, along with the relevant data for the modeled hydrogen production plants.

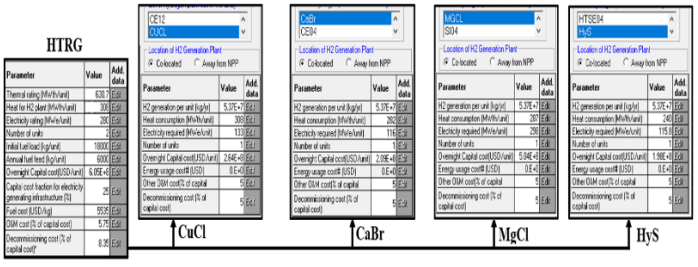

Fig 2. Thermal rating and economic data of the high temperature gas reactor at HEEP database (a) and corresponding hydrogen generation plants (b) CuCl, (c) MgCl (d) CaBr (e) HyS

3. RESULTS AND DISCUSSION

The HEEP (Hydrogen Economic Evaluation Program) tool was used to evaluate and tabulate the economic performance of selected hybrid thermochemical hydrogen production cycles, as summarized in Table 1. For the Cu-Cl cycle, the system requires approximately 133.1 MJ of electricity and 308 MJ of thermal energy per kilo mole of hydrogen under practical operating conditions. Given a thermal-to-electric conversion efficiency near 50% for the High Temperature Gas Reactor (HTGR), this implies that about 270 MJ of thermal input is needed for electricity generation, leading to a total thermal energy demand of around 580 MJ per kilo mole of hydrogen produced. In configuring the reactor system, both the thermal and electrical demands are taken into account. Within HEEP, when a power generation module is integrated into the plant design, the software automatically assigns 25% of the capital expenditure (CAPEX) to the power generation infrastructure. Based on energy input, the system is expected to generate 1 kilo mole of hydrogen per second, equating to approximately 2 kg/s. On an annual basis, assuming an 85% capacity factor, this results in 53.7 million kg of hydrogen production.

The CAPEX for a large-scale Cu-Cl plant operating at this capacity is estimated at USD 264 million. Notably, a major portion of this cost is associated with electrolyzer units, although reactor size and auxiliary systems also contribute significantly. The levelized cost of hydrogen (LCOH) for this configuration is determined to be approximately $2.99/kg, with the bulk of this cost attributed to capital and operation & maintenance (O&M) expenses. For the Mg-Cl cycle, which follows a three-step configuration, theoretical thermal and electrical demands are 152 MJ and 191 MJ per kg of hydrogen, respectively. However, drawing comparisons directly to Cu-Cl is problematic, as practical considerations such as lower reaction yields, higher steam-to-metal ratios, and extended residence times significantly impact real-world performance. A more representative evaluation, as discussed in Ozcan & Dincer [10], suggests practical heat and power requirements of 287 MJ and 298 MJ per kg of hydrogen. Consequently, the associated plant CAPEX is markedly higher—estimated at USD 462 million for the same annual hydrogen output. This results in a hydrogen production cost of around $3.61/kg, which is consistent with previous exergoeconomic analyses of enhanced four-step MgCl cycles, reporting LCOH values up to $3.87/kg [11]. Interestingly, due to greater electricity generation capacity in this configuration, electricity unit cost is slightly lower. However, the share of electrolyzer-related CAPEX is as high as 30%, reflecting the system's high dependence on electricity-driven reactions.

The Hybrid Ca-Br cycle, a variant of the UT-3 process, has received comparatively limited attention due to its high-temperature operation requirements. Nevertheless, preliminary economic projections can be made by aligning its operational profile with that of high-temperature reactor systems [13]. The Ca-Br cycle requires roughly 116 MJ of thermal energy and 282 MJ of electrical energy per kilo mole of hydrogen. Using ideal assumptions, the total CAPEX is estimated at USD 210 million for an annual production of 53.7 million kg of hydrogen. This results in a hydrogen cost of approximately $2.86/kg. However, in less-than-ideal scenarios—where elevated steam-to-metal ratios and substantial overpotentials increase electrolysis energy consumption—CAPEX may rise by 30%, pushing hydrogen costs up to around $3.03/kg. In the base-case scenario, about 20% of the total hydrogen cost stems from capital expenses; under more demanding conditions, this share could increase significantly.

The final case study focuses on the HyS (Hybrid Sulfur) cycle, widely recognized as one of the most mature hybrid thermochemical cycles. It utilizes a depolarized electrolysis step involving sulfur dioxide (SO_2), which theoretically reduces the electrical energy demand to about 15% of that required for conventional water electrolysis. However, in practice, significant overpotentials can elevate the actual cell voltage beyond 0.6 V—nearly triple the theoretical value [4]. For a more grounded estimation, an operational voltage of 0.4 V is assumed in this study, raising the total power consumption by roughly 50%. The HTGR reactor contribution is lower in this configuration since only one major thermal decomposition step is present. Nevertheless, the higher operational temperature requirements introduce additional engineering and cost challenges. Under these assumptions, the total CAPEX of the HTRG-HyS system is estimated at USD 200 million, resulting in a hydrogen cost of around $2.80/kg. Despite accounting for realistic overpotentials and thermal demands, the HyS cycle still delivers the lowest hydrogen production cost among the cycles studied—highlighting its economic promise, provided that electrolysis system complexity and safety can be effectively managed.

Table 1. HEEP results summary for the cycles

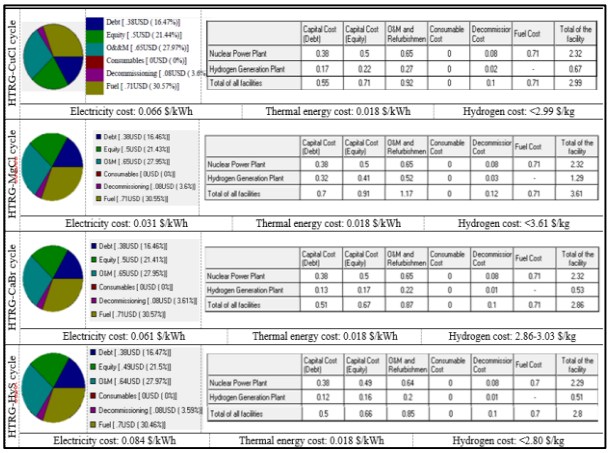

From a broader perspective, this comparative assessment reveals key trade-offs between capital intensity, reaction temperature, and electrochemical efficiency

across hybrid thermochemical cycles. While the Cu-Cl cycle offers a compelling compromise between system complexity and cost, its reliance on high-performance electrolyzers may pose scalability concerns. The Mg-Cl cycle, although chemically promising, suffers from significant CAPEX inflation when practical parameters are included, making it less economically attractive in the near term. The Ca-Br cycle stands out for its moderate CAPEX and flexible thermal integration, although it lacks the maturity and experimental validation of other options. The HyS cycle, despite technical difficulties associated with SO_2 handling and high-temperature electrolysis, remains cost-competitive largely due to its favorable energy distribution and simplified reaction steps. However, future advancements in materials for high-temperature electrochemical cells and improved integration with advanced nuclear systems (e.g., Gen-IV reactors) may dramatically alter the cost landscape, particularly for high-temperature cycles like Mg-Cl and Ca-Br.

4. CONCLUSIONS

Despite ongoing research and development efforts, none of the evaluated hybrid cycles are fully mature for commercial deployment. The HyS cycle appears to be the most technologically advanced and closest to market readiness, supported by pilot-scale demonstrations and a more established research foundation. However, both HyS and Cu-Cl cycles face significant technical barriers, particularly in the domain of electrochemical process development. High-temperature and depolarized electrolysis technologies remain complex, energy-intensive, and prone to degradation, which currently limits their scalability and commercial feasibility. The Mg-Cl cycle, although based on the well-established hydrochloric acid electrolysis process—which has been used in industrial applications for decades—yields significantly higher hydrogen production costs under realistic process conditions. These costs are primarily driven by elevated electricity consumption and associated capital requirements for electrolysis infrastructure. While theoretical or idealized evaluations may suggest hydrogen production costs below $3/kg, such values are overly optimistic and do not reflect the technical and operational constraints observed in practice. Future progress will depend on coordinated R&D efforts that span thermochemical engineering, advanced materials science, and nuclear-thermal system integration. In parallel, software tools such as HEEP should evolve to include a broader spectrum of reactor types, enabling more precise economic modeling of medium-temperature cycles. Only through such holistic and interdisciplinary approaches can hybrid thermochemical hydrogen production evolve into a commercially viable and sustainable energy pathway.

ACKNOWLEDGEMENT

This short paper is prepared as part of an IAEA Coordinated Research Project titled “Assessing technical and economic aspects of nuclear hydrogen production for near-term development” I35006 under Contract No: 22554.

REFERENCES

[1] L. E. Brecher, S. Spewock and C. J. Warde, "The Westinghouse Sulfur Cycle for the thermochemical decomposition of water," Int. J. Hydrogen Energy, vol. 2, no. 1, pp. 7–15, 1977.

[2] M. Dokiya, T. Kameyama and K. Fukuda, "Thermochemical hydrogen preparation—Part V. A feasibility study of the sulfur iodine cycle," Int. J. Hydrogen Energy, vol. 4, pp. 267–277, 1979.

[3] R. S. El-Emam, H. Ozcan and I. Dincer, "Comparative cost evaluation of nuclear hydrogen production methods with the Hydrogen Economy Evaluation Program (HEEP)," Int. J. Hydrogen Energy, vol. 40, no. 34, pp. 11168–11177, 2015.

[4] T. B. Ferriday and P. H. Middleton, "Alkaline fuel cell technology—A review," Int. J. Hydrogen Energy, vol. 46, no. 35, pp. 18489–18510, 2021.

[5] K. S. Gabriel, R. S. El-Emam and C. Zamfirescu, "Technoeconomics of large-scale clean hydrogen production – A review," Int. J. Hydrogen Energy, vol. 47, no. 72, pp. 30788–30798, 2022

[6] M. Kochański et al., "The technical and economical perspectives for the production and storage of hydrogen in Poland," Acta Innov., vol. 8, pp. 50–62, 2013.

[7] T. Kodama and N. Gokon, "Thermochemical Cycles for High-Temperature Solar Hydrogen Production," Chem. Rev., vol. 107, no. 10, pp. 4048–4077, 2007.

[8] G. F. Naterer et al., "Canada’s program on nuclear hydrogen production and the thermochemical Cu–Cl cycle," Int. J. Hydrogen Energy, vol. 35, pp. 10905–10926, 2010.

[9] M. Orhan, I. Dincer and G. Naterer, "Cost analysis of a thermochemical Cu–Cl pilot plant for nuclear-based hydrogen production," Int. J. Hydrogen Energy, vol. 33, pp. 6006–6020, 2008.

[10] H. Ozcan and I. Dincer, "Modeling of a new four-step magnesium–chlorine cycle with dry HCl capture for more efficient hydrogen production," Int. J. Hydrogen Energy, vol. 41, no. 19, pp. 7792–7801, 2016.

[11] H. Ozcan and I. Dincer, "Exergoeconomic optimization of a new four-step magnesium–chlorine cycle," Int. J. Hydrogen Energy, vol. 42, no. 4, pp. 2435–2445, 2017.

[12] H. Ozcan, R. S. El-Emam and B. A. Horri, "Thermochemical looping technologies for clean hydrogen production – Current status and recent advances," J. Cleaner Prod., vol. 382, p. 135295, 2023.

[13] H. Ozcan and H. Fazel, "Cost assessment of selected nuclear driven hybrid thermochemical cycles for hydrogen production," Int. J. Hydrogen Energy, vol. 54, pp. 554–561, 2024..

[14] K. Pope, Z. Wang and G. F. Naterer, "Process integration of material flows of copper chlorides in the thermochemical Cu–Cl cycle," Chem. Eng. Res. Des., vol. 109, pp. 273–281, 2016.

International Journal of Energy Horizon 01 (2025) 11-19

International Journal of Energy Horizon

journal homepage: https://dergipark.org.tr/tr/pub/ijeh

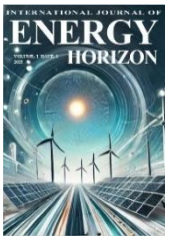

Research Paper

Effect of Metal Foam Material Type and Porosity Pattern on Melting and Flow Dynamics in A Vertical Rectangular Cavity

Emrehan GÜRSOY[1,*]

[1]Audit Department, Kardemir Karabük Iron Steel Industry Trade & Co. Inc., Karabük, Türkiye
[1]ORCID No:0000-0003-2373-3357

ARTICLE INFO

Article History:

Received:13 June 2025
Revised: 17 June 2025
Accepted: 23 June 2025
Available online: 30 June 2025

Keywords:

Different metal foam
Heat transfer enhancement
Latent heat thermal energy storage
Melting
Phase change material

ABSTRACT

Phase change materials have an important role in the field of energy storage. However, due to their low thermal conductivity, transferring applied heat to the entire system is difficult. It negatively affects the lack of use of the systems. Researchers are investigating many applications to prevent this and increase the thermal conductivity of the system. One of these methods is the application of metal foam (MF) embedded inside the phase change material (PCM) in the system. This study investigated the melting and natural convection characteristics of a 2D-designed rectangular cavity, and copper and aluminium MFs were placed inside this cavity, which was separated into two equal compartments. The porosity of these MFs was ε=0.90 and 0.95, and their proximity to the heat source was examined. The Brinkman-Forchheimer extended Darcy model was used in the cases solved based on the finite volume and enthalpy-porosity method. The results showed that RC4 is the case that shows the fastest melting performance, and the solid-liquid interface is not affected by natural convection. Increasing the porosity from ε=0.90 to 0.95 caused natural convection to occur. In these parameters, natural convection increases the thermal resistance and makes it difficult to transfer heat to unmelted phase change materials. It was determined that RC1 is the case that shows the fastest melting after RC4. The melting times of RC4 in Section 1 (S1) and Section 2 (S2) are 2.5 and 1.4 times faster than RC1, respectively. Besides, the placement of MF and porosity significantly affected the Nusselt number (Nu). The average Nu of RC4 is higher than that of RC1, and RC5 at the rate of 34.4% and 48.4%, respectively. As melting progressed, a stationary region was formed in the center of the cavity due to melted PCM moving upward from the hot wall to the cold section.

1. INTRODUCTION

Renewable energy sources, such as solar, wind, hydroelectric, etc., offer high amounts of usable energy, and the amount of instantaneous energy provided by solar is especially much higher than the current human usage needs **[1]**. However, the sustainability of these sources is very limited because of daily, seasonal, and yearly changes **[2]**. Considering these limitations and the ecological impacts of non-renewable energy sources, it is necessary to take action to store energy from a high-capacity source. Energy storage collects energy when it is in excess and makes it available when demand is high **[3]**. Energy can be stored with the help of several methods: thermal, mechanical, chemical, magnetic, and electric **[4]**. Each of these methods is a remarkable method, and the leading method among them is thermal energy storage (TES). TES systems are engineered to store thermal energy through heating, cooling, melting, condensation, or vaporization of a material. Based on the temperature range of operation, these materials are maintained at elevated or reduced temperatures within an insulated container. The stored energy is then retrieved for various purposes, including residential and industrial applications such as space heating or cooling, hot water generation, or power production.

Thermal energy can be stored in many ways and this classification has been presented by **[5]**. As stated in their study, sensible, latent, and thermo-chemical methods carry out the storage process in TES. Among these methods, the latent heat thermal energy storage (LHTES) method uses phase change material (PCM). This material has become the focus of more research and interest compared to other methods due to its advantages, such as high heat storage capacity, isothermal behaviour during melting and freezing processes, and minimum system size **[6, 7]**.

Although PCM has significant advantages, there are also serious disadvantages to its use in thermal systems, such as low thermal conductivity. However, it has been proven by many researchers using experimental and numerical analyses that this disadvantage can be improved by making enhancement applications, including metal foams (MFs), nanoparticles, magnetic fields, etc., on the systems, and some of these studies in renewable energy systems are numerically investigated an innovative 3D photovoltaic thermal (PVT) system integrated with PCM and MF **[8]**. By introducing copper (Cu) MF with varying porosities (ε) within the PCM compartment and employing nanofluid as the working fluid, the research evaluates the effects of parameters such as mass flow rate, nanofluid concentration, and ε on thermal and electrical performance.

*Corresponding author
E-mail address: emrehangursoy@gmail.com
journal homepage: https://dergipark.org.tr/tr/pub/ijeh

Results indicate that increasing ε from 0.2 to 0.8 enhances thermal efficiency by 33%, with a slight electrical efficiency decrease of 2.6%. Additionally, the PVT/PCM+Cu MF system achieves a 25.4% higher thermal efficiency compared to the PVT/PCM configuration, underscoring the effectiveness of incorporating Cu MF. To enhance the melting rate of MF composite PCM, partial and gradient optimizations of the MF pore densities (ω) were explored by Li et al. **[9]**. Among the partially optimized models, Partial-80-5-5 exhibited the most efficient melting, highlighting that increasing ω in the top region significantly accelerates the melting process. Further analysis of models with varying top-region ω confirmed that higher densities lead to faster melting. Gradient optimizations, such as Gradient-80-40-5, achieved the fastest melting rate overall. This performance is attributed to strong vortex formation at the bottom region, induced by suppressed natural convection in the top and middle regions with high ω. Ami Ahmadi et al. explored using gradient MFs with graded ε to improve TES performance.

Numerical simulations of a shell-and-tube TES unit showed that arranging MFs with ε ranging from 0.65 to 0.94 in the PCM domain reduces charging time and entropy generation **[10]**. Optimized designs achieved a 3.35% faster charging time and 7.96% lower entropy generation compared to uniform ε, demonstrating the effectiveness of gradient MFs. Prasanth et al. focused on enhancing the thermal conductivity of PCMs for solar thermal energy storage using Cu MF and Cu/aluminium (Al) wire-woven MF structures **[11]**. LHTES systems with a 300 KJ capacity were designed. Both PCM-Al wire woven MF and PCM-Cu MF composites exhibited similar melting times, but the heat extraction performance of the Al wire woven MF was comparable to Cu MF. Thermal efficiency ranged from 60–70% with water and 80–85% with air as heat extraction media. Heat extraction lasted 3–4 hours with cold water and 7–8 hours with cold air, increasing the outlet temperature by 2–2.5 times the inlet temperature. A pore-scale numerical model is developed by Parida et al. to simulate the melting of PCMs in PCM-MF composite energy storage systems **[12]**.

Unlike volume-averaged approaches, this model resolves the MF geometry, enabling accurate analysis of ω, distribution, and localized heat transfer at the PCM-MF interface. Incorporating convection effects, the model uses an enthalpy-based Finite Volume Method (FVM) and is validated against experimental data. Results show that convection significantly enhances melting and energy storage rates, particularly for MFs with higher ε and larger ω. Nie et al. investigated the effect of geometry on the melting and solidification behaviour of PCMs in seven vertical shell-tube LHTES systems **[13].** Both pure PCM (paraffin RT82) and composite PCM (paraffin RT82 embedded in Cu MF) are examined. A two-dimensional numerical model based on the enthalpy-porosity method (EPM) is developed and validated with experimental data. Results show that the conical shell system enhances natural convection, while the frustum tube system improves both convection and conduction. Geometry modification reduces melting time by at least 9.2% for pure PCM and 5.9% for composite PCM. The frustum tube system outperforms the conical shell system in both melting and solidification processes, regardless of the MF or working fluid used. Karimi et al. explored the use of PCMs in LHTES systems for buildings, addressing the issue of low thermal conductivity that limits charge/discharge rates **[14]**.

A new design incorporating a helical coil filled with PCM on both sides and Cu MFs (ε=0.9 and ω=12 PPI) in the inner region is proposed to enhance heat transfer. The effects of parameters such as HTF inlet flow rate, temperature, and MF on thermal performance are analysed experimentally. Results show that MF can reduce charge/discharge time by up to 57%, with greater reductions observed at higher inlet working fluid temperatures. Increasing the working fluid flow rate slightly shortens charging time, especially with MF, and accelerates discharge time, with faster depletion at lower working fluid inlet temperatures. Ghalambaz et al. investigated the effect of MF layer configurations on melting time in a system with parallel channel enclosures **[15]**. Three configurations were tested: half-split, L-shape, and diagonal foam layers. The optimal design was a horizontal split with a light foam layer at the top, which reduced charging time by 32%, completing the process in 837 seconds. Liu et al. examined the use of MF structures with varying ε gradients and multiple PCMs with different melting points to enhance PCM melting and improve system efficiency **[16]**.

Results show that using multiple PCMs reduced melting time by 9.18% compared to a single PCM with uniform MF. A multi-PCM system with ε=0.90 was tested with one-dimensional and two-dimensional porosity gradients. The one-dimensional positive gradient reduced melting time by 6.18%, while the negative gradient increased it by 19.78%, though the negative gradient minimized temperature non-uniformity. The optimal two-dimensional gradient model reduced melting time by 17.96% and increased energy storage efficiency by 20.16% compared to the single PCM system with uniform ε. A dimensionless analysis was also conducted to model liquid fraction (β) about Fourier, Stefan, and Rayleigh numbers. Joshi and Rathod, compared the thermal performance of fins and MF infusion in LHTES systems with identical compactness factors **[17]**. An experimental test rig validated a numerical model based on the coupled EPM. Results show that fins enhance thermal transport by 50% during melting and 5.56% during solidification compared to pure PCM. MF infusion improves thermal transport by 16.67% during melting and 33.33% during solidification. Fins accelerate melting by 66.67%, but MF enhances solidification by 29.41%. Overall, MF reduces total cycle time by 15%, making it a more effective thermal performance enhancer than fins. This numerical study conducted by Haddad et al. optimized the melting performance of TES partially filled with MF **[18]**.

A FVM based on the EPM was used for simulations, exploring the effects of foam location, ε, and nanoparticle volume fraction. The results show that inserting the MF layer diagonally from the top left to right bottom minimizes melting time. Compared to pure PCM, the melting time increases by 77.7%, while stored energy decreases by 6.7%. The optimal ε is 0.88, offering nearly the same stored energy as pure PCM with a 4% deviation. Adding nanoparticles enhances the melting rate by 8% but reduces stored energy by 3%. Hybrid systems combining MF at optimal ε and nanoparticles are more efficient than using each technique separately. Mehryan et al. investigated the melting heat transfer of capric acid PCM in a TES, using Cu nanoparticles and Cu MF to improve charging time **[19]**.

The EPM, combined with the FVM, simulates the free convection melting heat transfer of composite PCM. The ε, shape of the Cu MF layer, and nanoparticle volume fraction were optimized using the Taguchi approach to minimize charging time. Results showed that a left-right triangle porous zone minimized charging time. Higher ε and nanoparticle volume fraction further reduced charging time. The optimal combination of Cu MF, Cu nanoparticles, and MF design reduced melting time by three times, with a 12.8% and 21.96% reduction in charging time for MF zone configurations. Chibani et al. investigated the melting process of PCM embedded with nanoparticles and MF in a shell-and-tube LHTES, using numerical simulations **[20]**.

The model was first validated with experimental data. The effects of adding 5% Al_2O_3 nanoparticles and using various MFs (Al, Cu, Nickel, Titanium) with ε ranging from 0.96 to 0.99 were compared regarding temperature and liquid fraction during melting. The MF-PCM systems outperformed pure and nano-enhanced PCM, significantly reducing melting time. The effectiveness of the MFs followed the thermal conductivity order: Cu>Al>Ni>Ti. Increasing ε reduced melting time, with the highest porosity (ε=0.99) yielding the best performance. This study optimizes the design for improved practical application and reduced energy waste.

When the literature is examined, many methods and configurations have been used and examined to increase the thermal conductivity of PCM used for heat storage. However, due to these examinations, melting performance and natural convection characteristics of a LHTES including MF manufactured from two different materials with different physical property variables according to the heat source have not been examined in detail. In this study, one-half of a rectangular LHTES volume was filled with Al MF and Cu MF with ε=0.9 and 20. The entire volume of the rectangular LHTES was filled with RT-58 PCM material and heated from a single wall. In the numerical analyses where the MF in contact with the hot wall was also variable, a total of 6 different configurations were analysed.

2. DESCRIPTION OF MODEL AND MATHEMATICAL BACKGROUND

A schematic view of rectangular LHTESs is presented in Figure 1. Entire geometric, morphologic, and boundary conditions are similar to each system. A rectangular cavity was formed considering 30 cm height and 10 cm width. 350K has been applied to the left wall of the cavity, and the other wall is considered adiabatic. Moreover, the no-slip condition was applied to all walls. Also, the geometry was divided into two equal parts, and half volumes were filled with Al and Cu MFs, which changed the arrangement based on the thermal wall. MF parameters ε and ω were selected as 0.9 and 20 PPI, respectively, after the detailed investigation of the literature based on the Refs **[21-23]**. Variants of these structural parameters, as well as the arrangement of MFs, were used. Because of this, six different cases including the parameters in Table 1 have been analysed.

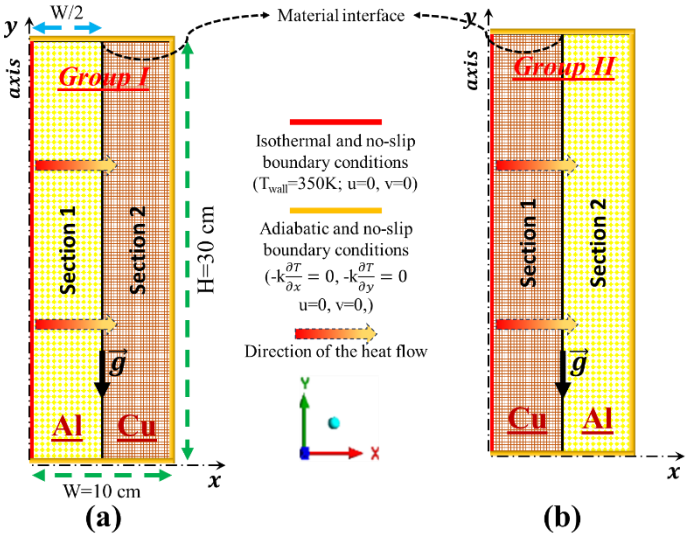

Figure 1. Schematic view of the computational domains for; (a) Group I (Al contacts hot wall) and (b) Group II (Cu contacts hot wall).

Table 1. Physical configuration of computational domains

Group I						
Case No	Section 1			Section 2		
	Material	ε	ω	Material	ε	ω
RC1	Al	0.9	20	Cu	0.9	20
RC2	Al	0.95	20	Cu	0.9	20
RC3	Al	0.95	20	Cu	0.95	20
Group II						
Case No	Section 1			Section 2		
	Material	ε	ω	Material	ε	ω
RC4	Cu	0.9	20	Al	0.9	20
RC5	Cu	0.95	20	Al	0.9	20
RC6	Cu	0.95	20	Al	0.95	20

The mentioned above cases have been solved based on the FVM combined with EPM **[24]**. The Brinkman-Forchheimer extended Darcy model **[25]**, and the local thermal equilibrium (LTE) hypothesis was used to characterize the MF in the analyses **[26]**. The continuity, momentum, and energy (for LTE) governing equations used in melting process solving are given in Eq. 1-3 **[27]**, respectively. While applying these equations, some assumptions are given below, taking into account.

- The analysis is carried out for a two-dimensional axisymmetric geometry.
- Due to the low-temperature difference between the solidus and liquidus temperature of PCM, the Boussinesq approximation has been used for calculating the density **[28]**.
- Thermophysical properties of PCM and MFs are considered constant.
- In the energy equation, the effect of viscosity is neglected.
- Computational domain volume is not changed during the melting process.
- Structural modification of MFs is accepted as isotropic and homogeneous.

$$\nabla \cdot V = 0 \tag{1}$$

where, V [m.s^{-1}] shows the PCM velocity in the rectangular cavity.

$$\frac{\rho_p}{\varepsilon}\frac{\partial V}{\partial t} + \frac{\rho_p}{\varepsilon^2}V\cdot\nabla V = -\nabla p + \frac{\mu_p}{\varepsilon}\nabla^2 V - \frac{(1-\beta)^2}{(\beta^3+0.001)}A_{mush}V - \left(\frac{\mu_p}{K}V + \frac{C_F}{\sqrt{K}}\rho_p V|V|\right) + \rho_p g \gamma \Delta T_0 \tag{2}$$

in which, g [m.s^{-2}], ρ [kg.m^{-3}], p [Pa], T [K], A_{mush} [kg.m^{-3}.s^{-1}], K [m^2], and C_F [m^{-1}] symbolize the gravity (g=9.91 [m.s^{-2}]), density, pressure, temperature, mush zone constant (set to 10^5 kg.m^{-3}.s^{-1}), permeability, and Forchheimer's drag coefficient (inertial).

$$(\rho c_p)_{eff}\left(\frac{\partial T}{\partial t} + V\cdot\nabla T\right) = k_{eff}\nabla^2 T - \varepsilon\rho_p H_L\frac{\partial \beta}{\partial t} \tag{3}$$

where, c_p [J.kg^{-1}.K^{-1}], k [W.m^{-1}.K^{-1}], and H_L [kJ.kg^{-1}] describe the specific heat, thermal conductivity, and latent heat energy. Incorporating MF enhances the thermal conductivity of the process named effective and this property is calculated with Eq. (4) **[29]**.

$$k_{eff} = \varepsilon k_{PCM} + (1-\varepsilon)k_{MF} \tag{4}$$

Other characteristic properties calculated based on the given structural properties with ε=0.9 and ω=20 PPI for both MFs are presented in Table 2. Besides, the thermo-physical properties of RT-58 (Rubitherm) PCM, Al MF, and Cu MF have been presented in Table 3.

Table 2. Equations used to calculate MF structural properties **[30]**

Definition	Equation	Eq.
Permeability, [m^2]	$K = \frac{\varepsilon^2 d_k^2}{36(\delta^2-\delta)}$	(5)
Characteristic length, [m]	$d_k = \frac{\delta}{3-\delta}d_p$	(6)
Tortuosity coefficient	$\delta = 2 + 2\cos\left[\frac{4\pi}{3} + \frac{1}{3}\cos^{-1}(2\varepsilon-1)\right]$	(7)
Forchheimer's drag (inertial) coefficient, [1/m]	$C_F = 0.00212(1-\varepsilon)^{-0.132}\left(\frac{d_f}{d_p}\right)^{-1.63}$	(8)
Fiber diameter, [m]	$d_f = 1.18\sqrt{\frac{1-\varepsilon}{3\pi}}\left(\frac{1}{1-e^{\left(-\frac{1-\varepsilon}{0.04}\right)}}\right)$	(9)
Pore diameter, [m]	$d_p = \frac{0.0254}{\omega}$	(10)

Table 3. Thermophysical properties of RT58, Al MF, and Cu MF.

Properties	RT58 **[31]**	Al **[32]**	Cu **[33]**
Density, ρ [kg.m^{-3}]	825	2719	8900
Specific heat, c_p [J.kg^{-1}.K^{-1}]	2000	871	385
Thermal conductivity, k [W.m^{-1}.K^{-1}]	0.2	202.4	401
Dynamic viscosity, μ [kg.m^{-1}.s^{-1}]	0.0269	-	-
Thermal expansion coefficient, γ [K^{-1}]	0.00011	-	-
Latent heat, H_L [J.kg^{-1}]	160000	-	-
Solidus temperature, T_S [K]	326	-	-
Liquidus temperature, T_L [K]	332	-	-

The EPM is applicable for scenarios where melting occurs progressively across a finite temperature range without a well-defined melting front. This method defines three distinct phases during the melting process: a solid phase where β=0, a mixed solid-liquid phase (mushy) where 0<β<1, and a liquid phase where β=1. The value of β depends on the local temperature and is determined using Eq. (11).

$$\beta = \frac{\Delta H}{H_L} = \begin{cases} 0 \text{ if } < T_S \\ \frac{T - T_S}{T_L - T_S} \quad \text{if } T_S < T < T_L \\ 1 \text{ if } T > T_L \end{cases} \tag{11}$$

where, T_S [K], T [K], and T_L [K] represent the temperatures of the solid phase, the local region, and the liquid phase, respectively. The region with a temperature below T_S is entirely solid, whereas the area with a temperature above T_L is fully liquid. Melting occurs when the temperature is within the range between T_S and T_L. In all cases, the initial temperature (T_{in}) is 298.15 K.

The governing equations were solved using ANSYS FLUENT 2024 R1 software considering the boundary and initial conditions of the computational domains and a time-dependent FVM analysis was carried out. To provide a sustainability pressure field, the SIMPLE algorithm was selected, and PRESTO! scheme was employed for pressure calculations. Besides, the second-order upwind scheme method was preferred to calculate the momentum and energy equations while residual trends were set to 10^{-6}.

After determining the physical properties and mathematical background, mesh convergence and time step size sensitivity analyses required for time-dependent numerical analyses should be performed to provide highly reliable results. In this context, the mesh convergence analysis of the rectangular LHTES in question was conducted for mesh numbers 3465, 7500, and 13333, and the time step sensitivity analysis was conducted for t=0.1, 0.5, and 1.0s, and the obtained liquid fraction-time graphs are presented in Figure 2(a) and Figure 2(b), respectively. When investigating the trends, it can be said that mesh number and time step size did not affect the results. According to the numerical results, the average deviation of 0.51% and 0.74% are calculated between 3465-13333 and 7500-13333, respectively, considering the mesh number at *t*=0.5s. On the other side, 0.71% and 0.83% average deviations were detected between *t*=0.1-0.5s and *t*=0.1-1.0s for time step size sensitivity analysis, respectively, at 7500 mesh number. Based on these results, a mesh number of 7500 and a time step size of *t*=0.5s have been selected to solve further solutions. On the other hand, the mesh structure of the computational domain is given in Figure 3.

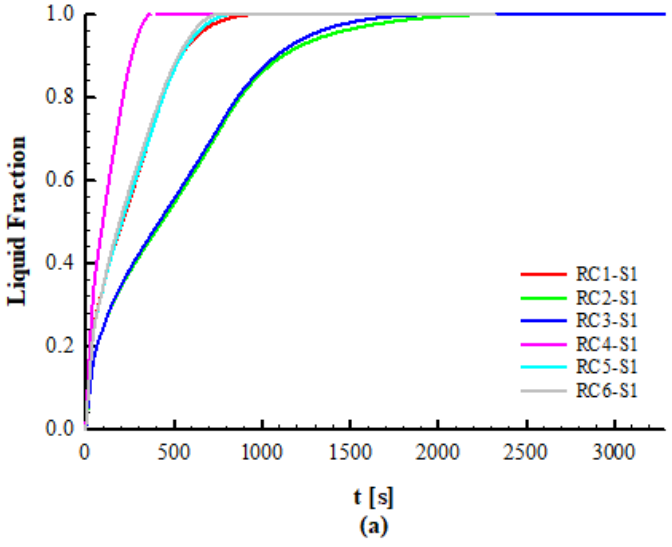

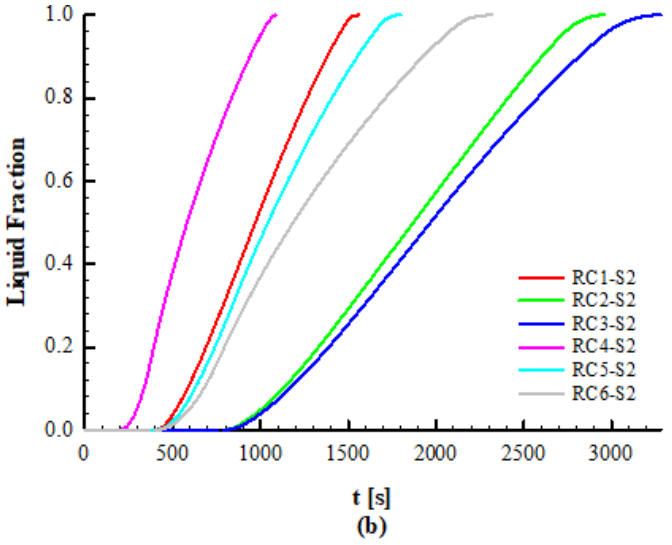

Figure 2. Imperative analyses before major solutions; (a) mesh convergence analysis at t=0.5s and (b) time step size sensitivity analysis at 7500 mesh number.

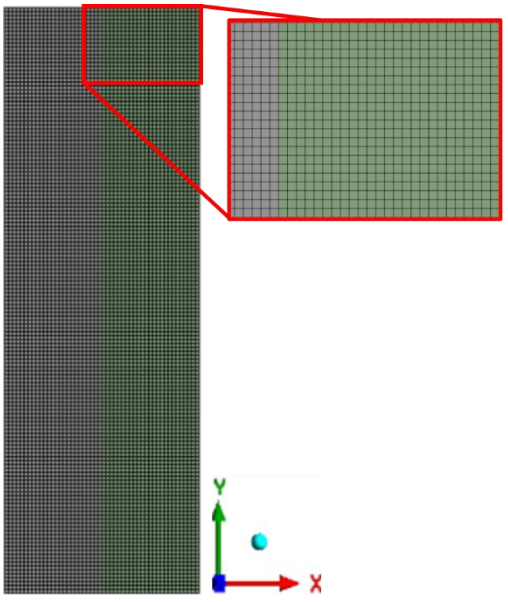

Figure 3. The mesh structure belongs to the 7500 mesh number.

Before proceeding to the analyses where the final results will be obtained, the solution methods and mesh structure of the numerical analysis, that is, the entire analysis setup, must be validated. In this context, the necessary validation is compared with the liquid fraction function of the study conducted by Huang et al. both as a contour and graphically in Table 4 and Figure 4, respectively **[30]**. When the contours are examined, it is concluded that the liquid-solid interface has almost the same distribution at all t times. When the numerical values in the trends are examined, it is calculated that the average deviation value between the two trends is 0.81%. With these results, it can be concluded that all solution procedures and applications applied in the study provide results compatible with the literature.

Table 4. Validation of the results as a liquid fraction contour.

t [s]	60	180	360	540	720	900
Huang et al. **[30]**	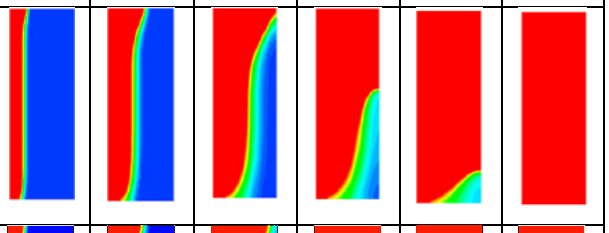					
Present study	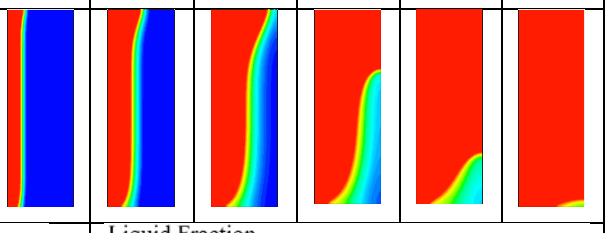					

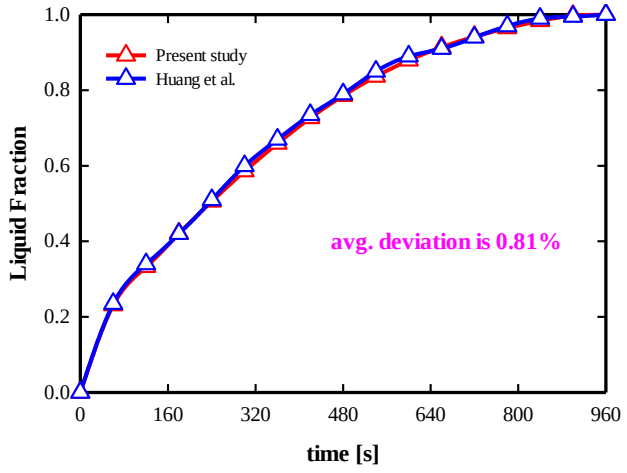

Figure 4. Validation of the results with Huang et al. study as a liquid fraction trend **[30]**

3. RESULTS AND DISCUSSION

The liquid fraction performance of the cases is examined in Figure 5. When Figure 5(a) showing the S1 characteristic is examined, the RC4, RC5, and RC6 cases, where the hot wall is in contact with the Cu MF, give the fastest response to the heating effect. The main reason for this situation is the increase in effective thermal conductivity in the cases due to the higher thermal conductivity of Cu MF. According to the results, RC4 reached full melting at the earliest time (t=1120 s). At t=1120 s, the melting rates of PCM in RC1, RC2, RC3, RC5 and RC6 are controlled at 82.9%, 49.9%, 49.7%, 78.5% and 72.8%, respectively. It can also be understood that the porosity of Cu MF, ε=0.95, exhibits a similar characteristic with the ε =0.9 of Al MF, which is close to the wall. From this result, it is undeniable that in addition to considering how high the thermal conductivity of the MF material used is, its porosity should also be taken into account. In S2, the fastest performance was again shown by RC4 in Figure 5(b), although Al MF was. The factor that caused this situation is that Cu MF, positioned on the hot wall with a low porosity, can conduct heat at a good level and Al MF with ε=0.9 can also respond quickly to this performance. However, as the porosity of Cu MF in S1 increases, RC4 shifted to another characteristic mechanism mentioned above and the second fastest performance in S2 was realized in RC1. This is the decrease in the level of heat conduction due to the decreasing amount of conductive material per unit volume as the porosity increases. A similar result has been found by Ami Ahmadi et al. **[10]**. Since the low porosity value contains more MF with high conductivity in volume, in these cases the heat transfer mechanism in the system is mostly carried out by conduction. In cases consisting of high porosity MF, an environment is created in the system where the PCM can move more easily and natural convection increases. However, thermal resistance also tends to increase at this point.

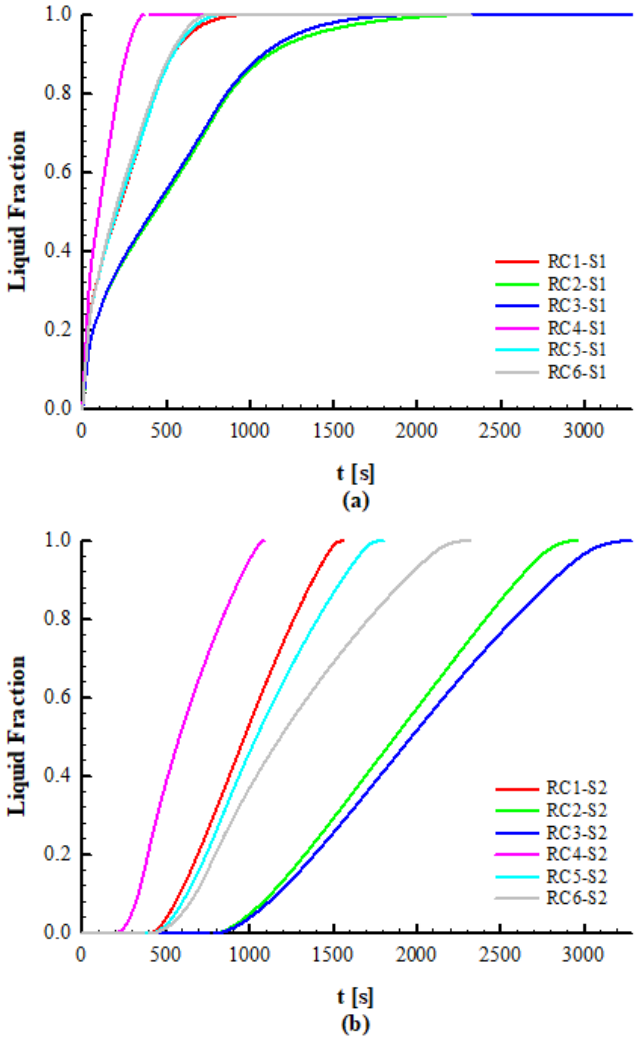

Figure 5. Liquid fraction characteristics in; (a) S 1 and (b) S2 as a function of time.

The liquid fraction behaviour of the cases is presented as contour in Table 5. Along with these contours, solid-liquid interfaces can be seen and the heat transfer progress in LHTES can be understood. When the figures are examined, it is observed that the solid-liquid interface in RC4 progresses faster and melts earlier. In this melting process, it is seen that the solid-liquid interface, which is in contact with the lower and upper points of the rectangular cavity, is in the form of a vertical line throughout the melting process. The main factor causing this situation is that the porosity of the MFs placed in the sections in RC4 is ε= 0.9. This parameter occupies more volumetrically the conductive material forming the MF and does not allow natural convection, and the heat transfer from the hot wall occurs by conduction throughout the process.

On the other hand, the thermal conductivity of the material from which the MF is manufactured is as important as the porosity of the MF. Although there is Cu MF with a porosity of ε= 0.95 in S1 of RC5 and RC6, no considerable tendency towards natural convection is observed here. However, when the heat reached S2, which consists of Al MF, the solid-liquid interface showed a logarithmic trend in the upper region of the rectangular cavity due to the decrease in the density of the PCM melted in the lower region of the rectangular cavity and the effect of the buoyancy force. The reason for this situation is that the porosity of S1 in RC5 is ε=0.95 and therefore the PCM finds more space to move in the cavity. In RC6, the porosity is ε=0.95 for both Sections and it is observed that the solid-liquid interface becomes more pronounced.

From these results, it can be determined by the behavior of the solid-liquid interface that the parameters of the MF material and porosity in the rectangular cavity directly affect the complete melting process of LHTES.

Figure 6 depicts the final melting time of the sections. According to the results, RC4 reaches the fully melted state first because in this case, the MF near the hot wall is Cu MF with high thermal conductivity and the porosity in both sections is ε=0.90. The combination of these two phenomena makes RC4 the fastest fully melted state. On the other hand, the case that provides the second fastest melting performance is RC1. Although Al MF is placed in the section close to the hot wall, the porosity being ε=0.9 in all sections made RC1 melt faster than the other cases. From these results, it can be inferred that the porosity is more important than the material type of the MF integrated into the system. The complete melting time in the S1 and S2 regions of RC4 was 2.5 and 1.4 times faster than that of RC1, respectively.

Table 5. Comparison of liquid fraction contours of the cases as a function of the time

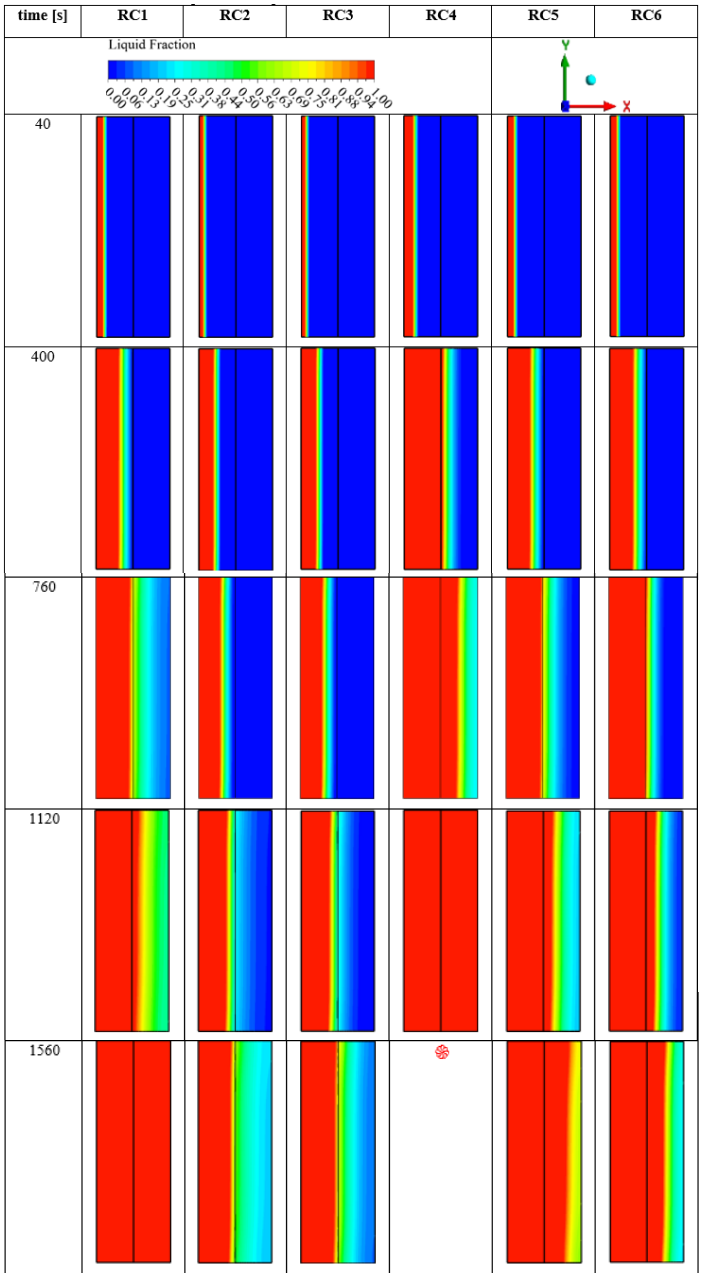

Figure 6 depicts the final melting time of the sections. According to the results, RC4 reaches the fully melted state first because in this case, the MF near the hot wall is Cu MF with high thermal conductivity and the porosity in both sections is ε=0.90. The combination of these two phenomena makes RC4 the fastest fully melted state. On the other hand, the case that provides the second fastest melting performance is RC1. Although Al MF is placed in the section close to the hot wall, the porosity being ε=0.9 in all sections made RC1 melt faster than the other cases. From these results, it can be inferred that the porosity is more important than the material type of the MF integrated into the system. The complete melting time in the S1 and S2 regions of RC4 was 2.5 and 1.4 times faster than that of RC1, respectively.

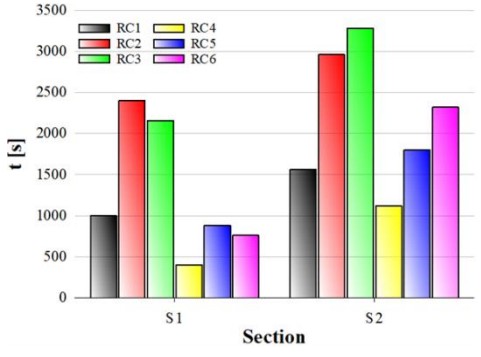

Figure 6. Full melting time performance of the cases

To evaluate the effectiveness of heat transfer throughout the melting process, the time-dependent Nusselt number (Nu) variation is given in Figure 7. At the onset of melting, Nu shows a sudden increase due to heat transfer predominantly realized by conduction.

The results show that placement and porosity of MFs important for the progress of the heat and the cases of Cu MF near the hot wall performed the highest Nu compared to identical configurations. The average Nu of RC4, RC5, and RC6 is 34.4%, 59.6%, and 35.5% higher than that of RC1, RC2, and RC3, respectively. On the other hand, increasing porosity also negatively affects the heat progression in the LHTES, and the change in S1 affects this progression more than the change in S2. This can be obtained by comparing the changes in average Nu between RC4-RC5 and RC5-RC6. RC4 with a porosity of ε=0.90 in S1 transfers 48.4% more heat than RC5 with a porosity of ε=0.95, and RC5 with a porosity of ε=0.90 in S2 transfers 23.3% more heat than RC6 with a porosity of ε=0.95.

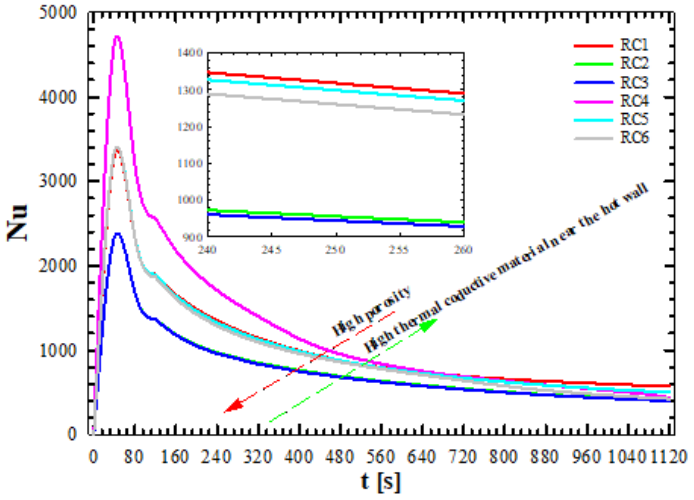

Figure 7. Effect of MF material and porosity configuration on time-dependent Nu

Table 6 illustrates the natural convection flow pattern in the cases up to t=1120 s. Velocity vectors reveal the flow characteristics arising from natural convection and directly affect the convective heat transfer effectiveness. At the beginning of the melting process, in all configurations, the flow field remained quite weak and the velocity magnitudes remained at low levels. This situation shows that PCM substantially remained in a solid form and natural convection did not enhance. As the melting progresses over time, increases in the natural convection intensity were observed due to temperature differences occurring in the liquid phase.

Compared to liquid fraction variation in Table 5, velocity vectors remain limited beyond the melted region, and high-velocity magnitudes were shown as the boundaries. A stationary area was formed in the central region of the cavity by the formation of a typical natural convection cycle (from left to right) characterized by the upward movement of the hot liquid and the downward movement of the cold liquid. These high velocities disappear with the complete melting of the PCM, and it is obvious that the changes in the velocity vectors between the cases are directly shaped according to the alignment and thermal conductivity of the MF.

Table 6. Comparison of velocity vectors of the cases as a function of the time

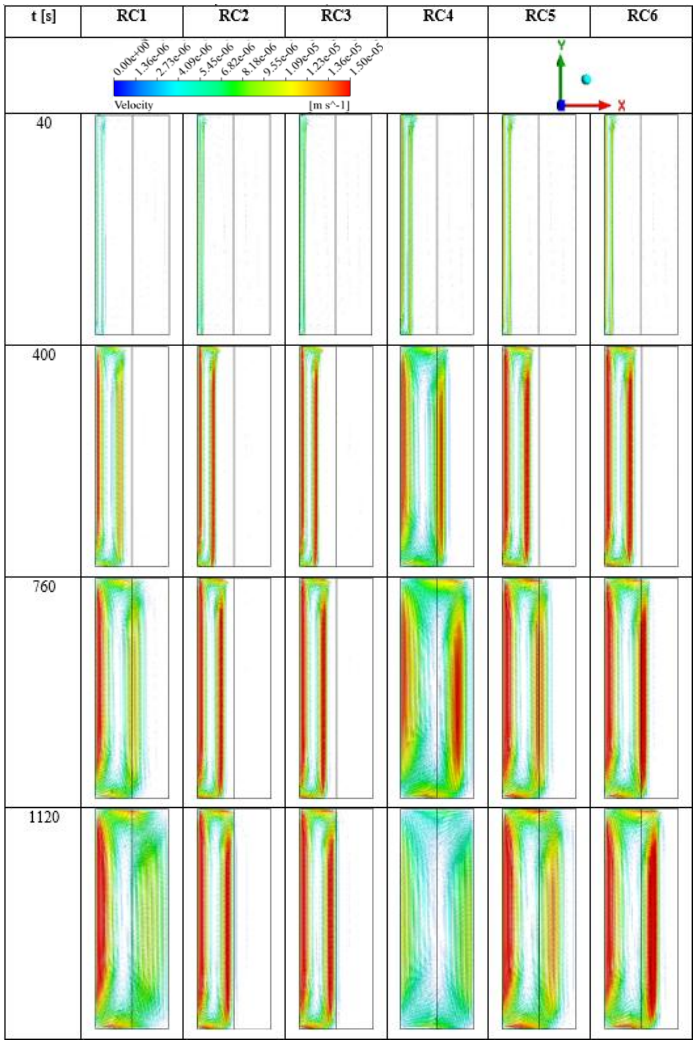

4. CONCLUSION

This paper includes the investigation of different MF types and configurations on melting dynamics and flow characteristics of rectangular LHTES. In the study, a 2D numerical model was developed and six different case configurations were solved based on EPM and the Brinkman-Forchheimer extended Darcy model. Dynamic responses of melting performance and natural convection characteristics have been presented and compared with each other. According to this purpose, the major findings are listed as follows:

1) Cu MF, where placed in S1, quickly responded to the heating effect due to it having higher thermal conductivity.

2) The RC4 case performed the highest melting process because the solid-liquid interface progressed faster.

3) In the RC4 case, the solid-liquid interface contacted with the lower and upper points of the rectangular cavity shows vertical progress. The main reason for this situation is related to low porosity in both sections, and Cu MF is the material conducting the heat into the further section.

4) When S1 was filled with Cu MF with ε=0.95 and S2 with Al MF, the solid-liquid interface showed a logarithmic trend in the upper region of the rectangular cavity; this is due to the decrease in the density of molten PCM in the lower region of the rectangular cavity and the effect of buoyancy force.

5) The second faster melting performance has been observed in RC1. This result shows that porosity is more important than the material type of the MF and that the full melting time in the S1 and S2 regions of RC4 was 2.5 and 1.4 times faster than that of RC1, respectively.

6) The placement of MF with higher thermal conductivity on the hot wall and lower porosity contributed to the improvement of heat transfer in LHTES. RC4 has a 34.4% higher Nu performance than RC1 and 48.4% higher Nu performance than RC5.

7) A stationary region was formed in the center of the cavity due to melted PCM moving upward from the hot wall to the cold section due to buoyancy force as melting progresses. Besides, the velocity in the LHTES significantly relies on the alignment and thermal conductivity of the MF.

5. FUTURE PERSPECTIVE

In future studies, the effects of different types of MF materials, porosity levels, and geometric arrangements with PCMs on heat transfer can be investigated more comprehensively. In addition, the effects of composite structures formed by adding nanoparticles to MF on thermal performance can be investigated, and hybrid improvement methods can be evaluated. In addition, magnetohydrodynamic studies can be conducted if the nanoparticles are magnetic. Experimental verification studies conducted under variable thermal boundary conditions reflecting real operating conditions will increase the validity of the numerical results obtained. In this context, application-based research supported by energy and exergy analyses will make significant contributions to the design of more efficient and sustainable thermal energy storage systems.

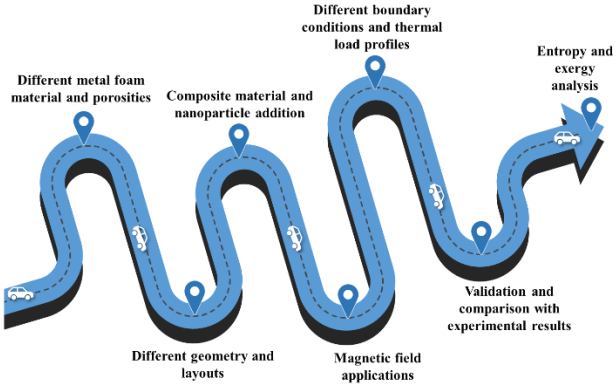

Figure 8. Schematic illustration of the proposed roadmap for future studies focusing on the enhancement of thermal performance in LHTES systems using metal foam-PCM composites.

Nomenclature

A_{mush}	mush zone constant, [$kg.m^{-3}.s^{-1}$]	T	temperature [K]
c_p	specific heat, [$J.kg^{-1}.K^{-1}$]	TES	thermal energy storage
C_F	Forchheimer' s drag (inertial) coefficient, [m^{-1}]	V	velocity [$m.s^{-1}$]
d_f	fiber diameter, [m]	Greek symbols	
d_k	characteristic length, [m]	β	liquid fraction
d_p	pore diameter, [m]	ω	pore density, [PPI]
EPM	enthalpy-porosity method	ε	porosity
FVM	finite volume method	ρ	density, [$kg.m^{-3}$]
g	gravity, [$m.s^{-2}$]	δ	tortuosity coefficient
H_L	latent heat, [$J.kg^{-1}$]	∀	unit volume [m^3]
k	thermal conductivity, [$W.m^{-1}.K^{-1}$]	μ	dynamic viscosity, [$kg.m^{-1}.s^{-1}$]
K	permeability [m^2]	γ	thermal expansion coefficient, [K^{-1}]
LHTES	latent heat thermal energy storage	Subscripts	
MF	metal foam	in	initial
p	pressure, [Pa]	L	liquidus
PCM	phase change material	S	solidus
S	section		

REFERENCES

[1] A. Rahman, O. Farrok, and M. M. Haque, "Environmental impact of renewable energy source based electrical power plants: Solar, wind, hydroelectric, biomass, geothermal, tidal, ocean, and osmotic," *Renewable and Sustainable Energy Reviews*, vol. 161, Art. no. 112279, 2022, doi: 10.1016/j.rser.2022.112279.

[2] A. Razmjoo, L. G. Kaigutha, M. A. Vaziri Rad, M. Marzband, A. Davarpanah, and M. Denai, "A technical analysis investigating energy sustainability utilizing reliable renewable energy sources to reduce CO_2 emissions in a high-potential area," *Renewable Energy*, vol. 164, pp. 46–57, 2021, doi: 10.1016/j.renene.2020.09.042.

[3] G. Sadeghi, "Energy storage on demand: Thermal energy storage development, materials, design, and integration challenges," *Energy Storage Materials*, vol. 46, pp. 192–222, 2022, doi: 10.1016/j.ensm.2022.01.017.

[4] J. Mitali, S. Dhinakaran, and A. A. Mohamad, "Energy storage systems: a review," *Energy Storage and Saving*, vol. 1, no. 3, pp. 166–216, 2022, doi: 10.1016/j.enss.2022.07.002.

[5] I. Sarbu and C. Sebarchievici, "A comprehensive review of thermal energy storage," *Sustainability*, vol. 10, no. 1, Art. no. 191, 2018, doi: 10.3390/su10010191.

[6] S. Khare, M. Dell'Amico, C. Knight, and S. McGarry, "Selection of materials for high temperature latent heat energy storage," *Solar Energy Materials and Solar Cells*, vol. 107, pp. 20–27, 2012, doi: 10.1016/j.solmat.2012.07.020.

[7] N. Nallusamy, S. Sampath, and R. Velraj, "Experimental investigation on a combined sensible and latent heat storage system integrated with constant/varying (solar) heat sources," *Renew. Energy*, vol. 32, no. 7, pp. 1206–1227, 2007, doi: 10.1016/j.renene.2006.04.015.

[8] N. Alipour, B. Jafari, and K. Hosseinzadeh, "Analysis of the impact of metal foam with phase change material on solar photovoltaic thermal system efficiency," *Journal of Energy Storage*, vol. 98, Art. no. 113064, 2024, doi: 10.1016/j.est.2024.113064.

[9] H. Li, C. Hu, Y. He, D. Tang, K. Wang, and X. Hu, "Visualized-experimental investigation on the energy storage performance of PCM infiltrated in metal foam with varying pore densities," *Energy*, vol. 237, Art. no. 121540, 2021, doi: 10.1016/j.energy.2021.121540.

[10] H. A. Ahmadi, N. Variji, A. Kaabinejadian, M. Moghimi, and M. Siavashi, "Optimal design and sensitivity analysis of energy storage for concentrated solar power plants using phase change material by gradient metal foams," *Journal of Energy Storage*, vol. 35, Art. no. 102233, 2021, doi: 10.1016/j.est.2021.102233.

[11] N. Prasanth, M. Sharma, R. N. Yadav, and P. Jain, "Designing of latent heat thermal energy storage systems using metal porous structures for storing solar energy," *Journal of Energy Storage*, vol. 32, Art. no. 101990, 2020, doi: 10.1016/j.est.2020.101990.

[12] A. Parida, A. Bhattacharya, and P. Rath, "Effect of convection on melting characteristics of phase change material-metal foam composite thermal energy storage system," *Journal of Energy Storage*, vol. 32, Art. no. 101804, 2020, doi: 10.1016/j.est.2020.101804.

[13] C. Nie, J. Liu, and S. Deng, "Effect of geometry modification on the thermal response of composite metal foam/phase change material for thermal energy storage," *International Journal of Heat and Mass Transfer*, vol. 165, Art. no. 120652, 2021, doi: 10.1016/j.ijheatmasstransfer.2020.120652.

[14] A. R. Karimi, M. Siavashi, M. Tahmasbi, and A. M. Norouzi, "Experimental analysis to improve charge/discharge of thermal energy storage in phase change materials using helical coil and porous metal foam," *Journal of Energy Storage*, vol. 55, Art. no. 105759, 2022, doi: 10.1016/j.est.2022.105759.

[15] M. Ghalambaz, M. Fteiti, O. Younis, M. Sheremet, and H. A. Hasan, "An improved latent heat thermal energy storage using two layers of metal foams," *Appl. Therm. Eng.*, vol. 234, p. 121319, 2023, doi: 10.1016/j.applthermaleng.2023.121319.

[16] S. Liu, H. Wang, Q. Ying, and L. Guo, "Numerical study on the combined application of multiple phase change materials and gradient metal foam in thermal energy storage device," *Appl. Therm. Eng.*, vol. 257, p. 124267, 2024, doi: 10.1016/j.applthermaleng.2024.124267.

[17] V. Joshi and M. K. Rathod, "Experimental and numerical assessments of thermal transport in fins and metal foam infused latent heat thermal energy storage systems: A comparative evaluation," *Appl. Therm. Eng.*, vol. 178, p. 115518, 2020, doi: 10.1016/j.applthermaleng.2020.115518.

[18] Z. Haddad, F. Iachachene, M. A. Sheremet, and E. Abu-Nada, "Numerical investigation and optimization of melting performance for thermal energy storage system partially filled with metal foam layer: New design configurations," *Appl. Therm. Eng.*, vol. 223, p. 119809, 2023, doi: 10.1016/j.applthermaleng.2022.119809.

[19] S. A. M. Mehryan, K. A. Ayoubloo, M. Mahdavi, O. Younis, Z. Kazemi, M. Ghodrat, and M. Ghalambaz, "Optimum configuration of a metal foam layer for a fast thermal charging energy storage unit: A numerical study," *J. Energy Storage*, vol. 48, p. 103950, 2022, doi: 10.1016/j.est.2021.103950.

[20] A. Chibani, S. Merouani, and F. Benmoussa, "Computational analysis of the melting process of phase change material–metal foam-based latent thermal energy storage unit: The heat exchanger configuration," *J. Energy Storage*, vol. 42, p. 103071, 2021, doi: 10.1016/j.est.2021.103071.

[21] R. M. K. Ali and S. Lafta Ghashim, "Numerical analysis of the heat transfer enhancement by using metal foam," *Case Stud. Therm. Eng.*, vol. 49, p. 103336, 2023, doi: 10.1016/j.csite.2023.103336.

[22] A. Arshad, M. Jabbal, H. Faraji, P. Talebizadehsardari, M. A. Bashir, and Y. Yan, "Thermal performance of a phase change material-based heat sink in presence of nanoparticles and metal-foam to enhance cooling performance of electronics," *J. Energy Storage*, vol. 48, p. 103882, 2022, doi: 10.1016/j.est.2021.103882.

[23] M. Valizade, M. M. Heyhat, and M. Maerefat, "Experimental study of the thermal behavior of direct absorption parabolic trough collector by applying copper metal foam as volumetric solar absorption," *Renew. Energy*, vol. 145, pp. 261–269, 2020, doi: 10.1016/j.renene.2019.05.112.

[24] A. D. Brent, V. R. Voller, and K. J. Reid, "Enthalpy-porosity technique for modeling convection-diffusion phase change: Application to the melting of a pure metal," *Numer. Heat Transf.*, vol. 13, no. 3, pp. 297–318, 1988, doi: 10.1080/10407788808913615.

[25] K. Vafai and S. J. Kim, "On the limitations of the Brinkman–Forchheimer-extended Darcy equation," *Int. J. Heat Fluid Flow*, vol. 16, no. 1, pp. 11–15, 1995, doi: 10.1016/0142-727X(94)00002-T.

[26] S. Pati, A. Borah, M. P. Boruah, and P. R. Randive, "Critical review on local thermal equilibrium and local thermal non-equilibrium approaches for the analysis of forced convective flow through porous media," *Int. Commun. Heat Mass Transf.*, vol. 132, p. 105889, 2022, doi: 10.1016/j.icheatmasstransfer.2022.105889.

[27] Q. Ying, H. Wang, and E. Lichtfouse, "Numerical simulation on thermal behavior of partially filled metal foam composite phase change materials," *Appl. Therm. Eng.*, vol. 229, p. 120573, 2023, doi: 10.1016/j.applthermaleng.2023.120573.

[28] T. Bouzennada, A. Abderrahmane, O. Younis, M. Oreijah, K. Guedri, C. Maatki, and L. Kolsi, "Numerical simulation of heat transfer and melting process in a NEPCM: Using new fin shape," *Int. Commun. Heat Mass Transf.*, vol. 143, p. 106711, 2023, doi: 10.1016/J.ICHEATMASSTRANSFER.2023.106711.

[29] ANSYS Inc., *ANSYS FLUENT Theory Guide*, Canonsburg, PA, USA: ANSYS Inc., 2011, p. 794.

[30] S. Huang, J. Lu, and Y. Li, "Numerical study on the influence of inclination angle on the melting behaviour of metal foam-PCM latent heat storage units," *Energy*, vol. 239, p. 122489, 2022, doi: 10.101/10.1016/J.ENERGY.2021.122489.

[31] N. S. Dhaidan and A. F. Khalaf, "Experimental evaluation of the melting behaviours of paraffin within a hemicylindrical storage cell," *Int. Commun. Heat Mass Transf.*, vol. 111, p. 104476, 2020, doi: 10.1016/j.icheatmasstransfer.2020.104476.

[32] C. Ji, Z. Qin, S. Dubey, F. H. Choo, and F. Duan, "Simulation on PCM melting enhancement with double-fin length arrangements in a rectangular enclosure induced by natural convection," *Int. J. Heat Mass Transf.*, vol. 127, pp. 255–265, 2018, doi: 10.1016/j.ijheatmasstransfer.2018.07.118.

[33] N. S. Bondareva and M. A. Sheremet, "Numerical simulation of heat transfer performance in an enclosure filled with a metal foam and nano-enhanced phase change material," *Energy*, vol. 296, p. 131123, 2024, doi: 10.1016/j.energy.2024.131123.

International Journal of Energy Horizon 01 (2025) 20-25

International Journal of Energy Horizon

journal homepage: https://dergipark.org.tr/tr/pub/ijeh

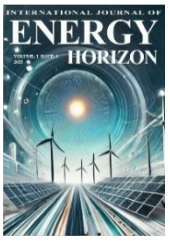

Research Paper

Electrolyzer Systems as Hydrogen Refueling Stations: A Review of Capex, Opex, and LCOH Calculations

Emre YILDIRIM[1,*], Yağmur BUDAK[2]

[1,2] Ankara Yildirim Beyazit University, Faculty of Engineering and Natural Sciences, Mechanical Engineering, Ankara, 06010, Türkiye

[1]ORCID No: 0000-0001-5792-4800
[2]ORCID No: 0000-0002-8443-1160

ARTICLE INFO

Article History:

Received:28 May 2025
Revised:20 June 2025
Accepted:24 June 2025
Available online: 30 June 2025

Keywords:

Hydrogen energy
Refueling station
LCOH

ABSTRACT

In order to lower transportation-related carbon emissions and promote the use of hydrogen-powered cars, this article offers an economic analysis hydrogen refueling station (HRS) that is connected to photovoltaic (PV) system. In the study, the HRS system with alkaline and PEM electrolyzers with a nominal hydrogen production rate of 30 $Nm^3.h^{-1}$ was compared. While the alkaline HRS system required 192.5 kW PV installed power, the PEM HRS system required 214.5 kW PV installed power. In order to evaluate the HRS system, the levelized cost of hydrogen (LCOH) was calculated by taking into account the initial investment costs, operating expenditures and the amount of hydrogen produced. Economic analysis of a PV integrated system for an inactive HRS in Ankara was conducted. Based on a daily hydrogen production capacity of 65 kg for both electrolyzers with identical nominal outputs, the results of the techno-economic analysis over a 10-year operational period indicate that the levelized cost of hydrogen (LCOH) is calculated as 6.39 $\$.kg^{-1}$ H_2 for the alkaline electrolyzer and 7.73 $\$.kg^{-1}$ H_2 for the PEM electrolyzer, respectively. This study helps to build sustainable energy infrastructure including PV integrated HRS design, calculation and economic evaluation. The findings give academics, industry stakeholders, and policymakers important information to support energy sustainability and the goal of a carbon-neutral transportation sector.

1. INTRODUCTION

In the global effort to mitigate climate change and reduce greenhouse gas emissions, hydrogen has emerged as a promising clean energy carrier. Its high mass-specific energy content (120 $MJ \cdot kg^{-1}$) and low environmental impact make it a suitable alternative to fossil fuel-based energy systems **[1]**. When produced from renewable sources such as solar or wind energy, hydrogen can support a wide range of applications, including energy storage, industrial processes, and zero-emission transportation systems.

Hydrogen has the unique ability to store surplus renewable electricity through water electrolysis, enabling energy balancing across different sectors. The stored hydrogen can later be reconverted into electricity via fuel cells or used directly to fuel buildings or vehicles. Among these applications, fuel cell electric vehicles (FCEVs) have garnered growing attention due to their high efficiency and zero emissions - with water being the only byproduct**[2].** However, the widespread adoption of FCEVs is contingent upon the development of reliable hydrogen infrastructure, particularly hydrogen refueling stations (HRS), which serve as the cornerstone of hydrogen-powered transportation systems **[3]**

HRS are crucial for the commercial viability of FCEVs, as they ensure reliable access to hydrogen fuel. Despite the increasing deployment of FCEVs in recent years, the lack of accessible and economically viable refueling infrastructure remains a significant bottleneck **[4]**. To overcome this challenge, the integration of renewable energy sources, especially solar photovoltaic (PV) systems-with on-site hydrogen production at HRS has been proposed as an environmentally and economically favorable solution. Water electrolysis powered by renewable electricity is considered one of the most sustainable hydrogen production pathways, promoting energy sector decarbonization and cross-sector coupling.

Various electrolyzer technologies can be used in renewable-powered HRS configurations, including alkaline electrolyzers, proton exchange membrane electrolyzers (PEMWEs), anion exchange membrane electrolyzers (AEMWEs), and solid oxide electrolyzer cells (SOECs). Among them, alkaline electrolyzers are considered a mature and cost-effective technology for large-scale hydrogen

*Corresponding author
E-mail address: emryildirim93@hotmail.com
journal homepage: https://dergipark.org.tr/tr/pub/ijeh

and scalability **[5, 6]**. On the other hand, PEM electrolyzers offer distinct advantages such as high current density operation, compact system design, and rapid dynamic response, making them particularly well-suited for integration with intermittent renewable energy sources **[7]**.

Previous research has explored the techno-economic feasibility of HRS integrated with renewable energy. For instance, Atabay and Devrim analyzed an HRS using AEMWE powered by a 5 MW PV system, reporting a levelized cost of hydrogen (LCOH) of 8.54 €·kg⁻¹ for a daily capacity of 170 kg **[3].** Gökçek and Kale compared hybrid wind-PV-battery and wind-battery configurations, yielding hydrogen costs of 8.92 and 11.08 USD·kg⁻¹, respectively **[8]**. Similarly, Kayfeci et al. indicated that the LCOH for PV/electrolysis systems could reach up to 23.33 USD·kg⁻¹, compared to just 2.08 USD·kg⁻¹ for natural gas-based steam methane reforming **[9]**. While Barhoumi et al. reported an LCOH of 3.32 EUR·kg⁻¹ using PV-electrolysis (excluding compression and storage costs) **[10]**, Zhao and Brouwer found that solar-powered HRS had an LCOH of 9.14 USD·kg⁻¹, reduced to 6.71 USD·kg⁻¹ for wind-powered systems **[11]**. Perna et al. reported an LCOH of 7.92 EUR·kg⁻¹ for an HRS with a capacity of 450 kg/day using PV-assisted alkaline electrolysis **[12]**.

Despite the growing body of literature, most existing studies tend to focus on a single electrolyzer type or general economic trends without conducting a comparative techno-economic analysis of different electrolyzer technologies under identical renewable energy inputs. Moreover, integrated assessments that consider realistic daily refueling capacities, operational lifetimes, and full system-level costs (including compression, storage, and dispensing units) remain limited. These research gaps hinder the development of robust strategies and investment decisions needed to scale up hydrogen infrastructure.

In this study, we aim to address these limitations by presenting a comparative techno-economic analysis of HRS configurations that utilize two different electrolyzer technologies - alkaline and PEM - integrated with a photovoltaic system. HRS systems with alkaline and PEM electrolyzers with a nominal hydrogen production rate of 30 $Nm3.h^{-1}$ were used for comparison. In the alkaline HRS system, the alkaline electrolyzer required 192.5 kW PV installed power and in the PEM HRS system, the PEM electrolyzer required 214.5 kW PV installed power. The levelized cost of hydrogen (LCOH) was calculated over a 10-year operational period, considering capital and operational expenditures.

The findings provide actionable insights for policymakers, researchers, and industry stakeholders to support the design and deployment of sustainable hydrogen infrastructure in line with decarbonization goals.

2. PROPERTY OF HRS

The planned HRS is designed as an integrated system that encompasses on-site hydrogen production, compression, high-pressure storage, and dual-pressure dispensing units for refueling hydrogen-powered vehicles. The facility is capable of producing up to 65 kg of hydrogen per day, which corresponds to the daily refueling needs of approximately 13 hydrogen fuel cell electric vehicles (FCEVs). Two different system configurations are considered for the hydrogen production unit: one based on a 156 kW alkaline electrolyzer, and the other utilizing a 174 kW PEM electrolyzer, both powered by PV systems with a maximum installed capacity of 192.5 kW and 214.5 kW, respectively. The entire HRS system is modular in design and comprises the following main components:

- A 9 m containerized hydrogen production unit (housing the electrolyzer and associated balance-of-plant),
- A 6 m containerized compression unit,
- High-pressure storage tanks with a total water volume of 4350 liters at 450 bar,
- Dispensers for vehicle and boat refueling at two different pressure levels.

Figure 1 provides a schematic overview of the HRS configuration. Both alkaline and PEM-based system layouts follow a similar structural and operational design, differing primarily in electrolyzer technology and corresponding performance characteristics. This dual-configuration approach enables a comparative techno-economic evaluation of the two electrolyzer technologies under identical operating conditions.

Figure 1. Schematic representation of HRS**[13]**

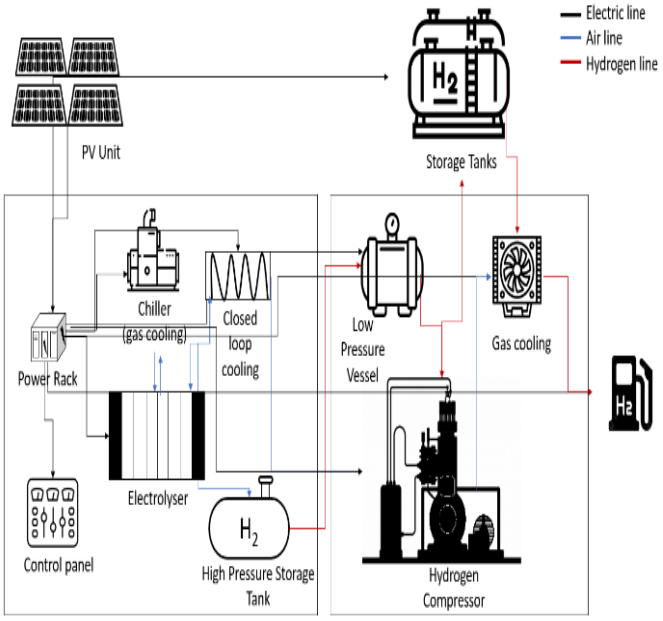

2.1. Method of Process

The hydrogen produced by the electrolyzer is first directed to a low-pressure (LP) storage tank operating at approximately 10 bar. This intermediate storage serves as a buffer before compression. The stored hydrogen is then compressed using a multi-stage hydrogen compressor, which incrementally increases the gas pressure from 10 bar up to 450 bar. Following compression, the hydrogen is transferred to a high-pressure storage system, composed of tanks designed to operate at 450 bar. These storage units ensure the availability of pressurized hydrogen for continuous and efficient refueling operations.

The hydrogen is finally delivered to vehicles via a dispenser unit calibrated to supply fuel at 350 bar. The pressure regulation from the high-pressure storage to the dispensing unit ensures safe and controlled refueling. A schematic flow of this system involves:

Electrolyzer → LP Storage (10 bar) → Compressor → HP Storage (450 bar) → Dispenser (350 bar).

The modular configuration of the HRS offers significant advantages in terms of scalability, on-site hydrogen generation, and integration with renewable energy sources, thereby reducing dependency on centralized hydrogen production and distribution networks. The system's compact design allows for flexible deployment in urban and semi-urban environments, while enabling localized, low-emission hydrogen supply. From a safety perspective, the HRS is equipped with advanced monitoring and control systems, including pressure relief valves, gas leak detectors, and automated emergency shutdown mechanisms, which ensure the safe handling of high-pressure hydrogen throughout the compression, storage, and dispensing processes.

Table 1. Technical specifications of the main components.

PV Panel	
Maximum Power (Pmax) **[14]**	550 W
G1, ref	1000 W/m
Tm, ref	25°C
NOCT	43°C
Temperature Coefficient, μ_p	0,00005
Number of PV Panels for Alkaline Electrolyzer	350
Number of PV Panels for PEM Electrolyzer	390
Alkaline Electrolyzer [15]	
Power	156 kW
H_2 Nominal Flow	30 $Nm^3 \cdot h^{-1}$
Power Consumption	5.2 $kWh.Nm^{-3}$
Tap Water Consumption	1.5 - 2 $liters.Nm^{-3}$ H_2
Electrolyte Quantity	360 L
Electrolyte	H_2O + 30% wt. KOH
PEM Electrolyzer [16]	
Power	174 kW
H_2 Nominal Flow	30 $Nm^3 \cdot h^{-1}$
Power Consumption	5.8 $kWh.Nm^{-3}$
Tap Water Consumption	0.8 – 1.2 $liters.Nm^{-3}$ H_2
Hydrogen Compressor [16]	
Mechanical Efficiency	%88
Gas Storage System (NEL, n.d.)	
Low-Pressure Buffer Tank	10 bar
Cascade System High-Pressure Tank	450 bar
Cooling Unit (Chiller and Closed Loop Cooling) [16]	
Car Dispensing Pressure	350 bar
Hydrogen delivery temperature	-40°C

2.2. Solar Radiation of Ankara

The quantity of energy generated by solar panels depends on many factors, including panel size, efficiency, amount of sunlight available, and temperature. In addition, it depends on the potential solar radiation and ambient temperature of the region where PV will be installed. The establishment of an HRS using a PV-based renewable energy system was chosen as a possible application area in Çankaya, Ankara, Türkiye. The meterological data's are taken from Turkish State Meteorological Service. Figure 2 shows the total global solar radiation and Figure 3 shows the ambient temperature of Ankara.

Figure 2. Total global solar radiation in Ankara

Figure 3. Ambient temperature of Ankara

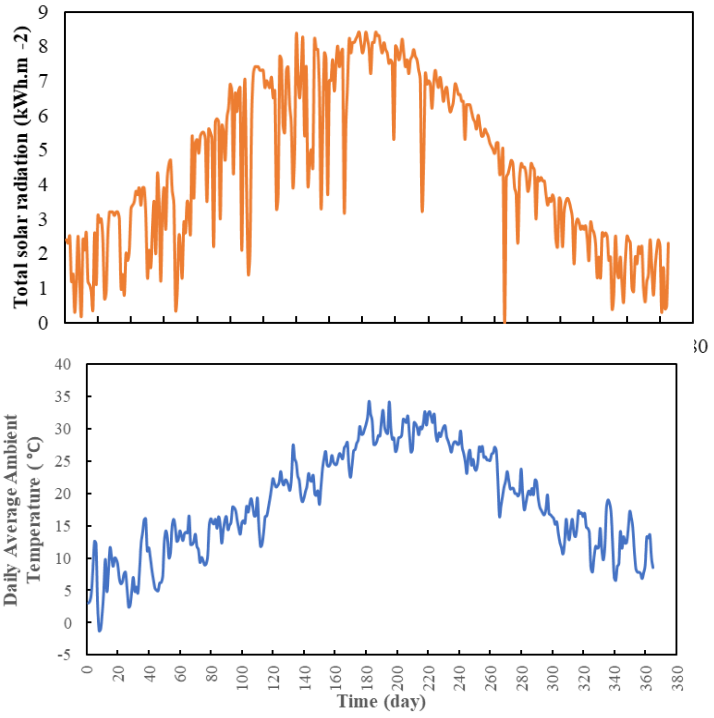

2.3. HRS Components

2.3.1. PV system

Using data on observed daily global irradiance, sunlight length, and ambient temperature, equations 1 and 2 were used to determine the daily power of the PV **[3]**.

$$T_m = T_a + G_1\left(\frac{NOCT - 20}{800}\right) \quad (1)$$

$$P_{PV} = N_{PV}\frac{G_1}{G_{1,ref}}\left[P_{PV,max} + \mu_p(T_m - T_{m,ref})\right] \quad (2)$$

T_m is module temperature (°C), T_a is ambient temperature (°C), G_I and $G_{I,ref}$ refer to solar irradiance and reference solar irradiation of PV (kW/m^2), μ_p is module power coefficient, NOCT is the nominal operating cell temperature **[14]**. While N_{PV} is the number of PV panels, $P_{PV,max}$ is the max power of PV panels. In the system design, a panel with a power of 550 W was selected. While 350 panels were used for the Alkali Electrolyzer, 390 panels were used for the PEM Electrolyzer in the system. Figure 4 shows the maximum power that calculated by Equation 2 produced in PV versus the daily radiation in Ankara.

Figure 4. Daily produced PV power

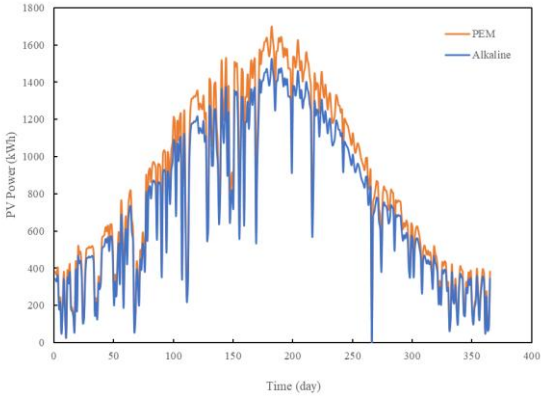

2.3.2. Electrolyzer

The Alkaline Electrolyzer and PEM Electrolyzer are chosen for hydrogen generation in this research. Alkaline electrolyzer operating at up to 10 bar pressure, this electrolyzer can produce 30 Nm^3/h of hydrogen while consuming 150 kW of electricity and utilizing 1.5-2 liters.$m^{-3}H_2$ of tap water. The PEM Electrolyzer, operating at up to 30 bar pressure, can produce 32 Nm^3/h of hydrogen while consuming 150 kW of electricity and utilizing 0.8–1.2 L/m^3 H_2 of tap water Equation 3 calculates the daily energy consumption of an alkaline electrolyzer **[3].**

$$E_{Electrolyzer} = P_{Electrolyzer} \times t_{day} \quad (3)$$

where $E_{Electrolyzer}$ is the electrolyzer's daily electricity consumption (kWh), $P_{Electrolyzer}$ is its nominal power (kW), and t_{day} is the alkaline electrolyzer's operational time.

2.3.3. Hydrogen Compressor

Outlet pressure for commercial alkaline electrolyzer in the proposed Hydrogen refueling station is approximately 10 bar. In order to use it in hydrogen-powered vehicles, A compressor capable of compressing hydrogen at high pressures (450 bar for this system) must be used. Equation 4 was used to calculate the hydrogen compressor's power **[8].**

$$W_{comp} = C_p \frac{T_1}{\eta_c} \left[\left(\frac{P_2}{P_1} \right)^{\frac{r-1}{r}} - 1 \right] m_c \quad (4)$$

where r is the isentropic exponent of hydrogen (r = 1.4), m_c is the gas flow rate through the hydrogen compressor in kilograms per second ($kg.s^{-1}$) , T_1 is the inlet gas temperature of the hydrogen compressor (293 K), η_c is the compressor efficiency, P_1 and P_2 are the inlet and output gas pressures of the hydrogen compressor, respectively, and Cp is the specific heat of hydrogen at constant pressure (14.304 $kJkg^{-1}$ K^{-1}) **[8].**

$$E_{Compressor} = W_{compressor} \times t_{comressor} \quad (5)$$

$E_{Compressor}$ is the daily energy consumption of the compressor and $t_{comressor}$ represents the compressor's daily operating time.

2.3.4. Cooling System

Distribution system is constructed in accordance with the SAE J2601 refueling procedure, which specifies the temperature range for hydrogen precooling (-30/-40°C). Because of its negative Joule-Thompson coefficient, hydrogen expands during refueling, raising the gas's temperature **[8]**. Precooling the hydrogen is necessary to prevent a temperature rise over 85°C, which poses a risk to the hydrogen tank in FCEVs **[4]**. In calculating the required cooling power, it was assumed that hydrogen would fill minutthe vehicle tank at 350 bar and -40 °C for 5 minutes.

Equation 6 was used to calculate HRS's cooling power requirement **[17].**

$$P_{cool} = N_{veh} \dot{m}_{H_2} C_{p_{H_2}} \left(T_{in_{H_2}} - T_{out_{H_2}} \right) \quad (6)$$

where $C_{p_{H_2}}$ is the specific heat for hydrogen at constant pressure ($kJ.kg^{-1}.K^{-1}$), N_{veh} is the number of cars, and $\dot{m}_{H_2}$ is the mass flow rate ($kg.s^{-1}$). The input temperature (K) of hydrogen is $T_{in_{H_2}}$, and the exit temperature (K) of hydrogen is $T_{out_{H_2}}$.

2.4. Techno-Economic Analysis

Economic evaluation based on the LCOH study has been conducted to determine cost of the suggested HRSs**[18]**. Based on the HRS's capacity ($kg.day^{-1}$), LCOH is a useful economic measure that enables determining the ultimate cost of producing, compressing, and storing hydrogen. Equation 7 is used for calculation **[4]**:

$$LCOH = \frac{\text{Total Costs}(\$) - \text{Electrical Revenue}(\$)}{H_2 \text{Annual Production (kg)}} \quad (7)$$

Total costs shown in equation 8 include annual investment costs ($C_{inv,a}$), annual replacement costs ($C_{rep,a}$), and annual operating costs ($C_{O\&M}$) **[12]**.

$$\text{Total Costs (€)} = C_{inv,a} + C_{rep,a} + C_{O\&M} \quad (8)$$

Equations 10 and 11 are used to annualize investment and replacement expenses while taking equation 9's capital recovery factor (CRF) into account **[3].**

$$CRF = \frac{i\,(1+i)^n}{(1+i)^n - 1} \quad (9)$$

$$C_{inv,a} = C_{inv}.CRF \quad (10)$$

$$C_{rep,a} = \frac{C_{rep}}{(1+i)^t} CRF \quad (11)$$

where the plant lifetime (n), the nominal discount rate (i), and t represent the replacement cost and the related year. Table 2 illustrates the techno-economic specs of the components. This table takes into account the cost per kW of the commercial products selected for high efficiency, the operational costs specified in the literature, and the replacement cost per kW for the products that have completed their lifetime in the process selected for the LCOH calculation. In addition, depending on the hydrogen capacities produced, decisions were made for the cooler, compressor and dispenser.

Table 2. Techno-economic specs of the components.

Component	Parameter	Price ($)
PV **[19]**	Installation cost [kW^{-1}]	226,24
	Replacement cost [kW^{-1}]	0
	Operation and maintenance [$year^{-1}$]	56,1
	Pv power (kW)	0,55
	Lifetime [year]	25
Electrolyzer (PEM) **[8]**	Installation cost [kW^{-1}]	1500
	Replacement cost [kW^{-1}]	0
	Operation and maintenance [$year^{-1}$]	6750
	Max electrolyzer power (kW)	150
	Lifetime [year]	10
Electrolyzer (Alkali) **[19]**	Installation cost [kW^{-1}]	1198
	Replacement cost [kW^{-1}]	0
	Operation and maintenance [$year^{-1}$]	3594
	Max electrolyzer power (kW)	150
	Lifetime [year]	10
Storage tank (PEM) **[19]**	Installation cost [kg^{-1}]	585
	Replacement cost [kg^{-1}]	0
	Operation and maintenance [$year^{-1}$]	16380
	Stored H_2 [kg]	140
	Lifetime [year]	20
Storage tank (Alkali) **[19]**	Installation cost [kg^{-1}]	585
	Replacement cost [kg^{-1}]	0
	Operation and maintenance [$year^{-1}$]	15210
	Stored H_2 [kg]	130
	Lifetime [year]	20
Compressor **[20]**	Total Installation cost	125625
	Replacement cost [kg^{-1}]	0
	Operation and maintenance [$year^{-1}$]	25125

	Lifetime [year]	20
Cooling **[3]**	Installation cost [$.kg^{-1}]	5000
	Replacement cost [$.kg^{-1}]	0
	Operation and maintenance [year^{-1}]	0
	Lifetime [year]	20
Dispenser **[8]**	Total Installation cost [$]	54000
	Replacement cost [kW^{-1}]	0
	Operation and maintenance [year^{-1}]	16200
	Lifetime [year]	10

3. RESULT AND DISCUSSION

This study evaluated two HRS configurations, each designed to meet a daily hydrogen demand of 65 kg-sufficient to refuel 13 vehicles equipped with 5 kg tanks. In order to enhance energy reliability, a grid-connected photovoltaic (PV) system was employed. While the PV-generated electricity serves as the primary energy source for both systems, the grid is utilized to compensate for any shortfalls, ensuring continuous operation.

The analysis revealed that the capital expenditure (CAPEX) of HRS configurations is strongly influenced by the required PV capacity. The PV-integrated alkaline HRS demonstrated a total CAPEX of approximately $43,500, whereas the PV-integrated PEM HRS exhibited a higher CAPEX of approximately $48,500. This difference arises from the higher specific energy consumption of the PEM electrolyzer, which necessitates a larger PV capacity to produce the same amount of hydrogen. Excluding the PV system, the electrolyzer represented the most substantial component of the total installation cost. Moreover, the electrolyzer's shorter operational lifespan compared to other system components introduces an additional replacement cost during the system's lifetime.

The findings underscore that the high upfront capital investment remains a key barrier to the widespread deployment of green hydrogen infrastructure, particularly in small-scale applications or in regions with limited financial resources. To ensure the long-term economic viability of HRS systems, it is essential to account for not only initial costs but also ongoing maintenance and replacement expenses. Efficient and optimized system operation should be prioritized to minimize lifecycle costs and support the broader adoption of sustainable hydrogen-based transportation. A comparative analysis of the capital cost distribution for two HRS configurations-integrated with either a PEM electrolyzer or an alkaline electrolyzer-is presented in Figure 5 (a and b).

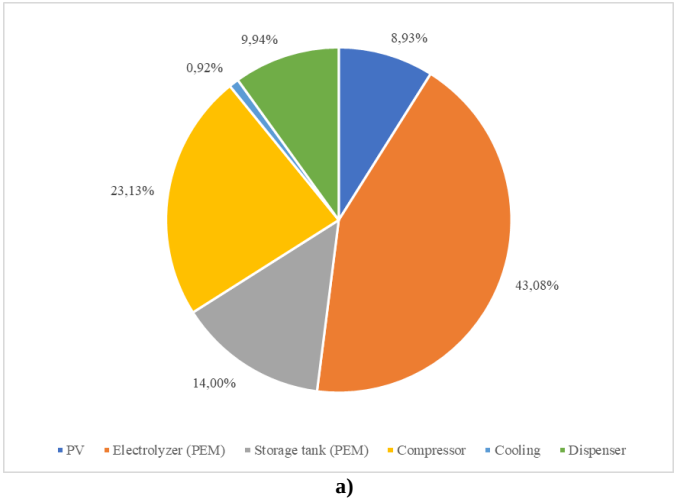

a)

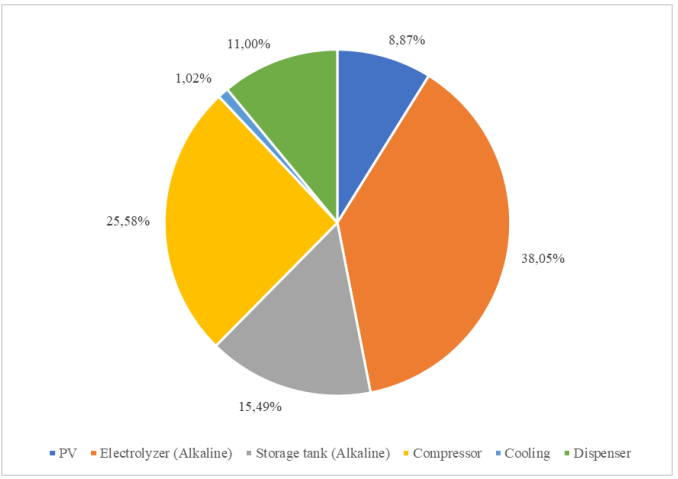

b)

Figure 5. a) Cost ratios of PEM HRS components **b)** Cost ratios of alkaline HRS components

As depicted in Figure 5 (a), the PEM-based system allocates the largest portion of its capital expenditure to the electrolyzer unit (43.08%), followed by the compressor (23.13%) and storage tank (14.00%). In contrast, the alkaline-based system exhibits a slightly more balanced cost structure, with 38.05% allocated to the electrolyzer, 25.58% to the compressor, and 15.49% to the storage tank in Figure 5 (b). The PV subsystem accounts for a similar share in both configurations (approximately 9%), though the absolute PV capacity required in the PEM system is higher due to its greater electricity consumption. Dispenser and cooling systems represent minor but non-negligible shares in both systems. Overall, the PEM-based HRS demonstrates a more capital-intensive profile, largely due to the higher cost and energy demands of PEM technology, whereas the alkaline system distributes costs more evenly across subsystems. These distinctions are particularly relevant for project developers seeking cost-effective solutions for small-scale or budget-constrained hydrogen infrastructure projects.

4. CONCLUSIONS

This study presents a comparative techno-economic analysis of HRS configurations integrated with grid-connected PV systems, taking into account the local climatic and geographical conditions of Ankara, Türkiye. The proposed HRS includes four main components: a water electrolyzer, hydrogen storage unit, PV system, and a dispenser. Two types of electrolyzer technologies-alkaline and PEM-each with a nominal hydrogen production capacity of 30 Nm³/h¹ (equivalent to 65 kg/day), were analyzed in terms of their enera gy requirements, capital investments, and long-term economic performance.

The analysis revealed that the alkaline HRS configuration required approximately 192.5 kW of installed PV capacity, whereas the PEM-based system required 214.5 kW due to its higher specific energy consumption. Over a 10-year operational period, the LCOH was calculated to be 6.39 $/kg· H_2 for the alkaline system and 7.73 USD/kg H_2 for the PEM system. These findings highlight the sensitivity of overall system economics to electrolyzer efficiency and energy input requirements.

In addition to capital expenditures, the study also considers the impact of component reliability and replacement over the system's lifetime. As hydrogen infrastructure comprises various subsystems-such as compressors, cooling units, and dispensers-with different operational lifespans, stochastic component failure and replacement frequencies must be considered for a more realistic cost assessment. As recommended by Atabay and Devrim, incorporating the average number and timing of component replacements improves the accuracy of long-term economic projections **[3].**

Ultimately, while green hydrogen production systems may not yet be economically superior to conventional methods in all contexts, their environmental advantages and alignment with global decarbonization goals make them essential for future energy systems. The integration of renewable sources like PV with HRS infrastructure represents a critical step toward establishing a sustainable, carbon-neutral hydrogen economy. Continued research and policy support will be necessary to reduce initial capital barriers and to promote widespread adoption of such systems at both regional and global scales.

5. RECOMMENDATIONS AND FUTURE WORK

To enhance the economic feasibility and technical reliability of PV-integrated hydrogen refueling stations, several strategies can be recommended. First, further research should focus on the optimization of system components through hybrid configurations, such as the incorporation of battery energy storage systems (BESS) or hybrid renewable sources (e.g., PV-wind combinations) to reduce reliance on grid electricity and to smooth fluctuations in renewable energy supply. Second, future studies should also assess the environmental impacts of such systems through life cycle assessment (LCA), enabling a more holistic evaluation that includes carbon footprint, water use, and resource intensity. Moreover, site-specific analyses using different geographic and climatic conditions would improve generalizability and help identify the most favorable deployment regions.

From a policy perspective, supportive regulatory frameworks and financial incentives-such as feed-in tariffs, carbon credits, or investment subsidies-will be critical to promote early adoption and reduce capital cost burdens. Finally, pilot-scale demonstration projects and real-world data collection are encouraged to validate techno-economic models and guide industry stakeholders and policymakers in making evidence-based decisions regarding green hydrogen infrastructure deployment.

REFERENCES

[1] Republic of Türkiye Ministry of Energy and Natural Resources, "Türkiye Hydrogen Technologies Strategy and Roadmap," *Republic of Türkiye Ministry of Energy and Natural Resources*, 2023. [Online]. Available: https://enerji.gov.tr/Media/Dizin/SGB/en/HSP_en/ETKB_Hydrogen_T_Strategies.pdf [Accessed: Jun. 25, 2025].

[2] P. Arévalo, M. Tostado-Véliz, D. Icaza-Álvarez, and F. Jurado, "Hydrogen-based automotive applications: a promising future," in *Hydrogen Energy Conversion and Management*, Elsevier, 2023, pp. 395–428, doi: 10.1016/B978-0-443-15329-7.00002-8.

[3] R. Atabay and Y. Devrim, "Design and techno-economic analysis of solar energy based on-site hydrogen refueling station," *Int. J. Hydrogen Energy*, vol. 80, pp. 151–160, 2024.

[4] M. Minutillo, A. Perna, A. Forcina, S. Di Micco, and E. Jannelli, "Analyzing the levelized cost of hydrogen in refueling stations with on-site hydrogen production via water electrolysis in the Italian scenario," *Int. J. Hydrogen Energy*, vol. 46, no. 26, pp. 13667–13677, 2020.

[5] S. Brynolf, M. Taljegard, M. Grahn, and J. Hansson, "Electrofuels for the transport sector: A review of production costs," *Renew. Sustain. Energy Rev.*, vol. 81, pp. 1887–1905, 2017.

[6] G. Guandalini, S. Campanari, and G. Valenti, "Comparative assessment and safety issues in state-of-the-art hydrogen production technologies," *Int. J. Hydrogen Energy*, vol. 41, no. 42, pp. 18901–18920, 2016.

[7] R. Ngameni, "PEM water electrolyzers: From electrocatalysis to stack development," *Int. J. Hydrogen Energy*, vol. 35, no. 14, pp. 7811–7822, 2010, doi: 10.1016/J.IJHYDENE.2009.09.015.

[8] M. Gökçek and C. Kale, "Optimal design of a hydrogen refuelling station (HRFS) powered by hybrid power system," Energy Convers. Manag., vol. 161, pp. 215–224, 2018.

[9] M. Kayfeci, A. Keçebaş, and M. Bayat, "Chapter 3 - Hydrogen production," in *Solar Hydrogen Production*, F. Calise, M. Dentice D'Accadia, M. Santarelli, A. Lanzini, and D. Ferrero, Eds. Academic Press, 2019, pp. 45–83, doi: 10.1016/B978-0-12-814853-2.00003-5.

[10] E. M. Barhoumi, P. C. Okonkwo, S. Farhani, I. B. Belgacem, M. Zghaibeh, I. B. Mansir, and F. Bacha, "Techno-economic analysis of photovoltaic-hydrogen refueling station case study: A transport company Tunis-Tunisia," *Int. J. Hydrogen Energy*, vol. 47, no. 58, pp. 24523–24532, 2021.

[11] L. Zhao and J. Brouwer, "Dynamic operation and feasibility study of a self-sustainable hydrogen fueling station using renewable energy sources," *Int. J. Hydrogen Energy*, vol. 40, no. 10, pp. 3822–3837, 2015.

[12] A. Perna, M. Minutillo, S. Di Micco, and E. Jannelli, "Design and costs analysis of hydrogen refuelling stations based on different hydrogen sources and plant configurations," *Energies*, vol. 15, no. 2, p. 541, 2022.

[13] *Hydrogen Refuelling Stations – Gilbarco Veeder-Root*, [Online]. Available: https://www.gilbarco.com/eu/our-solutions/hydrogen-refuelling-station-solutions/hydrogen-refuelling-stations. [Accessed: Jun. 26, 2025].

[14] Gazioğlu Solar, "550 Watt A+ Half Cut Monokristal Perc Yeni Nesil Güneş (Solar) Panel,". [Online]. Available: https://www.argefen.com/urun/gazioglu-solar-550-watt-a-half-cut-monokristal-perc-yeni-nesil-gunes-solar-panel-11bb [Accessed: May 20, 2025].

[15] Cummins, "HySTAT Alkaline Electrolyzer,". [Online]. Available: https://www.cummins.com/sites/default/files/2021-08/cummins-hystat-30-specsheet.pdf [Accessed: Jun. 17, 2025].

[16] NEL, "PEM Electrolyzer,". [Online]. Available: https://nelhydrogen.com/wp-content/uploads/2024/09/Electrolysers-Brochure_PD-0600-0125-Rev-F.pdf [Accessed: Jun. 17, 2025].

[17] A. Elgowainy, K. Reddi, D. Lee, N. Rustagi, and E. Gupta, "Techno-economic and thermodynamic analysis of pre-cooling systems at gaseous hydrogen refueling stations," *Int. J. Hydrogen Energy*, vol. 42, no. 49, pp. 29067–29079, 2017.

[18] L. Viktorsson, J. Heinonen, J. Skulason, and R. Unnthorsson, "A step towards the hydrogen economy-A life cycle cost analysis of a hydrogen refueling station," *Energies*, vol. 10, no. 6, p. 763, 2017.

[19] H. Tebibel, "Dual-objective optimization of solar driven alkaline electrolyzer system for on-site hydrogen production and storage: Current and future scenarios," *Renew. Energy*, vol. 237, p. 121784, 2024.

[20] G. Parks, R. Boyd, J. Cornish, and R. Remick, *Hydrogen Station Compression, Storage, and Dispensing: Technical Status and Costs*, NREL, Golden, CO, USA, Tech. Rep. NREL/BK-6A10-58564, May 2014. [Online]. Available: https://www.nrel.gov/docs/fy14osti/58564.pdf. [Accessed: Jun. 26, 2025].

International Journal of Energy Horizon 01 (2025) 26-31

International Journal of Energy Horizon

journal homepage: https://dergipark.org.tr/tr/pub/ijeh

Research Paper

Utilization of Aluminium for Hydrogen Production: A Sustainable and In-Situ Approach

Vinay Yadav[1], Farrukh Khalid[2*]

[1,2]Indian Institute of Technology Guwahati, India
[1]ORCID No: 0009-0004-9119-4361
[2]ORCID No: 0000-0003-4600-3496

ARTICLE INFO

Article History:

Received:12 June 2025
Accepted:25 June 2025
Available online: 30 June 2025

Keywords:

Aluminium
Hydrogen
Sustainable
In-situ approach
Scrap utilisation

ABSTRACT

The production of hydrogen from affordable and widely available resources is necessary for the broader adoption of hydrogen as a sustainable energy carrier. Aluminium, because of its significant energy content per unit mass, natural abundance, and recyclability, has attracted significant attention as a reactive material for on-demand hydrogen generation when combined with water or reducing agents such as sodium borohydride ($NaBH_4$) and hydrogen chloride (HCl). Furthermore, aluminium scraps are a valuable resource which can be used to produce various useful products such as hydrogen, alumina, potash alum, etc. A major limitation in utilising aluminium for hydrogen production is the development of a stable oxide layer (Al_2O_3) on its outer layer, which inhibits its reaction with water. To overcome this barrier and improve hydrogen yield, various activation techniques have been explored. This review critically examines several activation methods aimed at enhancing the reactivity of aluminium, including salt-assisted activation, metal-assisted activation, particle size reduction, etc. The study concludes with a discussion on future directions, emphasising the need for environmentally friendly activation strategies, reusable reaction systems, and integration with aluminium scrap recycling and renewable energy systems to support sustainable hydrogen production.

1. INTRODUCTION

The growing global population and enhanced living standards have led to a substantial rise in energy demand. Although the majority of current energy needs are met through fossil fuels, their limited availability and the environmental issues they cause have highlighted the urgent need for alternative energy sources. Renewable resources like solar and wind offer cleaner alternatives, but their intermittent and location-dependent nature has limited their large-scale deployment. Despite these challenges, reliance on renewable energy sources is growing rapidly (as shown in Fig. 1) **[1]**. In response to these concerns, extensive research has been conducted to identify clean, reliable alternatives to traditional fossil fuels. Hydrogen is one of the most promising alternative energy options, as it produces only water during combustion, making it an environmentally friendly fuel. This clean characteristic has attracted significant interest, with ongoing focus on improving and optimising hydrogen production methods.

In contrast to conventional batteries, a fuel cell operates like a continuous "factory" for redox-based energy conversion. While energy storage devices such as lithium-ion, lead-acid, and manganese-based batteries can only deliver energy for a limited period before needing recharging, fuel cells continue to generate electricity as long as fuel is supplied. Similarly, internal combustion engines also function continuously, but they involve complex steps to convert chemical energy into mechanical and then into electrical energy. In contrast, fuel cells directly convert chemical energy into electrical energy, resulting in higher overall efficiency. These advantages make fuel cells a promising and commercially viable energy technology, prompting extensive ongoing research. The fundamental reaction in a fuel cell is as given in equation (1).

$$H_2(g) + 0.5\ O_2(g) \longrightarrow H_2O(g) + \text{Heat} \quad (1)$$

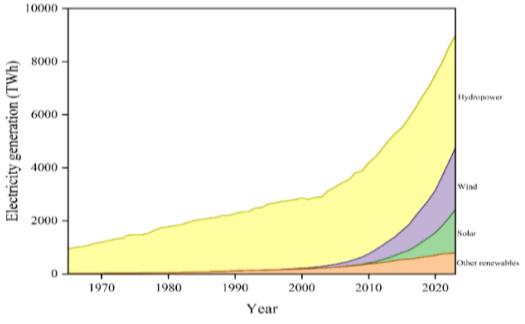

Figure 1. Global renewable electricity generation **[1]**

*Corresponding author
E-mail address: f.khalid@iitg.ac.in
journal homepage: https://dergipark.org.tr/tr/pub/ijeh

Hydrogen has a very high gravimetric energy density of 120 MJ/kg, which is about three times that of gasoline (44 MJ/kg), making it an excellent energy carrier by weight. However, its volumetric energy density is significantly lower (approximately 0.01 MJ/L) compared to 32 MJ/L for gasoline. This low volumetric density presents a major challenge for practical applications. Therefore, developing high-density hydrogen storage methods is crucial for improving the overall performance and feasibility of hydrogen-based systems, including proton exchange membrane (PEM) fuel cells **[2-10]**.

Recent research has explored the potential of multinary semiconductors for converting solar energy into hydrogen effectively **[11]**. Additionally, ammonia borane has been considered a viable hydrogen source because of its high hydrogen content (over 19.6 wt%) and ability for regeneration. Although the release of ammonia as a by-product leads to corrosion of both containers and catalysts, significantly reducing performance (around 95 Wh/kg), which is much lower than that of the sodium borohydride ($NaBH_4$) system (200-400 Wh/kg). Moreover, ammonia borane can act as a catalyst poison, limiting its applicability in fuel cell systems **[9, 12-14]**. In contrast, formic acid presents several advantages as a hydrogen carrier. It offers a high volumetric hydrogen capacity (53 g H_2/L), low toxicity, and low flammability in ambient conditions, making it a safer and more practical option for hydrogen storage and transport.

Although lithium-ion batteries are the leading technology for energy storage at present, they have several limitations, including lower power density, safety concerns, limited life, long recharging times, high cost, and limited design flexibility. These drawbacks have driven the search for alternative energy systems with better overall performance. Fuel cells have emerged as a strong option in this regard. They convert chemical energy directly to electrical energy with high efficiency and emit only water as a by-product. Additionally, fuel cells have no moving parts, offer potentially long operational lifetimes, and their energy output is not constrained by the physical size of the cell, unlike batteries. Despite these advantages, the widespread adoption of fuel cells is challenged by factors such as high cost, moderate power density, efficiency limitations, and lifespan issues. Furthermore, fuel accessibility, storage methods, and the required operating temperatures add to the complexity of fuel cell systems. A typical proton exchange membrane (PEM) fuel cell setup includes three main components: a fuel cell stack, a hydrogen generator, and a hydrogen storage unit. Hydrogen is fed to the anode of the fuel cell by the storage unit, and the performance of the cell is influenced by the hydrogen purity, back pressure, and flow rate **[15,16]**. In recent years, chemical hydrides have gained attention as promising hydrogen storage materials considering their stability at ambient conditions and potential to liberate hydrogen instantly through chemical breakdown. Common hydrides comprise alanate hydrides, alkali metal hydrides, and metal hydroborates, with compounds such as $NaBH_4$, $Zn(BH_4)_2$, $Ca(BH_4)_2$, $LiAlH_4$, and $NaBH(OCH_3)_3$ being the most studied. Among them, sodium borohydride ($NaBH_4$) stands out due to its relatively lower cost and high hydrogen content (10.6 wt%). However, its hydrolysis reaction produces sodium metaborate $NaBO_2$, and a removal or recycling system is essential for practical applications **[17]**. In addition to chemical hydrides, various organic compounds have also shown potential for high-rate and efficient hydrogen production. However, their commercialisation is limited by the need for expensive catalysts **[18]**.

Water is an abundant and cost-effective source of hydrogen, offering a high hydrogen content. Aluminium (Al), on the other hand, is widely available in the Earth's crust and possesses a range of desirable physical and chemical properties. These include lower density (2700 kg/m^3), high hardness, excellent ductility, strong thermal and electrical conductivity, naturally anti-corrosive, and high reflectivity. Due to these characteristics, aluminium has gained attention as a potential energy carrier. Its ability to resist corrosion is largely due to the formation of the stable oxide layer, which is both non-toxic and colorless. Moreover, aluminium can be converted into porous sodium alanate ($NaAlH_4$), a material that serves as an effective medium for hydrogen storage **[19-21]**.

Hydrogen can be produced through various methods, including thermochemical, electrolytic, solar, and biological processes. However, current green hydrogen production technologies still face problems in terms of efficiency and cost-effectiveness. For instance, photovoltaic electrolysis cells remain uneconomical. Currently, the major portion of hydrogen is generated through hydrocarbons and alcohol reforming **[22]**, coal and fossil fuels gasification **[23-26]**, water electrolysis **[27]**, renewable energy-based systems **[28]**, thermochemical cycles, electro-thermochemical (hybrid thermochemical) cycles and alternative approaches like aluminium-based methods **[29-40]**, ammonia reforming **[41]**, and plasma reforming **[42-44]**. Among these, the reforming of hydrocarbons and alcohols such as alkanes, alkyl alcohols, and glycerol is commonly carried out using auto-thermal reforming and partial oxidation techniques. However, partial oxidation is challenged by a lower hydrogen-to-carbon monoxide ratio, complex operational requirements, and the need for high operating temperatures **[45]**. Auto-thermal reforming, which involves oxygen consumption, is generally not cost-effective and therefore has limited commercial application **[3,45]**. In coal gasification, various coal types are converted into syngas by reacting them with air, steam, or oxygen at elevated temperatures (>900 °C) in a gasifier **[24]**. This process suffers from low efficiency due to the carbon-rich feedstock and is also associated with high greenhouse gas (GHG) emissions **[3,46]**. Electrolysis, although a clean method of hydrogen production, demands high electrical energy input and involves the use of expensive membranes, which increases operational costs **[47]**. Aluminium-based hydrogen production methods involve reactions between aluminium and water or acids, often with the addition of inhibitors to control the process **[29-40]**. The general aluminium hydrolysis and hydrochlorination reactions are given in (2), (3), and (4) **[48,49]**. According to reactions (2) and (3), the absolute hydrolysis of 1 gram of aluminium in a non-acidic medium can produce approximately 1245 mL of hydrogen gas at normal temperature and pressure (NTP). The by-products of this reaction, i.e. aluminium hydroxide ($Al(OH)_3$) and aluminium oxyhydroxide (AlOOH), are stable, amti-corrosive, and serve as valuable raw materials for the ceramics and related industries. Hydrogen produced through this route is influenced by the alkalinity of the solution and can be regulated by adjusting the reaction temperature **[20]**. These reactions are most effective when aluminium is in fresh or activated form, which enhances its reactivity. Furthermore, integrating a hydrogen/air sub-cell into the system has been shown to increase the maximum power output by up to 20% **[50]**. While these methods offer simplicity and utilize abundant resources, they suffer from uncontrolled hydrogen release due to the exothermic nature of the reactions, which can pose safety and efficiency challenges. In this study, we focus on the direct production of hydrogen with an in-depth discussion on the underlying mechanism. The techniques employed to enhance aluminium reactivity for more efficient hydrogen generation.

$$2Al + 4H_2O \longrightarrow 2AlOOH + 3H_2 \quad (2)$$

$$2Al + 6H_2O \longrightarrow 2Al(OH)_3 + 3H_2 \quad (3)$$

$$2Al + 6HCl \longrightarrow 2AlCl_3 + 3H_2 \quad (4)$$

2. ACTIVATION OF ALUMINIUM

Due to the presence of an oxide layer on the aluminium surface, the aluminium should be activated, or the oxide layer should be removed to increase the surface area for reaction. Various methods are available, which are discussed in this section.

2.1 Aluminium Activation by Gallium-Indium

High intensity energy (HIE) processing of aluminium (Al) powder using a Gallium (Ga)-Indium (In) eutectic alloy, using a planetary ball mill at 220 rpm for 3 minutes, significantly enhanced the metal's reactivity toward water. The milling process employed a steel ball having a diameter of 6 mm, with a powder-to-ball mass proportion of 1:30. In contrast, low intensity energy (LIE) processing involved manually mixing the Ga-In alloy powder in Al powder using a ceramic mortar in a nitrogen gas atmosphere. The results revealed a significant difference in hydrogen generation rates between the two methods. LIE-treated aluminium achieved the highest hydrogen production rate of 11 mL/min, while the HIE-treated sample generated a substantially higher rate of 1.28 L/min when 1 g of Al is used. Although the eutectic Ga-In alloy improved the reactivity of aluminium, it also led to increased brittleness in the material. Temperature was found to significantly impact hydrogen generation in both cases. For LIE-treated aluminium, the hydrogen generation rate improved with temperature, with values of 11 and 95 mL/g/min at 24 °C to 61 °C, respectively. Similarly, for HIE-treated aluminium, the yield was enhanced from 1.28 to 2.60 L/g/min when the temperature rose from 21 °C to 59 °C **[51-54]**.

A detailed investigation was carried out to evaluate the optimal temperature and pressure conditions for activating aluminium using Ga-In alloy. The results revealed that the formation of aluminium oxyhydroxide is thermodynamically beneficial at ambient pressure and temperatures more than 21 °C. In contrast, the formation of aluminium hydroxide is achievable by maintaining the reaction at lower temperatures or under higher pressure. By carefully adjusting the reaction conditions, water consumption in the system can be decreased up to 33.3% with no effect on the overall hydrogen production. This is achieved by directing the reaction pathway toward the formation of AlOOH. Furthermore, by manipulating the operating parameters, different by-products can be selectively produced, each with distinct industrial applications **[55]**.

2.2 Size of Particles

Aluminium powders of both nano and micro scale sizes can interact with water under atmospheric pressure and moderate temperatures for hydrogen generation. Nanosized Al particles are capable of reacting completely with water even at 20 °C, while micro-sized Al particles require a temperature above 40 °C for effective hydrogen generation. This indicates that smaller Al particles can initiate hydrogen production without the need for any prior activation or surface reformation. Initially, the reaction is governed by the accessible surface area of the Al particles, while in later stages it is controlled by the diffusion of water molecules through the by-product layer formed on the particle surface. The induction time for the onset of the reaction depends on the hydrogen diffusion within the bulk aluminium and the critical pressure of gas in hydrogen bubbles formed at the Al/Al_2O_3 interface. It has been observed that the activation energy for the reaction increases with the average size of the aluminium particles, likely due to the broader particle size distribution associated with larger particles. The reaction by-products may include baeyerite, boehmite, or a combination of both, and their composition is influenced by the temperature at which the reaction takes place **[32]**.

Aluminium powders produced through ball milling have demonstrated an exceptionally high capacity to generate hydrogen from aqueous solutions, even at balanced or near-balanced pH levels. Studies have demonstrated that ball milling aluminium with various additives such as sodium hydroxide (NaOH), cobalt oxide (CoO), and molybdenum oxide (MoO_3) significantly alters the morphology and microstructure of the Al particles. These structural changes are highly dependent on the milling duration and operating conditions. One of the key factors contributing to the enhanced hydrogen generation is the increase in the specific surface area of the aluminium particles. For instance, after 15 minutes of ball milling, the specific surface area of Al was observed to be enhanced dramatically from 0.30 m^2/g to 9.68 m^2/g, thereby promoting more efficient water-splitting reactions. Prolonged ball milling of aluminium decreases the interlayer spacing among particles, resulting in lower reaction rate with water **[56]**.

The proportion of Al to NaCl while milling also plays a significant role in hydrogen generation. A higher concentration of salt was found to enhance the reaction rate, with the maximum average hydrogen production rate recorded at 75 mL/min per gram of Al for an Al to NaCl molar proportion of 5:1. This formulation exhibited 100% conversion within 40 minutes **[57]**. Activated aluminium powder, produced by mechanical pulverisation of Al with silicon powder, graphite powder, bismuth powder, and NaCl, was effectively utilised for hydrogen production. The powder with an optimal Al to salt molar proportion of 0.5 was not only highly reactive but also suitable for long-term air storage. It demonstrated average hydrogen generation rates of approximately 101 mL/g/min and 210 mL/g/min at initial water temperatures of 55 °C and 70 °C, respectively. When a bismuth alloy was used, the highest rates observed were about 287 mL/g/min and 713 mL/g/min at 55 °C and 70 °C, respectively **[58]**. In parallel research, mesoporous alumina catalysts with well-managed pore structure were synthesised through the regulated hydrolysis of aluminium alkoxides. Using water to alumina ratios between 2 and 15, various alumina compositions were developed. After calcination at 700 °C for 2 hours, these supports exhibited surface areas of 240-320 m^2/g, average pore sizes of 4-18 nm, and pore volumes of 0.4-1.6 mL/g **[59]**. Hydrogen production through aluminium oxidation was also demonstrated using water vapour, hydrogen peroxide solutions, and water/oxygen mixtures. Water was found to inhibit surface passivation of aluminium when oxygen was introduced. The formation and expansion of oxide and hydroxide nanoparticles during water oxidation advanced the oxidation front deeper into the aluminium. To ensure safety, the molar ratio of O_2 to H_2 was limited to 13% to prevent excessive hydrogen accumulation and the risk of explosion **[60]**.

2.3 Impact of Zinc or Mercury Amalgamation and $Al(OH)_3$

The aluminium hydrolysis can be effectively operated at temperatures below 65 °C by employing amalgamation with mercury or zinc. This process significantly enhances the hydrogen generation rate, which increases with temperature. The maximum hydrogen evolution rate recorded was 7.25 L/min at 65 °C for aluminium coated with a zinc conglomerate. Among the two, zinc demonstrated a superior activation effect compared to mercury. This is attributed to its lower activation energy requirement of 43.4 kJ/mol for zinc coating versus 74.8 kJ/mol for mercury. Notably, the by-product formed during this reaction, bayerite, is non-toxic and environmentally safe **[61]**. Finely divided and poorly crystalline $Al(OH)_3$ powder has proven to be an effective additive for enhancing hydrogen production in the Al-H_2O system. The proposed mechanism of action involves a reaction given in (5) with a Gibbs free energy change of 39.40 kJ/mol. The surface area of $Al(OH)_3$ plays a major role in influencing the hydrogen yield, with finer particles yielding better performance. By leveraging an on-demand, self-driven exothermic reaction using a relatively large amount of aluminium (3 g Al to 15 g H_2O) and a minimal amount of fine β-$Al(OH)_3$, approximately 70% hydrogen conversion was achieved within 30 minutes. Importantly, this approach eliminates the need for high alkalinity and does not cause corrosion-related issues **[39]**.

$$Al_2O_3 + Al(OH)_3 \longrightarrow 3AlO(OH) \quad (5)$$

2.4 Carbon Nanoparticles (CNTs), Composites, Graphene/Graphite

The hydrogen production rate was observed to improve with the incorporation of carbon nanotubes (CNTs) into the aluminium matrix. CNTs act as localised cathodic sites during the hydrolysis process, facilitating rapid hydrogen production via galvanic corrosion between the CNTs and the aluminium matrix. Although carbon-based by-products arise from the interaction of carbon and water. Yet, no carbon monoxide (CO) generation was found **[62]**. Al@rGO (aluminium-reduced graphene oxide) composites, synthesised via ultrasonic atomization, demonstrated significantly enhanced hydrogen generation upon exposure to pure water under infrared irradiation. The presence of reduced graphene oxide not only accelerates the reaction but also provides ~4nm diffusion pathways for efficient transport of reactants and products **[63]**. Similarly, Al/graphite core-shell composites made from ball milling exhibited effective hydrogen production. When 23 wt% graphite was added, approximately 76.5% of the aluminium content reacted with water to produce hydrogen within 6 hours. An increased reaction temperature enhanced the hydrogen evolution rate, achieving a maximum of 40 ml/g.min Al at 75 °C **[64]**.

Additionally, composites made from bismuth nanoparticle-modified graphene oxide (BiNPs@GO) and bismuth nanoparticles (Bi-NPs), synthesised through hydrothermal processing, showed further improvements in hydrogen generation performance. This enhancement is attributed to the synergetic effects of graphene and nano-bismuth, and notably, the system remained effective even at 0 °C. such composites are promising for hydrogen generation in fuel cells operating under variable temperature and pressure conditions **[65]**.

2.5 Other Agents

The use of water-soluble inorganic salts (such as NaCl and KCl) during milling effectively minimises aluminium passivation in the pH range of 5 to 9. Higher concentrations of these salts, along with smaller aluminium particle sizes, significantly enhance the extent of aluminium reacting with water. Additionally, elevated temperatures not only improve the hydrogen generation rate but also lessen the induction time required to initiate the reaction. Based on the hydrolysis reactions that form aluminium hydroxide and baeyerite, approximately 1446 mL of hydrogen can be generated by just 1 gram of aluminium **[30]**. Alloy ingots composed of Al-Ga-In-Sn_4-Cu have been reported to exhibit superior hydrogen yield and faster production rates compared to Al-Ga-In-Sn_4 alloys. The addition of copper plays a critical role by inhibiting the development of aluminium grains and promoting the pulverisation of the Al(Ga) solid solution. This process increases the surface area available for reaction, thereby enhancing the reactivity of the alloy with water and improving hydrogen production **[66]**.

The activation energy needed for the Al-20%Li alloy was significantly lower than that of the Al-20%Mg alloy. Consequently, Al-20%Li exhibited a hydrogen generation rate of 309.74 mL/g/min and the maximum hydrogen production of 1038 mL/g. In contrast, the yield achieved from Al-20%Mg is found to be approximately 60% of that produced by the Al-20%Li alloy **[67]**. The addition of CaO and Li/Li_2O to aluminium systems was found to greatly increase hydrogen generation. This improvement is attributed to a decrease in activation energy and the autocatalytic properties of the by-product ($Al(OH)_3$) generated during the process **[68]**. Al-based composites synthesised from ball milling mixtures of Al, CaO, and salt powder have also been explored for hydrogen generation. A rise in the content of CaO and NaCl was shown to be favourable, and the highest hydrogen yield was achieved at 30 °C **[69, 70]**. Incorporating hydrides into aluminium-based materials further improved hydrogen generation performance, with lithium hydride (LiH) demonstrating the best results. An Al-30 mol% LiH sample, milled for 3 hours, achieved a hydrogen yield of 96.3% and a peak generation rate of 4556.3 mL/g.min at 75 °C **[34, 71]**. Additionally, hydrolysis of waste aluminium in a mildly alkaline solution (~70 °C) using Ni or Ni/Bi additives produced impressive results. This setup achieved a hydrogen generation rate of 9.00 L/g/min and an overall yield of 1.35 L/g, having nearly a 100% conversion rate **[72]**.

Bismuth-based composites have demonstrated effective activation properties, and the Al-$Bi_2O_2CO_3$ system, prepared via ball milling, has been successfully employed for hydrogen generation. The hydrogen production efficiency was influenced by several factors, including the $Bi_2O_2CO_3$ content, ball milling duration, and the powder-to-ball ratio. The hydrolysis reaction yielded by-products such as $Bi_2O_2CO_3$, AlO(OH), and Al_2O_3. Doping the Al-15 wt% $Bi_2O_2CO_3$ composite with 5 wt% of NaCl or $AlCl_3$ effectively eliminated the induction period and significantly enhanced both the hydrogen yield and

generation rate. The initial temperature of the reaction influenced the rate of hydrogen production, though it had a minimal effect on the overall yield. Additionally, the reaction yield was affected by the ageing time of the composite when exposed to air **[73]**.

2.6 Aluminium Reaction with Steam

Shmelev et al. performed an experiment to generate hydrogen by hydrolysis of molten Al (900-950 °C) in a reactor **[74]**. They used a stainless-steel reactor with a diameter of 42 mm and a height of 82 mm. A maximum of 40% hydrogen yield was observed, which was increased to 100% by adding 10% KOH in molten Al. Furthermore, it was concluded that the reactor could produce a maximum of 13 L of hydrogen per minute from 1 L of the melted Al. Gao et al. investigate the characteristics and working mechanism of aluminium-gas water and aluminium-liquid water reactions at temperatures ranging from 250-376 °C and pressures between 4.0-23.5 MPa **[75]**. They found that supercritical steam showed strong reactivity, inhibiting passivation, with 8 mm aluminium particles completely oxidised at 376 °C and 23.5 MPa. However, steam-based hydrogen yield was observed to be slightly less or equal when compared to liquid water-based reactions due to differences in working mechanisms and aluminium surface contact opportunities. Wang et al. demonstrated the hydrogen production behaviour of millimetre-sized aluminium spheres reacting with subcritical and supercritical water, without the use of any additives or catalysts **[76]**. The effect of reaction time, temperature, and aluminium sphere size on hydrogen generation is systematically analysed. The results reveal that the aluminium-water reaction proceeds through four distinct stages, with hydrogen production increasing over time. For a 6.35 mm aluminium sphere, a maximum hydrogen yield of 86.7% is achieved at temperatures between 550-600 °C. Furthermore, reducing the aluminium sphere size significantly enhances reactivity. Spheres with a diameter of 2.38 mm attain a hydrogen yield of up to 95% and a reaction ratio of 91.71%. These findings suggest that the reaction between millimetre-sized aluminium and sub/supercritical water holds potential for integrated hydrogen, heat, and electricity generation systems.

3. CONCLUSION

This review highlights the potential of aluminium (Al) for hydrogen production, with surface passivation identified as a key barrier to efficient Al-water reactions. Various strategies and conditions that enhance Al hydrolysis have been thoroughly examined. Among the promising approaches, mechanically milled Al nanoparticles (~4nm) combined with NaCl at an Al-to-salt ratio of 0.5 demonstrated both cost-effectiveness and high performance, yielding 101 ml H_2/g/min at 55 °C and 210 ml H_2/g/min at 70 °C. The inclusion of carbon-based materials significantly improved hydrogen output. The type of aluminium precursor, such as mesoporous/microparticle Al, $Al(OH)_3$, Al_2O_3 and $AlCl_3$, also influenced the yield positively. Additives like NaCl, KCl, CaO, carbon nanotubes (CNTs), and graphene further enhanced hydrogen generation. Surface activation through amalgamation with Zn or Hg, and alloying with elements such as Bi, Sn, Ga, In, and Cu, notably increased reactivity and hydrogen yield. The use of waste Al as a hydrogen source was also explored, with galvanic corrosion promoted by elements like Bi and Ga playing a significant role. Since these metals are expensive, alternatives should be explored, despite their recyclability. Key challenges remain in scaling this technology, particularly in managing the accumulation of hydrolysis by-products such as $Al(OH)_3$ and AlOOH, which form surface deposits and inhibit reaction progress. Efficient removal strategies for these by-products and for excess heat generated during the reaction must be developed. Finally, integrated studies combining the most effective approaches discussed in this review are necessary to overcome current limitations and advance aluminium-based hydrogen generation technologies.

REFERENCES

[1] Renewable Energy - Our World in Data, [Online]. Available: https://ourworldindata.org/renewable-energy. [Accessed: Jun. 4, 2025].

[2] A. A. Basheer and I. Ali, "Water photo splitting for green hydrogen energy by green nanoparticles," Int. J. Hydrogen Energy, vol. 44, 2019, doi: 10.1016/j.ijhydene.2019.03.040.

[3] I. Dincer and C. Acar, "Review and evaluation of hydrogen production methods for better sustainability," Int. J. Hydrogen Energy, vol. 40, no. 34, 2014, doi: 10.1016/j.ijhydene.2014.12.035.

[4] I. Dincer and C. Acar, "Innovation in hydrogen production," Int. J. Hydrogen Energy, vol. 42, 2017, doi: 10.1016/j.ijhydene.2017.04.107.

[5] R. S. El-Emam and H. Özcan, "Comprehensive review on the techno-economics of sustainable large-scale clean hydrogen production," J. Clean. Prod., vol. 220, 2019, doi: 10.1016/j.jclepro.2019.01.309.

[6] A. Ersoz, H. Olgun, and S. Ozdogan, "Reforming options for hydrogen production from fossil fuels for PEM fuel cells," J. Power Sources, vol. 154, no. 1, 2006, doi: 10.1016/j.jpowsour.2005.02.092.

[7] H. Fayaz et al., "An overview of hydrogen as a vehicle fuel," Renew. Sustain. Energy Rev., vol. 16, 2012, doi: 10.1016/j.rser.2012.06.012.

[8] D. W. Hurtubise, D. A. Klosterman, and A. B. Morgan, "Development and demonstration of a deployable apparatus for generating hydrogen from the hydrolysis of aluminum via sodium hydroxide," Int. J. Hydrogen Energy, vol. 43, no. 14, pp. 6777–6788, 2018, doi: 10.1016/j.ijhydene.2018.02.087.

[9] J. Kim and T. Kim, "Compact PEM fuel cell system combined with all-in-one hydrogen generator using chemical hydride as a hydrogen source," Appl. Energy, vol. 160, pp. 275–285, 2015, doi: 10.1016/j.apenergy.2015.03.084.

[10] P. Nikolaidis and A. Poullikkas, "A comparative overview of hydrogen production processes," Renew. Sustain. Energy Rev., vol. 67, pp. 597–611, 2017, doi: 10.1016/j.rser.2016.09.044.

[11] J. E. Seo, Y. Kim, Y. Kim, K. Kim, J. H. Lee, D. H. Lee, and S. W. Nam, "Portable ammonia-borane-based H_2 power-pack for unmanned aerial vehicles," J. Power Sources, vol. 254, pp. 1–8, 2014, doi: 10.1016/j.jpowsour.2013.11.112.

[12] J. Eppinger and K. W. Huang, "Formic acid as a hydrogen energy carrier," ACS Energy Lett., vol. 2, no. 1, pp. 188–195, 2017, doi: 10.1021/acsenergylett.6b00574

[13] J. Luo, X. Kang, C. Chen, J. Song, D. Luo, and P. Wang, "Rapidly releasing over 9 wt % of H_2 from NH_3BH_3–Mg or NH_3BH_3–MgH_2 composites around 85 °C," J. Phys. Chem. C, vol. 120, no. 33, pp. 18435–18441, 2016, doi: 10.1021/acs.jpcc.6b04230.

[14] X. Zhang, L. Kam, and T. J. Williams, "Dehydrogenation of ammonia borane through the third equivalent of hydrogen," Dalton Trans., vol. 45, no. 18, pp. 7392–7397, 2016, doi: 10.1039/c6dt00604c.

[15] Fuel Cells | Department of Energy, [Online]. Available: https://www.energy.gov/eere/fuelcells/fuel-cells. [Accessed: Jun. 5, 2025].

[16] S. M. Kwon, S. Kang, and T. Kim, "Development of $NaBH_4$-based hydrogen generator for fuel cell unmanned aerial vehicles with movable fuel cartridge," Energy Procedia, vol. 158, pp. 2241–2246, 2019, doi: 10.1016/j.egypro.2019.01.443.

[17] A. Braunschweiler, Catalytic dehydrogenation of liquid organic hydrogen carriers, M.Sc. thesis, Aalto Univ., Nov. 6, 2018. [Online]. Available: https://aaltodoc.aalto.fi/handle/123456789/34676. [Accessed: Jun. 26, 2025].

[18] M. Veronica Sofianos, D. A. Sheppard, E. Ianni, T. D. Humphries, M. R. Rowles, S. Liu, and C. E. Buckley, "Novel synthesis of porous aluminium and its application in hydrogen storage," J. Alloys Compd., vol. 702, pp. 114–120, 2017, doi: 10.1016/j.jallcom.2017.01.254.

[19] Aluminum: uses, applications - Metalpedia, [Online]. Available: http://metalpedia.asianmetal.com/metal/aluminum/application.shtml. [Accessed: Jun. 5, 2025].

[20] M. Mahinroosta and A. Allahverdi, "Hazardous aluminum dross characterization and recycling strategies: A critical review," J. Environ. Manage., vol. 223, pp. 452–468, 2018, doi: 10.1016/J.JENVMAN.2018.06.068.

[21] H. Zou, S. Chen, Z. Zhao, and W. Lin, "Hydrogen production by hydrolysis of aluminum," J. Alloys Compd., vol. 578, pp. 571–576, 2013, doi: 10.1016/j.jallcom.2013.06.016.

[22] A. M. Al-Bassam, J. A. Conner, and V. I. Manousiouthakis, "Natural-gas-derived hydrogen in the presence of carbon fuel taxes and concentrated solar power," ACS Sustainable Chem. Eng., vol. 6, no. 3, pp. 3731–3742, 2018, doi: 10.1021/acssuschemeng.7b02745.

[23] L. J. Guo, H. Jin, Z. W. Ge, Y. J. Lu, and C. Q. Cao, "Industrialization prospects for hydrogen production by coal gasification in supercritical water and novel thermodynamic cycle power generation system with no pollution emission," Sci. China Technol. Sci., vol. 58, no. 12, pp. 2084–2093, 2015, doi: 10.1007/s11431-015-5967-0.

[24] A. Midilli, H. Kucuk, M. E. Topal, U. Akbulut, and I. Dincer, "A comprehensive review on hydrogen production from coal gasification: Challenges and opportunities," Int. J. Hydrogen Energy, vol. 46, no. 62, pp. 31770–31797, 2021, doi: 10.1016/j.ijhydene.2021.05.088.

[25] M. Muresan, C. C. Cormos, and P. S. Agachi, "Techno-economical assessment of coal and biomass gasification-based hydrogen production supply chain system," Chem. Eng. Res. Des., vol. 91, no. 8, pp. 1376–1386, 2013, doi: 10.1016/j.cherd.2013.02.018.

[26] S. S. Seyitoglu, I. Dincer, and A. Kilicarslan, "Energy and exergy analyses of hydrogen production by coal gasification," Int. J. Hydrogen Energy, vol. 42, no. 4, pp. 2550–2561, 2017, doi: 10.1016/j.ijhydene.2016.08.228.

[27] J. Yates, R. Daiyan, R. Patterson, R. Egan, R. Amal, A. Ho-Baillie, and N. L. Chang, "Techno-economic analysis of hydrogen electrolysis from off-grid stand-alone photovoltaics incorporating uncertainty analysis," Cell Rep. Phys. Sci., vol. 1, no. 10, p. 100209, 2020, doi: 10.1016/j.xcrp.2020.100209.

[28] B. W. McQuillan, L. C. Brown, G. E. Besenbruch, R. Tolman, T. Cramer, B. E. Russ and A. Lewandowski, "High efficiency generation of hydrogen fuels using solar thermal chemical splitting of water (Solar Thermo Chemical Splitting for H_2)," ResearchGate, 2010. [Online]. Available: https://www.researchgate.net/publication/273450634. [Accessed: Jun. 26, 2025].

[29] X. Chen, Z. Zhao, X. Liu, M. Hao, A. Chen, and Z. Tang, "Hydrogen generation by the hydrolysis reaction of ball-milled aluminium–lithium alloys," J. Power Sources, vol. 254, pp. 140–146, 2014, doi: 10.1016/j.jpowsour.2013.12.113.

[30] E. Czech and T. Troczynski, "Hydrogen generation through massive corrosion of deformed aluminum in water," Int. J. Hydrogen Energy, vol. 35, no. 3, pp. 1029–1037, 2010, doi: 10.1016/j.ijhydene.2009.11.085.

[31] P. Dupiano, D. Stamatis, and E. L. Dreizin, "Hydrogen production by reacting water with mechanically milled composite aluminum-metal oxide powders," Int. J. Hydrogen Energy, vol. 36, no. 8, pp. 4781–4791, 2011, doi: 10.1016/j.ijhydene.2011.01.062.

[32] W. Z. Gai, W. H. Liu, Z. Y. Deng, and J. G. Zhou, "Reaction of Al powder with water for hydrogen generation under ambient condition," Int. J. Hydrogen Energy, vol. 37, no. 17, pp. 13132–13140, 2012, doi: 10.1016/j.ijhydene.2012.04.025.

[33] A. V. Ilyukhina, A. S. Ilyukhin, and E. I. Shkolnikov, "Hydrogen generation from water by means of activated aluminum," Int. J. Hydrogen Energy, vol. 37, no. 21, pp. 16445–16452, 2012, doi: 10.1016/j.ijhydene.2012.02.175.

[34] Y. Liu, X. Wang, H. Liu, Z. Dong, S. Li, H. Ge, and M. Yan, "Improved hydrogen generation from the hydrolysis of aluminum ball milled with hydride," Energy, vol. 72, pp. 636–641, 2014, doi: 10.1016/j.energy.2014.05.060.

[35] G. L. Ma, H. B. Dai, D. W. Zhuang, H. J. Xia, and P. Wang, "Controlled hydrogen generation by reaction of aluminum/sodium hydroxide/sodium stannate solid mixture with water," Int. J. Hydrogen Energy, vol. 37, no. 7, pp. 5874–5880, 2012, doi: 10.1016/j.ijhydene.2011.12.157.

[36] H. X. Meng, N. Wang, Y. M. Dong, Z. L. Jia, L. J. Gao, and Y. J. Chai, "Influence of M–B (M = Fe, Co, Ni) on aluminum–water reaction," J. Power Sources, vol. 268, pp. 468–475, 2014, doi: 10.1016/j.jpowsour.2014.06.094.

[37] A. Newell and K. R. Thampi, "Novel amorphous aluminum hydroxide catalysts for aluminum–water reactions to produce H_2 on demand," Int. J. Hydrogen Energy, vol. 42, no. 37, pp. 23421–23429, 2017, doi: 10.1016/j.ijhydene.2017.04.279.

[38] L. Soler, A. M. Candela, J. Macanás, M. Muñoz, and J. Casado, "Hydrogen generation by aluminum corrosion in seawater promoted by suspensions of aluminum hydroxide," Int. J. Hydrogen Energy, vol. 34, no. 20, pp. 8867–8873, 2009, doi: 10.1016/j.ijhydene.2009.08.008.

[39] H. T. Teng, T. Y. Lee, Y. K. Chen, H. W. Wang, and G. Cao, "Effect of $Al(OH)_3$ on the hydrogen generation of aluminum–water system," J. Power Sources, vol. 219, pp. 16–21, 2012, doi: 10.1016/j.jpowsour.2012.06.077.

[40] H. Z. Wang, D. Y. C. Leung, M. K. H. Leung, and M. Ni, "A review on hydrogen production using aluminum and aluminum alloys," Renew. Sustain. Energy Rev., vol. 13, no. 4, pp. 845–853, 2009, doi: 10.1016/j.rser.2008.02.009.

[41] Z. Ma, P. Davenport, and G. Saur, "System and technoeconomic analysis of solar thermochemical hydrogen production," Renew. Energy, vol. 190, pp. 591–604, 2022, doi: 10.1016/j.renene.2022.03.108.

[42] B. Wang, S. Li, Y. Pu, and C. Wang, "Gliding arc plasma reforming of toluene for on-board hydrogen production," Int. J. Hydrogen Energy, vol. 45, no. 11, pp. 7010–7020, 2020, doi: 10.1016/j.ijhydene.2019.12.184.

[43] N. Budhraja, A. Pal, and R. S. Mishra, "Plasma reforming for hydrogen production: Pathways, reactors and storage," Int. J. Hydrogen Energy, vol. 48, no. 6, pp. 2447–2466, 2023, doi: 10.1016/j.ijhydene.2022.10.143.

[44] W. Wang, Y. Ma, G. Chen, C. Quan, J. Yanik, N. Gao, and X. Tu, "Enhanced hydrogen production using a tandem biomass pyrolysis and plasma reforming process," Fuel Process. Technol., vol. 234, p. 107333, 2022, doi: 10.1016/j.fuproc.2022.107333.

[45] J. D. Holladay, J. Hu, D. L. King, and Y. Wang, "An overview of hydrogen production technologies," Catal. Today, vol. 139, no. 4, pp. 244–260, 2009, doi: 10.1016/j.cattod.2008.08.039.

[46] D. J. Wilhelm, D. R. Simbeck, A. D. Karp, and R. L. Dickenson, "Syngas production for gas-to-liquids applications: Technologies, issues and outlook," Fuel Process. Technol., vol. 71, no. 1–3, pp. 139–148, 2001, doi: 10.1016/S0378-3820(01)00140-0.

[47] B. Ghorbani, S. Zendehboudi, Y. Zhang, H. Zarrin, and I. Chatzis, "Thermochemical water-splitting structures for hydrogen production: Thermodynamic, economic, and environmental impacts," Energy Convers. Manag., vol. 297, p. 117599, 2023, doi: 10.1016/j.enconman.2023.117599.

[48] D. Kumar and K. Muthukumar, "An overview on activation of aluminium–water reaction for enhanced hydrogen production," J. Alloys Compd., vol. 835, p. 155189, 2020, doi: 10.1016/j.jallcom.2020.155189.

[49] V. Yadav and F. Khalid, "A thermodynamics perspective on a novel aluminium–chlorine (Al–Cl) hybrid thermochemical cycle for hydrogen production," Int. J. Hydrogen Energy, vol. 50, no. 25, pp. 10001–10013, 2025, doi: 10.1016/J.IJHYDENE.2025.01.084.

[50] V. Shmelev, V. Nikolaev, J. H. Lee, and C. Yim, "Hydrogen production by reaction of aluminum with water," Int. J. Hydrogen Energy, vol. 41, no. 38, pp. 16664–16673, 2016, doi: 10.1016/J.IJHYDENE.2016.05.159.

[51] A. V. Ilyukhina, O. V. Kravchenko, and B. M. Bulychev, "Studies on microstructure of activated aluminum and its hydrogen generation properties in aluminum/water reaction," J. Alloys Compd., vol. 690, pp. 321–329, 2017, doi: 10.1016/J.JALLCOM.2016.08.151.

[52] A. I. Nizovskii, S. V. Belkova, A. A. Novikov, and M. V. Trenikhin, "Hydrogen production for fuel cells in reaction of activated aluminum with water," Procedia Eng., vol. 113, pp. 8–12, 2015, doi: 10.1016/J.PROENG.2015.07.278.

[53] V. Rosenband and A. Gany, "Application of activated aluminum powder for generation of hydrogen from water," Int. J. Hydrogen Energy, vol. 35, no. 20, pp. 10898–10904, 2010, doi: 10.1016/J.IJHYDENE.2010.07.019.

[54] F. Wang, H. Ni, F. Sun, M. Li, and L. Chen, "Overexpression of lncRNA AFAP1-AS1 correlates with poor prognosis and promotes tumorigenesis in colorectal cancer," Biomed. Pharmacother., vol. 81, pp. 152–159, 2016, doi: 10.1016/J.BIOPHA.2016.04.009.

[55] P. Godart, J. Fischman, K. Seto, and D. Hart, "Hydrogen production from aluminum–water reactions subject to varied pressures and temperatures," Int. J. Hydrogen Energy, vol. 44, no. 23, pp. 11448–11458, 2019, doi: 10.1016/J.IJHYDENE.2019.03.140.

[56] S. S. Razavi-Tousi and J. A. Szpunar, "Effect of structural evolution of aluminum powder during ball milling on hydrogen generation in aluminum–water reaction," Int. J. Hydrogen Energy, vol. 38, no. 2, pp. 795–806, 2013, doi: 10.1016/J.IJHYDENE.2012.10.106.

[57] B. Alinejad and K. Mahmoodi, "A novel method for generating hydrogen by hydrolysis of highly activated aluminum nanoparticles in pure water," Int. J. Hydrogen Energy, vol. 34, no. 19, pp. 7934–7938, 2009, doi: 10.1016/J.IJHYDENE.2009.07.028.

[58] K. Mahmoodi and B. Alinejad, "Enhancement of hydrogen generation rate in reaction of aluminum with water," Int. J. Hydrogen Energy, vol. 35, no. 11, pp. 5227–5232, 2010, doi: 10.1016/J.IJHYDENE.2010.03.016.

[59] B. Huang, C. H. Bartholomew, and B. F. Woodfield, "Facile synthesis of mesoporous γ-alumina with tunable pore size: The effects of water to aluminum molar ratio in hydrolysis of aluminum alkoxides," Microporous Mesoporous Mater., vol. 183, pp. 37–47, 2014, doi: 10.1016/J.MICROMESO.2013.09.007.

[60] A. A. Vostrikov, A. V. Shishkin, and O. N. Fedyaeva, "Conjugated processes of bulk aluminum and hydrogen combustion in water–oxygen mixtures," Int. J. Hydrogen Energy, vol. 45, no. 1, pp. 1061–1071, 2020, doi: 10.1016/J.IJHYDENE.2019.10.152.

[61] X. N. Huang, C. J. Lv, Y. X. Huang, S. Liu, C. Wang, and D. Chen, "Effects of amalgam on hydrogen generation by hydrolysis of aluminum with water," Int. J. Hydrogen Energy, vol. 36, no. 23, pp. 15119–15124, 2011, doi: 10.1016/J.IJHYDENE.2011.08.073.

[62] M. K. Yu, M. J. Kim, B. Y. Yoon, S. K. Oh, D. H. Nam, and H. S. Kwon, "Carbon nanotubes/aluminum composite as a hydrogen source for PEMFC," Int. J. Hydrogen Energy, vol. 39, no. 34, pp. 19416–19423, 2014, doi: 10.1016/J.IJHYDENE.2014.09.109.

[63] L. Zhang, Y. Tang, Y. Duan, L. Hou, L. Cui, F. Yang, and J. Huang, "Green production of hydrogen by hydrolysis of graphene-modified aluminum through infrared light irradiation," Chem. Eng. J., vol. 320, pp. 160–167, 2017, doi: 10.1016/J.CEJ.2017.03.025.

[64] X. N. Huang, C. J. Lv, Y. Wang, H. Y. Shen, D. Chen, and Y. X. Huang, "Hydrogen generation from hydrolysis of aluminum/graphite composites with a core–shell structure," Int. J. Hydrogen Energy, vol. 37, no. 9, pp. 7457–7463, 2012, doi: 10.1016/J.IJHYDENE.2012.01.126.

[65] F. Xiao, R. Yang, and J. Li, "Aluminum composites with bismuth nanoparticles and graphene oxide and their application to hydrogen generation in water," Int. J. Hydrogen Energy, vol. 45, no. 11, pp. 6082–6089, 2020, doi: 10.1016/J.IJHYDENE.2019.12.105.

[66] C. Wei, D. Liu, S. Xu, T. Cui, Q. An, Z. Liu, and Q. Gao, "Effects of Cu additives on the hydrogen generation performance of Al-rich alloys," J. Alloys Compd., vol. 738, pp. 105–110, 2018, doi: 10.1016/J.JALLCOM.2017.12.152.

[67] W. Yang, T. Zhang, J. Zhou, W. Shi, J. Liu, and K. Cen, "Experimental study on the effect of low melting point metal additives on hydrogen production in the aluminum–water reaction," Energy, vol. 88, pp. 537–543, 2015, doi: 10.1016/J.ENERGY.2015.05.069.

[68] H. Liu, F. Yang, B. Yang, Q. Zhang, Y. Chai, and N. Wang, "Rapid hydrogen generation through aluminum–water reaction in alkali solution," Catal. Today, vol. 318, pp. 52–58, 2018, doi: 10.1016/J.CATTOD.2018.03.030.

[69] X. Chen, Z. Zhao, M. Hao, and D. Wang, "Research of hydrogen generation by the reaction of Al-based materials with water," J. Power Sources, vol. 222, pp. 188–195, 2013, doi: 10.1016/J.JPOWSOUR.2012.08.078.

[70] C. R. Jung, A. Kundu, B. Ku, J. H. Gil, H. R. Lee, and J. H. Jang, "Hydrogen from aluminium in a flow reactor for fuel cell applications," J. Power Sources, vol. 175, no. 1, pp. 490–494, 2008, doi: 10.1016/J.JPOWSOUR.2007.09.064.

[71] M. Q. Fan, L. X. Sun, and F. Xu, "Experiment assessment of hydrogen production from activated aluminum alloys in portable generator for fuel cell applications," Energy, vol. 35, no. 7, pp. 2922–2926, 2010, doi: 10.1016/J.ENERGY.2010.03.023.

[72] C. Y. Ho and C. H. Huang, "Enhancement of hydrogen generation using waste aluminum cans hydrolysis in low alkaline de-ionized water," Int. J. Hydrogen Energy, vol. 41, no. 6, pp. 3741–3747, 2016, doi: 10.1016/J.IJHYDENE.2015.11.083.

[73] C. Chen, B. Lan, K. Liu, H. Wang, X. Guan, S. Dong, and P. Luo, "A novel aluminum/bismuth subcarbonate/salt composite for hydrogen generation from tap water," J. Alloys Compd., vol. 808, p. 151733, 2019, doi: 10.1016/J.JALLCOM.2019.151733.

[74] V. Shmelev, H. Yang, and C. Yim, "Hydrogen generation by reaction of molten aluminum with water steam," Int. J. Hydrogen Energy, vol. 41, no. 33, pp. 15073–15080, 2016, doi: 10.1016/j.ijhydene.2016.05.277.

[75] X. Gao, C. Wang, Y. Hou, L. Zhao, W. Bai, and D. Che, "Experimental study on characteristics and mechanism of hydrogen production from aluminium–water reaction for carbon-free power generation," Fuel, vol. 380, p. 133206, 2025, doi: 10.1016/J.FUEL.2024.133206.

[76] Y. Wang, Y. Wei, Z. Zhuang, W. Wei, Y. Duan, Y. Yang, and H. Jin, "Experimental study on hydrogen production characteristics of millimeter aluminum spheres in sub/supercritical water," Renew. Energy, vol. 240, p. 122221, 2025, doi: 10.1016/J.RENENE.2024.122221.